JOHANNES GUTENBERG UNIVERSITÄT MAINZ

Scanning Tunneling Microscopy and Spectroscopy of Surface States with Different Step Decorations on Re(0001) and Mobility Investigations of Ni on Re(0001) at low Temperatures

Dissertation zur Erlangung des akademischen Grades
„Doktor der Naturwissenschaften“
im Promotionsfach Physik

am Fachbereich Physik, Mathematik und Informatik der
Johannes Gutenberg-Universität Mainz

Vorgelegt von

Johannes Benjamin Regel

geboren am 17. März 1993 in Wiesbaden

submitted to the Department of Physics,
Mathematics and Computer Science (FB 08)
of the Johannes Gutenberg-Universität Mainz

Mainz, den 19. November 2020

This thesis was supervised by Prof. Dr. Hans-Joachim Elmers and was carried out at the Institute of Physics at the Johannes Gutenberg University Mainz from October 2017 to November 2020.

D77 (Dissertation Johannes Gutenberg-Universität Mainz)

1st report:
Prof. Dr. Hans-Joachim Elmers
Johannes Gutenberg-University Mainz

Submitted: **19. Nov. 2020**
Oral examination: **02. Feb. 2021**

Declaration

Hiermit versichere ich, dass ich die vorliegende Arbeit selbst angefertigt und nur die genannten Quellen benutzt habe.

Mainz, den 19. Nov. 2020

Johannes Regel

Johannes Regel
joregel@uni-mainz.de

Johannes Gutenberg-Universität D-55099 Mainz
Institut für Physik
KOMET335
Staudingerweg 7

Abstract

In this thesis, topographic and electronic properties of the pristine Re(0001) surface covered by 0 to 20 atomic layers of Au and Ni are studied using scanning tunneling microscopy and spectroscopy. Growth, mobility, surface structures, and surface states of these systems were investigated. The experimental results represent a step towards a fundamental understanding of surface properties, which are relevant for a wide range of applications such as chemical catalysis, quantum information technology, and spintronics.

In the first part of the thesis, quasiparticle interference patterns formed by a surface state on Re(0001) were investigated using scanning tunneling spectroscopy. The Tamm surface state exhibited a Rashba type band splitting, revealing a strong spin-momentum locking. The energy dispersion was inferred from Fourier-transformed differential conductivity maps for occupied and unoccupied states. An analysis of the phase of interference patterns at step edges revealed a change of sign in the effective energy barrier for backscattering above and below the Fermi level. The attenuation of the interference pattern with increasing distance indicated interband scattering as the significant scattering mechanism. Step decorations by Ni had a negligible influence on the pattern, excluding spin-flip scattering as a dominant contribution. The one-dimensional Au/Re line interface, however, reversed the scattering barrier behavior, indicating a coupling of Au and Re surface states. Using spin-resolved scanning tunneling spectroscopy, we investigated the spin-dependent scattering of spin waves.

In the second part of this thesis, a movement of Ni adatoms at 4.6 K on a Re(0001) single crystal was investigated, while the surface was rigid at room temperature. Measurements at intermediate temperatures revealed increasing mobility with decreasing temperature. This inverse mobility behavior can be explained tentatively by a combination of a small force induced by the tip of a scanning tunneling microscope (STM) and the weakened bonding of Ni adatoms due to an increase of the mismatch between their lattice constants at low temperature. To achieve a better understanding of the physics resulting in this unique behavior, investigations at various temperatures, coverages, and tunneling parameters were performed. Different types of movement and decreasing mobility with increasing temperature and layer thickness were observed. In addition, measurements with a Fe coated tip on ultrathin Ni films revealed an unexpected spectroscopic contrast. Close inspection of the spectroscopic and topographic results indicated that Fe atoms are transferred from the tip to the sample surface during scanning.

Zusammenfassung

In dieser Arbeit werden die topographischen und elektronischen Eigenschaften einer reinen Re(0001)-Oberfläche und der Oberfläche mit einer Bedeckung von 0 bis 20 Atomlagen aus Au oder Ni, mittels Rastertunnelmikroskopie und -spektroskopie untersucht. Dabei werden Wachstum, Mobilität, Oberflächenstrukturen und Oberflächenzustände dieser Systeme studiert. Die experimentellen Ergebnisse stellen einen Schritt zu einem grundlegenden Verständnis der Oberflächeneigenschaften dar, die für eine Vielzahl von Anwendungen wie chemische Katalyse, Quanteninformationstechnologie und Spintronik relevant sind.

Im ersten Teil der Arbeit werden Quasiteilchen-Interferenzmuster, die durch einen Oberflächenzustand auf Re(0001) gebildet werden, mittels Rastertunnel-Spektroskopie untersucht. Der Tamm-Oberflächenzustand weist eine Bandaufspaltung vom Rashba-Typ auf, die eine starke Spin-Impuls-Kopplung offenbart. Die Energiedispersion wird aus Fourier-transformierten differentiellen Leitfähigkeitskarten für besetzte und unbesetzte Zustände abgeleitet. Eine Analyse der Phase von Interferenzmustern an Stufenkanten zeigt eine Änderung des Vorzeichens der effektiven Energiebarriere für die Rückstreuung oberhalb und unterhalb des Fermi-Niveaus. Die Dämpfung des Interferenzmusters mit zunehmendem Abstand deutet auf Interbandstreuung als Streumechanismus hin. Die Stufendekoration durch Ni hat einen vernachlässigbaren Einfluss auf das Interferenzmuster, womit die Spin-Flip-Streuung als Beitrag ausgeschlossen werden kann. Die eindimensionale Au/Re-Grenzfläche kehrt jedoch das Verhalten der Streubarriere um, was auf eine Kopplung von Au und Re Oberflächenzuständen hinweist. Mittels spinaufgelöster Rastertunnelspektroskopie untersuchen wir die spinabhängige Streuung von Spinwellen.

Im zweiten Teil dieser Dissertation wird die Erhöhung der Mobilität von Ni-Clustern bei 4.6 K auf Re(0001) diskutiert, während die Oberfläche bei Raumtemperatur starr ist. Messungen bei Zwischentemperaturen zeigen eine zunehmende Mobilität mit abnehmender Temperatur. Dieses umgekehrte Mobilitätsverhalten lässt sich durch eine Kombination aus einer kleinen Kraft, die durch die Spitze eines Rastertunnelmikroskops (STM) induziert wird, und der geschwächten Bindung der Ni-Adatome aufgrund einer Zunahme der Fehlanpassung der Gitterkonstanten mit abnehmender Temperatur erklären. Um ein besseres Verständnis der Physik zu erhalten, die zu diesem einzigartigen Verhalten führt, werden Untersuchungen bei verschiedenen Temperaturen, Bedeckungen und Tunnelparametern durchgeführt. Man beobachtet unterschiedliche Bewegungsarten und eine abnehmende Mobilität mit zunehmender Temperatur und Schichtdicke. Darüber hinaus zeigen Messungen mit einer Fe-beschichteten Spitze auf ultradünnen Ni-Filmen einen unerwarteten spektroskopischen Kontrast. Eine genaue Prüfung der spektroskopischen und topografischen Ergebnisse zeigt, dass Fe-Atome beim Scannen von der Spitze auf die Probenoberfläche übertragen werden.

Table of Contents

1. Introduction and Motivation **1**

2. Fundamentals of the Microscope **5**
2.1. Tunneling Effect . . . 6
2.2. Theoretical Model - Tunneling Process . . . 8
2.3. Resolution, Limitations of the Model . . . 12
2.4. The Scanning Tunneling Microscope . . . 14
2.5. Methods of Measurement . . . 16
2.5.1. Constant-Height Mode . . . 16
2.5.2. Constant-Current Mode . . . 17
2.6. Spectroscopy . . . 18
2.6.1. Spin-Polarized STS . . . 20
2.7. Low-Energy Electron Diffraction . . . 20

3. Samples and Theory **23**
3.1. Rhenium, Gold and Nickel . . . 23
3.1.1. Rhenium . . . 23
3.1.2. Gold . . . 24
3.1.3. Nickel . . . 24
3.1.4. Growth . . . 24
3.1.5. Mismatch . . . 26
3.1.6. Strain . . . 27
3.2. Entropy . . . 27
3.3. Inverse Melting . . . 30
3.4. Mobility of Ni . . . 31
3.5. Electronic Band Structure . . . 32
3.6. Surface States . . . 36
3.6.1. Bloch Wave . . . 36
3.6.2. Shockley-States . . . 37
3.6.3. Tamm-States . . . 39
3.6.4. Friedel Oscillations . . . 40
3.7. Bychkov–Rashba Effect . . . 40

4. Design and Methodology **43**
4.1. The Scanning Tunneling Microscope . . . 43
4.2. Operating in UHV . . . 47
4.3. Electronics . . . 48
4.4. Sensitivity of STM . . . 49
4.5. Tunneling Tip . . . 49
4.6. Sample Preparation and Experimental Procedure . . . 51

5. Growth of Ni and Au on Re(0001) 53
5.1. LEED Results . . . 53
5.2. STM Results . . . 56

6. Results and Discussion: Surface States 61
6.1. Wave Length Analysis . . . 61
6.2. Attenuation . . . 63
6.3. Phase Angle . . . 65
6.4. Surface States on Au . . . 69
6.5. Surface States with Spin-Resolved STS . . . 71
6.6. Line Defects . . . 73

7. Results and Discussion: Inverse Transition Upon Cooling 75
7.1. Mobility Measurements . . . 75
7.2. Discussion . . . 80
7.3. Movement at Higher Temperatures . . . 84
7.4. Dependence on Film Thickness . . . 84
7.5. Au on Re(0001) . . . 87
7.6. Spin-Resolved Measurements . . . 88

8. Error Discussion 91
8.1. Topographic Errors . . . 91
8.2. Spectroscopic Errors . . . 92

9. Conclusion and Outlook 95

Bibliography 99

List of Figures 109

A. Appendix 111
A.1. Mobility with Different Parameters . . . 111
A.2. Mobility at Higher Film Thickness . . . 113
A.3. Extensions to the Measurement Series in the Thesis . . . 114

1. Introduction and Motivation

Even before the ancient Greeks melting was a well-known process. Today, it is still a daily observed process of everyday life. However, the understanding of this process in physics is of fundamental importance. But what does melting mean, exactly? In general, the phase transition of a solid into the liquid aggregate state, mostly due to heat input or pressure reduction, is called melting. If an element melts at constant pressure, the melting temperature can be determined. Melting temperature and pressure form the so-called melting point. Due to the everyday presence, it may therefore be surprising that the microscopic mechanisms of the melting of three-dimensional systems are still not completely understood. On a two-dimensional surface, it is much more difficult to define melting, but it is in a way easier to observe on a microscopic level. In this case, it is a phase transition from a phase with higher-order and less mobility, to a phase with less order and higher mobility. For the theory of melting in two dimensions, the so-called KTHNY-theory was awarded the Nobel Prize in 2016 [1, 2, 3]. Therefore, this topic is not only important for everyday life but also an interesting research area in physics.

But is the reverse process, in other words melting by cooling, also possible? Inverse melting (IM) is a counter-intuitive and very rare phenomenon. In general, IM is defined as the transition from a phase with a higher-order to one with a lower order by reducing the temperature [4]. IM was first predicted by G. Tammann in 1903 as a solution to avoid the issue of the melting curve progressing to infinity [5]. He recognized there can be no termination of a liquid-solid phase line, and hence there is a symmetry breaking between crystal and liquid phase. But for a long period, IM was only observed under extreme conditions, such as high pressure. With the transformation of the concept to a two-dimensional plane, melting is no longer a suitable expression. A better term would be inverse transition upon cooling. In the case of this work, a combination of a small force, induced by the STM-tip and the weakened bonding between the Ni atoms and Rhenium results in mobile Ni atoms at the surface. So, a suitable term could also be the decrease of the energy barrier for mobilization upon cooling.

The growth of metal on metals has been investigated for numerous systems [6]. Understanding the growth modes is an important precondition for the fabrication of functional devices comprising metallic multilayers such as spintronic devices [7]. Considering the tendency to develop multilayers with functional layers down to a few atomic layers, it becomes increasingly important to tailor the growth modes on an atomic level.

The general understanding of metal growth is that adatoms that hit the surface remain typically on the nearest lattice site. The kinetic energy for the metal atoms to move around on a terrace may be provided by thermal energy. By annealing the metal layer in an appropriate temperature range, the metal atoms can use the added kinetic energy to find an energetically more favorable position, often at existing step edges or defects.

Usually, the adatoms are hindered to cross a step edge because of the Ehrlich-Schwoebel barrier [8, 9]: if an adatom has found an energetically favorable position, the atom will stay there unless it has acquired enough kinetic energy to overcome the energy barrier. Thus, an increasing sample temperature usually results in increased mobility of adatoms on the surface which can be exploited to smoothen the surface roughness. On the other hand, lowering the sample temperature to cryogenic temperatures normally results in freezing of the mobility, eventually even allowing for the investigation of isolated atoms on a surface terrace [10, 11].

Surfaces represent another fundamental field of physics. If a particular orbital is responsible for the chemical bond, it is influenced strongly by its neighboring atoms. Assuming these bonds are missing or broken and these orbitals are sticking out above the surface, then the energy levels of such states are expected to shift significantly from the bulk values due to the change in chemical bonding. Thus, the periodic potential of the atomic nuclei within the bulk is weakened at the uppermost atomic layers before the transition to vacuum [12]. This changes the electric states, creates new electronic levels, and can also modify many-body effects or even cause completely new effects such as the Bychkov–Rashba effect. The Rashba effect is a symmetry break at the surface which causes a spin-orbit coupling (SOC) of the electrons, leading to a splitting of the states. Many other phenomena on surfaces are related to this change in electronic structure, like the surface free energy, the adhesion forces, and the specific chemical reactivity of particular surfaces. These significant differences between volume and surface states become increasingly important for nanostructures, spintronics, and chemical catalysis.

The field of surface physics is therefore constantly growing, intending to develop a detailed understanding of the electronic and magnetic surface structure. In principle, the approaches to solving problems do not differ significantly from the considerations of bulk crystals. Compared to the bulk, however, two additional difficulties arise at surfaces. Due to the symmetry breaking, a translational symmetry exists only in directions within the surface plane. Along the surface normal, however, there is no periodicity, which complicates a theoretical treatment. Significantly more serious, especially in the experimental field, are surface structure problems. Based on the altered chemical bond at the surface, surface relaxations and reconstructions occur. These reconstructions make not only the theoretical consideration more difficult but are also very obstructive for the experimental approach. In order to have clean surfaces for a suitable period of time, it is advisable to work under ultrahigh vacuum (UHV) conditions and clean the samples from unwanted contaminations using ultrahigh heating or sputtering, for example. Therefore, there is no general, simple, and uncomplicated experimental technique to determine the atomic structure in the uppermost atomic layers. Several relatively complex methods such as dynamic low-energy electron diffraction (LEED) (Sec. 2.7) analysis, SEXAFS[1], STM (Sec. 2.4) and atomic scattering provide information, but relatively few structures have been fully determined [12].

It is known that the broken inversion symmetry at surfaces can lead to a lifting of the spin degeneracy of surface states. Such degeneracy lifting is most pronounced

[1] Surface-extended X-ray absorption fine structure is a technique involving the illumination of the sample by high-intensity X-ray beams and monitoring their photoabsorption by detecting the intensity of Auger electrons as a function of the incident photon energy.

at the surface of high-Z materials [13]. The spin momentum locking of the surface states results in orthogonal wave functions provisionally eliminating backscattering. A similarly forbidden backscattering of surface states is responsible for the particular properties of topological insulators. Therefore, the study of scattering processes of spin momentum locked surface states is of growing interest [14, 15].

The central question is how effectively spin momentum locking suppresses quantum interference and how to tailor the scattering amplitude by material design. Controversial explanations for the occurrence of quantum interference have been discussed: for Rashba split surface states, spin-conserving interband scattering can contribute to interference [16, 17, 18]. Alternatively, quantum interference patterns may result from nonorthogonal states causing only partial suppression of backscattering [19, 20, 21]. Breaking the time-reversal symmetry with a magnetic material could also activate forbidden scattering channels [22, 23, 24].

The Re(0001) surface is an interesting system potentially suitable for solving this controversy [25, 26]. A surface state is localized at the topmost atomic layer [27, 28], and the orbital d_z^2 character is favorable for detection by scanning tunneling spectroscopy (STS). The strong spin-orbit coupling of Re leads to a pronounced Rashba splitting [29, 30]. By different step decorations with ferromagnetic nickel and the very stable diamagnetic gold, these questions should be able to be answered in a more detailed manner.

An article reporting a possible technical application has been published recently [31]. Reported is a Stern-Gerlach spin filter built with a nonuniform spin-orbit interaction system, which is easier to build and has almost 100% spin polarization without applying any external magnetic field and without attaching ferromagnetic contacts. A lateral voltage is used to create a locally changing spin splitting. The Au/Re surface alloy with one monolayer gold deposited creates a similar structure which would have the same effect as the proposed spin filter.

The scanning tunneling microscope has been used extensively over the past three decades as an atomic-scale structural probe and is useful for observing the surface electronic structure [29, 30]. With the STM, atomic structures can be resolved, and even individual molecular orbitals can be partially imaged. At the same time, information about the local density of states (LDOS) of the sample is obtained. The STM can also be used to perform electronic spectroscopy to measure the conduction properties and electron waves. This method has a low-energy consumption, i.e. the sample is not significantly heated during the measurement so that a stable temperature is guaranteed. In contrast to methods like angle-resolved photoemission spectroscopy (ARPES), it is possible to investigate selected areas and measuring electronic states below and above the Fermi energy. The quantum interference mapping technique observes spatial oscillations of the energy-resolved DOS, which originates from the elastic scattering of the eigenstates resulting in well observable Friedel-oscillations [32]. Thus, the STM fulfills all requirements for the experiment.

The present work is divided into six parts. For the interpretation of the measurements, the necessary theory is explained in Chapters 2 and 3. Chapter 2 introduces the theory of the scanning tunneling microscope. Furthermore, the measuring methods and the STM itself are explained. Chapter 3 deals with the basics of the investigated samples,

states, and mobility of metals as well as an introduction in Rashba splitting and inverse melting. The experimental equipment can be found in Chapter 4. Here, the emphasis is also placed on the exact execution of the measurements. Chapter 5 describes the growth of Au and Ni under different coverages. The following Chapters 6 and 7 are dealing with the results and the interpretation of the measurements of the two main themes surface states and phase transition upon cooling being treated separately. The error discussion in Chapter 8 is followed by the last Chapter 9, which contains a summary of the work.

2. Fundamentals of the Microscope

With scanning probe microscopy, the image is not generated by full-field imaging with lenses as in an optical microscope. Instead, local interactions between probe-tip and sample are used for imaging. The surface of the sample is scanned by a probe-tip point by point in a scanning process. A computer then assembles the measured values for each individual point into a digital image. Scanning probe microscopy is thus very surface-sensitive.

The scanning tunneling microscope , developed in 1981 by Gerd Binnig and Heinrich Rohrer, was awarded the Nobel Prize in 1986 [33]. The theoretical work was carried out by Bardeen in 1961 with an analysis of the tunneling effect between two metals and further developed by Tersoff and Hamann with a description of the tip geometry of the STM. The STM is characterized by the direct imaging of the sample surface in real space. It can display non-periodic structures with atomic resolution.

The STM uses a usually metallic tip as the probe, where the movement is controlled by piezo crystals. The image is generated, based on the tunneling current between sample and tip. The measured current for a defined applied voltage depends exponentially on the distance between sample and tip so that subatomic resolution in the sub-picometer range can be achieved at small distances. Thus, the STM can even image single atomic and molecular orbitals. However, UHV conditions are necessary to prevent the surface from unwanted adsorbates [34].

Further STM techniques include the manipulation of atoms and molecules at the atomic level to form diverse nanostructures [35, 36, 37, 38]. Moreover, the variation of the tunneling voltage can be used for spatially resolved spectroscopy to measure the electronic properties of a surface [39]. The STM can operate in a temperature range from the millikelvin range up to several hundred Kelvin. Low temperatures are often used: the lower the temperatures, the lower the thermal energy of the investigated molecules and atoms. This usually reduces vibrations and movements on the surface and counteracts the thermal drift of the sample. A temperature close to 0 K minimizes drifts and increases measurement accuracy and energy resolution. In addition, the vacuum is improved by the cold surfaces of the thermal shields in the microscope, because adsorbates adhere to them and are permanently trapped there.

The distance between sample and tip is in the ångström range. Since the tunneling current depends exponentially on this distance, the STM is very susceptible to external vibrations and must be decoupled mechanically as far as possible. If a voltage is applied between sample and tip, a tunneling current flows which depends on both the distance and the local electron density. The tunneling current signal consists of a convolution of the surface topography with the LDOS of sample and tip. The recorded, unprocessed images of STM are thus three-dimensional height topographies of constant electron density.

In the following chapter, the basics of the scanning tunneling microscope are presented. Based on the tunneling effect (Sec. 2.1), the many-body tunneling process is derived to obtain a mathematical expression for the tunneling current (Sec. 2.2). After a consideration of the model used (Sec. 2.3), the setup of a STM (Sec. 2.4) for investigations on surfaces (2.5) is discussed. The next step is to introduce scanning tunneling microscopy for measuring the electronic properties of samples (Sec. 2.6). Finally, there is a short introduction to low-energy electron diffraction technology (Sec. 2.7), providing alternative access to the atomic structure at surfaces.

2.1. Tunneling Effect

The tunneling effect was discovered in the early twentieth century as a description for the decay of an α particle and appears in many physical phenomena. Thus, it was known before the development of the STM. Atomic particles can overcome potential barriers, even if the barriers are higher than the particle energy $E < V_0$. Classically, the overcoming of the barrier cannot be explained, instead, the explanation is of a purely quantum mechanical nature. Every particle can be described by a wave function being the solution of the Schrödinger equation, whose absolute square indicates the probability density of the particle. This probability decreases exponentially with increasing distance, but the probability of a particle appearing behind the barrier is no longer zero [40]. Figure 2.1 shows a schematic representation of this effect.

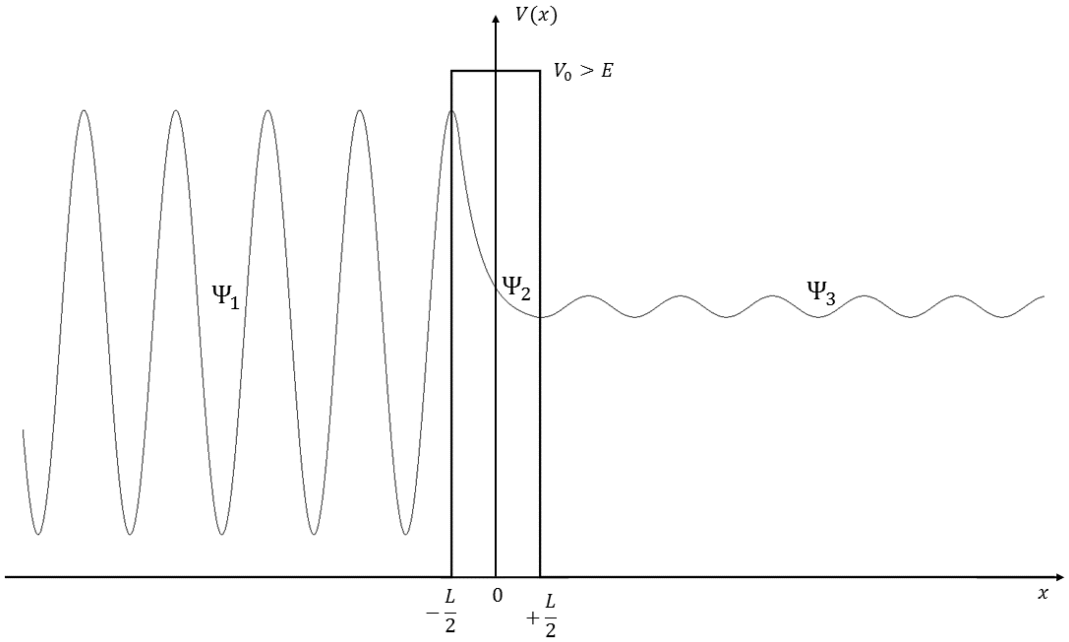

Fig. 2.1. Schematic representation of the tunneling effect: A particle (Ψ_1) with mass m and energy $E < V_0$ tunnels (Ψ_2) through a box-shaped potential barrier of height V_0 and width L. Most particles are reflected at the potential barrier and only a few tunnels through the barrier (Ψ_3). The amplitude behind the barrier is much smaller, while the energy and wavelength of the particles remain constant.

In the following, the tunneling effect is modeled without consideration of spin-orbit coupling and electron correlation effects to identify basic dependencies. The one-dimensional Schrödinger equation can be used for this purpose, whereby the potential $V(x)$ represents the tunneling barrier:

$$-\frac{\hbar^2}{2m}\frac{d^2\Psi(x)}{dx^2} + V(x)\Psi(x) = E\Psi(x). \tag{2.1}$$

More precisely, the tunneling barrier is a box-shaped potential of height $V_0 > E$ and width L:

$$V(x) = \begin{cases} V_0 & -\frac{L}{2} \leq x \leq \frac{L}{2} \\ 0 & \text{else,} \end{cases} \tag{2.2}$$

considering an incoming particle Ψ_1 with the energy E with $0 < E < V_0$. At the potential barrier, it is either reflected or transmitted, where the probability of reflection depends on the barrier height and width. Within the barrier, an exponential drop of the wave function amplitude Ψ_2 is obtained as a solution. Behind the barrier, the particle is described by the scattered wave Ψ_3 with a lower amplitude [40]:

$$\Psi_1(x) = A_1 \cdot e^{ik_0 x} + A_2 \cdot e^{-ik_0 x}, \qquad x < -\frac{L}{2}, \tag{2.3}$$

$$\Psi_2(x) = B_1 \cdot e^{\kappa x} + B_2 \cdot e^{-\kappa x}, \qquad -\frac{L}{2} \leq x \leq \frac{L}{2}, \tag{2.4}$$

$$\Psi_3(x) = S \cdot e^{ik_0 x}, \qquad \frac{L}{2} < x, \tag{2.5}$$

where

$$E = \frac{\hbar^2}{2m} \cdot k_0^2, \qquad V_0 - E = \frac{\hbar^2}{2m} \cdot \kappa^2. \tag{2.6}$$

The amplitude of the incoming wave is known and can be normalized to $A_1 = 1$. The remaining four amplitudes A_2, B_1, B_2, and S can be calculated using a system of equations with boundary- and continuity-conditions at the potential boundaries. The amplitude of the outgoing, i.e. transmitted wave S is of primary interest. This indicates the transmission probability for an electron through the tunneling barrier, and thus

directly determines the tunneling current. The following result is obtained for the tunneling probability:

$$T = \left(1 + \frac{1}{4} \cdot \left(\frac{\kappa}{k_0} + \frac{k_0}{\kappa}\right)^2 \cdot \sinh^2(\kappa L)\right)^{-1}, \qquad \text{with} \qquad \left(\frac{\kappa}{k_0} + \frac{k_0}{\kappa}\right)^2 = \frac{V_0^2}{E(V_0 - E)}. \tag{2.7}$$

For a large barrier $\kappa L \gg 1$ $\sinh^2(\kappa L) \approx 1/4 * \exp(2\kappa L)$ applies, resulting in a transmission probability of [40]:

$$T \approx \frac{16E(V_0 - E)}{V_0^2} \cdot e^{-2\alpha L}, \qquad \text{with} \qquad \alpha = \sqrt{\frac{2m(V_0 - E)}{\hbar^2}}. \tag{2.8}$$

Noticeable is the exponential dependence of the transmission probability depending on the width of the tunneling barrier L. This remains the same for multidimensional many-body systems and directly determines the tunneling current of the STM: the width of the tunneling barrier is the distance between the tip and the sample.

2.2. Theoretical Model - Tunneling Process

In the case of the STM, sample and tip are on different electric potentials. In addition, a geometric component between sample and tip comes into play. The first situation was theoretically treated and described by J. Bardeen in 1961. In his model, he assumes a tunneling process between two different metals separated by a potential barrier [41]. He calculates the tunneling matrix element $M_{\mu\nu}$, which describes the probability of an electron's transition from an initial quantum state μ to a final state ν. The tunneling matrix element represents the tunneling probability. Independent of small energy changes it remains unchanged even during a transition to the superconducting state.

Bardeen considered the two metals a and b as separate systems in two different many-particle states Ψ and $\Psi_{\mu\nu}$. The wave functions of the two systems oscillate in the metal and, as in the single-particle case, are either reflected or transmitted at the interface. To create a tunneling barrier of appropriate size, the surfaces at positions x_a and x_b of the two metals are now approached as shown in Fig. 2.2. The two wave functions are thus a good approximation in the area of the barrier $x_\mathrm{a} < x < x_\mathrm{b}$, resulting in a time-independent solution, which is supplemented by the tunneling current as a time-dependent perturbation term [41]:

$$M_{\mu\nu} = -\frac{\hbar^2}{2m} \int (\Psi^* \nabla \Psi_{\mu\nu} - \Psi_{\mu\nu} \nabla \Psi^*) d\tau. \tag{2.9}$$

The integral is integrated for the volume element $d\tau$. Additionally, Bardeen obtained a first expression for the x-component, along the surface normal, of the tunneling current $J_{mn}(x_1)$ by expressing the matrix element using the imaginary current-density operator [41]:

$$M_{\mu\nu} = \frac{1}{2\mu} \sum_i \int ... \int \left[\Psi_0^* \partial \Psi_{mn} / \partial x_i - \Psi_{mn} \partial \Psi_0^* / \partial x_i\right] \delta\left(x_1 - x_i\right) d\tau_1 ... d\tau_N \tag{2.10}$$

$$= -i \cdot J_{\mu\nu}(x_1), \tag{2.11}$$

where x_1 must be in the range of the barrier $x_\mathrm{a} < x_1 < x_\mathrm{b}$.

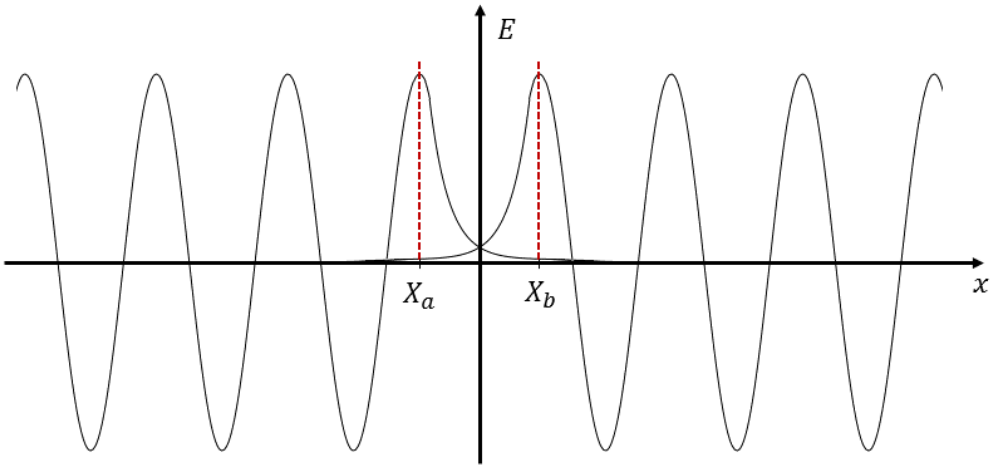

Fig. 2.2. The model of Barden's approach: the surfaces of the two metals are at x_a and x_b. The wave functions of the systems are in separate states. After moving them together they are no longer valid in the area of the other metal but are a good approximation for the space between the metals, such as the location of the barrier $x_\mathrm{a} < x < x_\mathrm{b}$.

Based on Bardeen's results, Tersoff and Hamann developed a theory for calculating the tunneling current, taking the tip geometry into account. They published their work in 1983 [42] and supplemented and extended it in 1985 [43]. Very similar results were obtained in preliminary tests with tunneling tips made of different metals. Thus, the metal of the tip was neglected. In order to find a simple, calculable approximation for the tunneling current, Tersoff and Hamann made partly drastic assumptions. In particular, the more precise electronic structures of sample and tip are not considered. In their model, they approximated the tip with a spherical potential corresponding to the wave function of an s-orbital. Additionally, an absolute vacuum is assumed.

With Barden's formalism, the first-order tunneling current can be represented as follows:

$$I = \frac{2 \cdot \pi \cdot e}{\hbar} \sum_{\mu\nu} f\left(E_\mu\right) \left[1 - f\left(E_\nu + eV\right)\right] |M_{\mu\nu}|^2 \delta\left(E_\mu - E_\nu\right), \tag{2.12}$$

where $f\left(E_\mu\right)$ is the Fermi function, V is the tunneling voltage, and $M_{\mu\nu}$ is the matrix transition element between the states of tip Ψ_μ and sample Ψ_ν. The energies of the states Ψ_μ and Ψ_ν are E_μ and E_ν.

In this case, Ψ_μ and Ψ_ν are nonorthogonal, independent eigenstates of different Hamilton operators. In a linear approximation, assuming 0 K and a small tunneling voltage, i.e. $V \leq 10\,\text{meV}$, [Eq. 2.12] can be linearized to the following equation (Fermi energy E_F):

$$I = \frac{2 \cdot \pi \cdot e^2 \cdot V}{\hbar} \sum_{\mu\nu} |M_{\mu\nu}|^2 \delta\left(E_\nu - E_F\right) \delta\left(E_\mu - E_F\right). \tag{2.13}$$

Considering the limit case where the tip can be replaced by a point-shaped probe head and assume an arbitrary distribution of the peak wave functions, the matrix transition element $M_{\mu\nu}$ is proportional to the amplitude of the sample wave function $|\Psi_\nu\left(\vec{r_0}\right)|^2$ at the position of the tip $\vec{r_0}$. Thus, one obtains:

$$I \approx \sum_{\nu} |\Psi_\nu\left(\vec{r_0}\right)|^2 \delta\left(E_\nu - E_F\right). \tag{2.14}$$

The term on the right corresponds to the LDOS at the Fermi energy E_F. Already here, the dependence of the tunneling current on the DOS of the sample can be seen. To further calculate the expression, the wave functions of sample and tip must now be specified. In principle, the surface wave function of the sample Ψ_ν can be written in the following form [43]:

$$\Psi_\nu = \Omega_\text{s}^{-\frac{1}{2}} \sum_{G} a_G \cdot \exp\left[\left(\kappa^2 + |\vec{k_G}|^2\right)^{\frac{1}{2}} \cdot z\right] \exp\left(i \cdot \vec{k_G} \cdot \vec{x}\right). \tag{2.15}$$

Ω_s describes the sample volume; $\kappa = \sqrt{2 \cdot m \cdot \varphi_\text{p}/\hbar}$ is the inverse decay length, with the work function φ_p. For electronic states at the Fermi level, the work function φ_p represents the height of the potential barrier on the sample surface. $\vec{k_G} = \vec{k_{||}} + \vec{G}$ is the addition of the surface Bloch-vector $\vec{k_{||}}$ and the reciprocal lattice vector $\vec{G}$. The term contains the constant a_G, which is in the first order approximation equal to one and is thus neglected in the further calculation. For non-periodic surface structures, the sum over G becomes an integral.

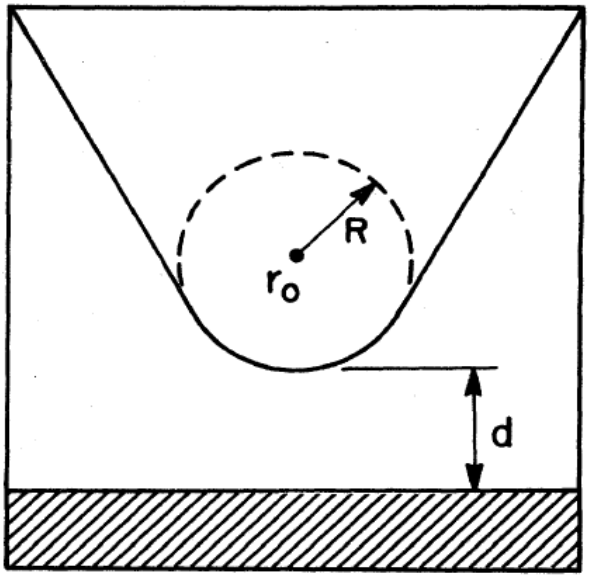

Fig. 2.3. Model of the tip [42]. The end of the tip is modeled by a sphere with a radius of curvature R and the center $\vec{r_0}$. The smallest distance from the sample surface is d. Thus, the radial part of an s-orbital is assumed as an approximation of the wave function.

The microscopic structure of the tip is generally unknown. In this model, Tersoff and Hamann assume for the sake of simplicity a spherical tip with the local radius R and the center $\vec{r_0}$. The smallest distance between tip and sample is d, as can be seen in Fig. 2.3. For the tip, a wave function with an asymptotic-spherical shape [43] results in the considered area:

$$\Psi_\mu = \Omega_\mathrm{t}^{-\frac{1}{2}} \cdot \frac{c_t \cdot \kappa \cdot R \cdot e^{\kappa \cdot R}}{\kappa \cdot |\vec{r} - \vec{r_0}|} \cdot e^{-\kappa \cdot |\vec{r} - \vec{r_0}|}, \tag{2.16}$$

where Ω_t is the probe volume and $\vec{r}$ is the position vector. $\kappa = \sqrt{2 \cdot m \cdot \varphi_\mathrm{s}/\hbar}$ is the inverse decay length with the work function at the tip φ_s.

Now $\varphi_s = \varphi_p = \phi_\mathrm{eff}$ is assumed, with ϕ_eff the joint effective potential of sample and tip, which corresponds approximately to the mean value of the work function of the sample and the tip. The parameter c_t is determined only by the tip geometry and the electronic structure. With the approximation $R >> \kappa^{-1}$ it is set equal to one in the following. Furthermore, the angular dependence of Ψ_μ is neglected.

The development of the tip wave function in the same way as the function of the surface combined with converting the expression for the tunneling matrix element $M_{\mu\nu}$ leads to [43]:

$$M_{\mu\nu} = \frac{\hbar^2 \cdot 4\pi}{2m \cdot \kappa} \cdot \Omega_t^{-\frac{1}{2}} \cdot R \cdot \kappa \cdot e^{2\kappa R} \cdot \Psi_\nu \left(\vec{r_0}\right). \tag{2.17}$$

Inserting this expression into the tunneling current [Eq. 2.13] and simplifying it results in:

$$I = \frac{32\pi^3 \cdot e^2 \cdot V}{\hbar} \cdot \varphi^2 \cdot D_t \left(E_F\right) \cdot \frac{R^2}{\kappa^4} \cdot e^{2\kappa R} \cdot \sum_\nu \left|\Psi_\nu \left(\vec{r_0}\right)\right|^2 \delta \left(E_\nu - E_F\right). \tag{2.18}$$

$D_t \left(E_F\right)$ describes the LDOS of the tip at the Fermi energy E_F. As explained above, the expression $\sum_\nu \left|\Psi_\nu \left(\vec{r_0}\right)\right|^2 \delta \left(E_\nu - E_F\right)$ is the LDOS of the sample located at $\vec{r}$, with $\left|\Psi_\nu \left(\vec{r_0}\right)\right|^2 \propto \exp\left\{-2\kappa \left(R + d\right)\right\}$. The tunneling current is then given by [43]:

$$I = \frac{32\pi^3 \cdot e^2 \cdot V}{\hbar} \cdot \varphi^2 \cdot D_t \left(E_F\right) \cdot \frac{R^2}{\kappa^4} \cdot e^{-2\kappa d} \cdot D_p \left(\vec{r}, E_F + e \cdot V\right). \tag{2.19}$$

To clarify the important dependencies of the tunneling current, the expression can be written in proportional representation. Where d is the distance between sample and tip and V is the applied voltage:

$$I \sim D_t \left(E_F\right) \cdot D_p \left(E_F \pm e \cdot V\right) \cdot eV \cdot e^{-2\kappa d}. \tag{2.20}$$

The exponential dependence of the tunneling current on the distance between tip and sample was expected. The dependence of the current on the LDOS at the Fermi level E_F has already been seen during the derivation. Furthermore, the tunneling current is linearly dependent on the applied voltage $I \sim V$.

2.3. Resolution, Limitations of the Model

The crucial approximation of the model of Tersoff and Hamann is the assumption of an s-wave function to describe the tip. In addition, an undisturbed tip-wave-function is assumed. The angular dependence of Ψ_μ $(l \neq 0)$, on the other hand, can be considered quite easily via the m-term. The result is a weighting of Ψ_ν with the factor $\sim \sqrt{1 + q^2/k^2}$, which is negligible for small l. Only for larger tip radii R with a stronger angular dependence the model becomes less accurate.

For typical values for the tunneling conductivity of metals the following estimate is obtained [42]:

$$\sigma \approx 0.1 \cdot R^2 \cdot e^{2kR} \cdot \rho\left(\vec{r_0}, E_F\right), \tag{2.21}$$

where

$$\rho\left(\vec{r_0}; E_F\right) = \sum_{\nu} |\Psi_\nu\left(\vec{r_0}\right)|^2 \delta\left(E_\nu - E\right) \quad \text{and} \quad |\Psi_\nu\left(\vec{r_0}\right)|^2 \sim e^{-2k(R+d)}. \tag{2.22}$$

An exponential dependence of the tunneling conductivity and the tip-sample distance d is given by:

$$\sigma \sim e^{-2kd}. \tag{2.23}$$

Under the condition $q \ll 2k$ the resolving power A of the STM can also be roughly estimated [42]:

$$A = \sqrt{\frac{2\left(R+d\right)}{\kappa}}. \tag{2.24}$$

Adding other values typical for metals[1] leads to a resolving power in the ångström range.

STMs have an actual resolution in the picometer range. Therefore, the high resolution cannot be explained with the model of Tersoff and Hamann. The model can provide the dependencies of the tunneling current but fails to explain the high spatial resolution. J. Chen investigated this problem [44]. He concluded, as Tersoff and Hamann expected, that modeling the tip as a pure s-wave function is too drastic to derive an exact solution for the problem since higher d-wave functions also play a non-negligible role. He also found that enormous interactions between sample and tip exist, which lead to the fact that the basis of the theory, namely Bardeen's description of the tunneling matrix element, is no longer valid. With the aim of finding a simple solution for the problem, Tersoff and Hamann have oversimplified the model [45].

A third weakness of the model results from the uncertainty relation: assuming that the tunneling barrier is lower than the Fermi level, the boundary between classically allowed and forbidden transmissions disappears. The prerequisites for a more realistic expression of the tunneling current and the resolving power would therefore be a modified theory by Bardeen and the simultaneous consideration of higher orbitals. However, this approach could no longer be calculated analytically. In the report [45] J. Chen deals in particular with the spontaneous changes in resolution during the

[1] For example $2k^{-1} \approx 1.6\,\text{Å}$ and $R + d \approx 15\,\text{Å}$ lead to a resolution of $A \approx 5\,\text{Å}$. [42]

measurement, which take place without changing the given parameters. He concludes that the resolving power depends strongly on the energetic states of the tip.

There are several other approaches for different applications to simulate and theoretically calculate measurements of an STM [46, 47]. The perturbation model of Tersoff and Hamann with neglected tip-sample interactions can be extended with the help of density-functional theory to provide good results [48, 49]. The density-functional theory in the generalized gradient approximation can also be used to calculate the magnetic and electronic structure and the DOS of the tip even for spin-resolved measurements. Depending on the tip material, different orbitals of the atoms at the apex are essential for the correct description [50]. However, the model is only sufficiently accurate at small bias voltages, otherwise, the model may break down [51].

Alternatively, an atom superposition model can be used as an approach, in which it is integrated over the LDOS of each surface atom at the apex of the tip, assuming that the LDOS of each surface atom contributes to the tunneling current. This approach has only been successful in some areas, but in contrast to the Tersoff-Hamann model, it is not possible to simulate a complete STM dataset correctly [52]. A third possibility is to use real-space Green functions within the framework of Landauer-Büttiker theory[2] to include incoherent tunneling processes and tip-sample interactions in the calculations. Here it is additionally found that electronic states localized in the STM tip contribute significantly to the conductance [53].

2.4. The Scanning Tunneling Microscope

Before discussing the individual measuring modes of the STM, the general design should be considered first. The basis of every STM is the measuring probe scanning over a conductive sample, which is mounted with a small distance d apart and connected by a control loop [Fig. 2.4]. A DC voltage V_0 is applied to the tunneling junction to allow the electrons to tunnel from tip to sample or vice versa, by lowering the potential barrier: a tunneling current $I(V_0, z)$ flows at a distance in the ångström range. The current is converted into a proportional voltage signal by a pre-amplifier placed close to the vacuum feed-through to avoid additional inductively coupled noise. The signal is amplified several times, then measured and passed on to a control loop for image generation. The feedback loop additionally adjusts the tip-sample distance [34].

The probe of the STM is usually a metallic tip that conducts the tunneling current and scans the sample. It is often made of tungsten or a platinum-iridium alloy because these materials allow the fabrication of sharp tips with a radius of tens of nanometers. The tip is attached to a piezoelectric tube, which is responsible for actuating the position of the tip in all three spatial directions. For spatially resolved measurements, the x- and y-directions are varied by a periodic signal from the scan generator to scan the sample line by line. The z-signal, i.e. the tip-sample distance, is adjusted by the feedback loop keeping the measured tunneling current at the set value [54].

[2] The Landauer-Büttiker formalism describes generally the current transport in the boundary channel model in systems of finite size.

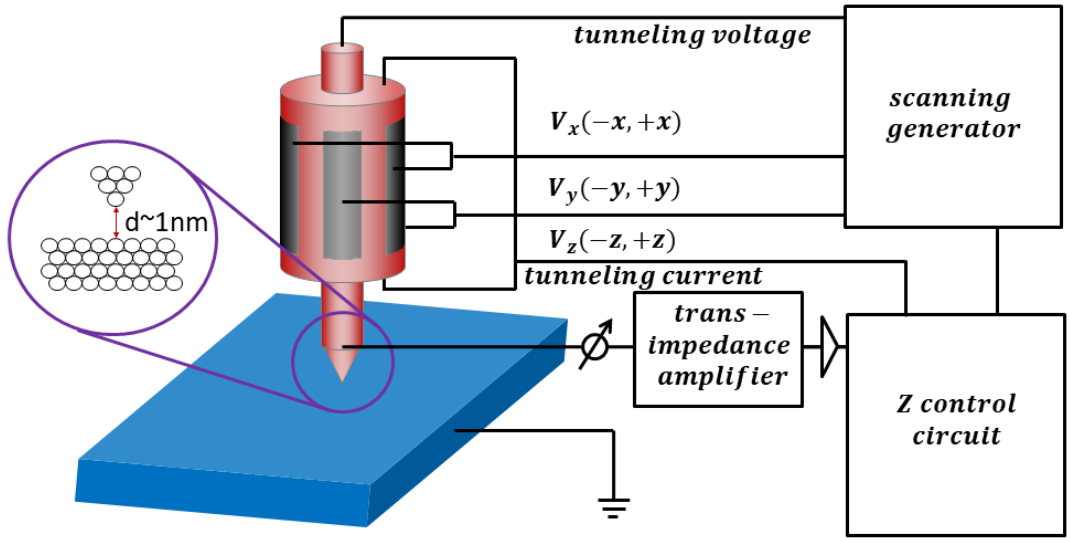

Fig. 2.4. Shown is the basic structure of an STM. Tip and sample are connected to a control loop which controls the z-position of the tip via a piezo tube and readjusts it depending on the tunneling current. The scan generator takes care of scanning the sample in x- and y-direction. The tunneling current signal gets amplified and converted into a voltage signal for further electronic processing. The measuring electronics comprise the scan generator and the control loop and are thus responsible for the entire control of the STM.

The piezoelectric effect describes the generation of a voltage by mechanical deformation of a crystal. The inverse piezoelectric effect is used for position control: the deformation of the crystal (piezo tube) is roughly proportional to the applied voltage. By applying electrodes on the piezo tube, the tip can be moved almost independently in x-, y- and z-direction with picometer accuracy.

The microscope must be insulated against mechanical and electrical noise. The distance between the sample and the tip is very small, so even the smallest mechanical vibrations can cause considerable interference with the measurement. To minimize vibrations the microscope can be suspended on springs and damped by eddy current brakes, like in the case of the system used in this thesis. A surge baffle system below the apparatus can also improve isolation. Furthermore, for good measurement results, it is recommended to place the microscope in the basement to minimize the influence of building vibrations [33]. Building vibrations are in the low-frequency range and cannot be easily removed by passive anti-vibration devices. Therefore, an active device is installed in our case. The damping system consists of two modules that carry the entire STM apparatus. The system uses vibration sensors to detect disturbing frequencies that are negated by vibrations of the same frequencies and amplitudes with destructive interference caused by vibrating piezo elements.

Another source of interference is the tunneling current signal itself: the tunneling current is in the nanoampere range, hence even the smallest electronic feedbacks or inductive loops cause interference with the tunneling current and are usually visible in the measurements [39]. Therefore, a well-thought-out cable routing and grounding of

the microscope is useful.

In the previous part, the theory of the microscope was examined, finding a dependence of the tunneling current on the applied voltage, the tip-sample distance, and the LDOS of tip and sample. There are several measurement modes to determine and separate the individual measurement quantities.

2.5. Methods of Measurement

For topographic measurements, the scan generator systematically moves the tip over the conductive sample surface. Usually, the image is recorded in the following manner: each line (x-direction) is recorded in the forward and backward direction, then the probe moves a defined step in y-direction and the next line is measured. The image is thus composed of line scans, whereby the line spacing and the pixels per line can be set in the measurement software. One obtains a backward and a forward image measured almost simultaneously.

Measuring the tunneling current at a fixed voltage results in an image showing the convolution of the surface structure with the electronic properties of the sample, more precisely a topography of constant conductivity. In contrast to the linear dependence of the tunneling current on the LDOS of the sample surface, it depends exponentially on the distance between the tip and the sample. Therefore the largest part of the tunneling current flows over the tip atom nearest to the surface. This makes the current particularly sensitive to the smallest changes in distance so that the surface topography is the main component of the recorded images [54].

Experimentally, image acquisition can be realized in several ways discussed in the next Section 2.5.1. The modes of constant-current and constant-height are most important for topographic imaging.

2.5.1. Constant-Height Mode

The constant-height mode (CHM) is based on a constant z-position of the tip. The z-component is therefore not varied by the control loop. Instead, it is kept at a constant value throughout the measurement, as well as the tunneling voltage. The sample is systematically scanned. The sample surface has to be very flat for CHM because otherwise, the tunneling current varies in a range larger than the pre-amplifier can handle. From the measurement of the tunneling current, the topographic image of the sample is calculated by the measurement electronics [55]. With CHM a very high scanning speed is possible because data acquisition is not limited by the feedback loop. This advantage is important for recording dynamic processes. A high scan speed can also reduce the influence of thermal drift[3].

[3] The thermal drift is an image distortion due to thermal effects: often the sample migrates in the nanometer range during the measurement.

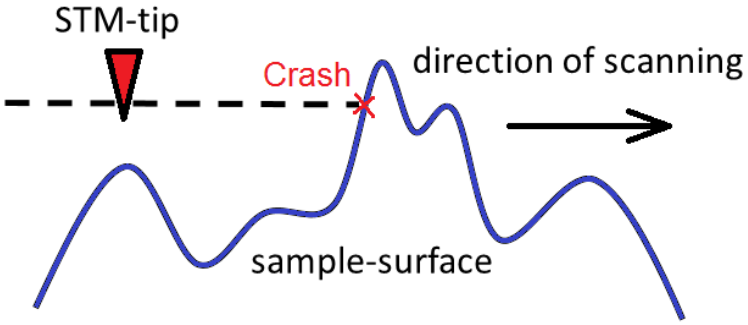

Fig. 2.5. The operation of the STM in CHM; the dashed line represents the path of the tip. The solid blue line represents the sample surface. Additionally, the possibility of a crash in this mode is shown.

However, CHM has a decisive disadvantage: a noticeably rough sample can lead to crashes[4] between the sample and the tip. A particularly flat sample is therefore a prerequisite to minimize the probability of contact between tip and sample. Adjusting the height of the tip is still difficult: the higher the tip, the weaker the signal, but if the tip is too low, it will collide. In principle, there is a loss of resolution accuracy because the distance between tip and surface should not be too small. Moreover, the resolution is not constant, due to the variation of the distance between tip and sample.

2.5.2. Constant-Current Mode

The constant-current mode (CCM) is the second important mode for topographic measurements with the STM. The nominal value of the tunneling current I_0 is fixed before the measurement is started. Therefore the distance between the tip and the sample remains constant and the tip must be continuously readjusted via the feedback loop depending on the tunneling current. The image of the surface is calculated from the z-voltage of the piezo tube [55].

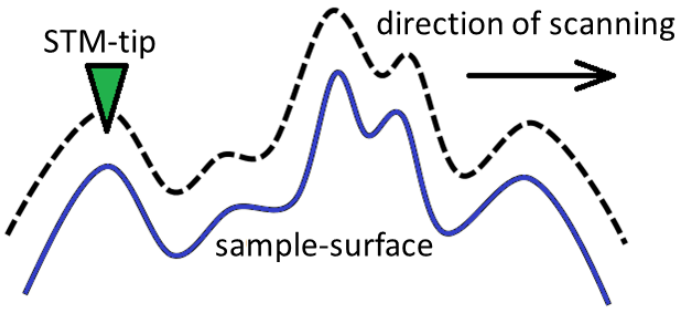

Fig. 2.6. The operation of the STM in CCM; the dotted line shows the path of the tip. The solid blue line represents the sample surface. Here, the probability of a collision between the tip and the sample is rather low.

[4] A contact between tip and sample results in at least a significant measurement error, as shown in Figure 2.5. A damaged or even destroyed tip or sample is in the worst case also possible.

The CCM often is the preferred measurement method since a collision between tip and sample can generally be avoided [Fig. 2.6]. In addition, unlike in the CHM mode, the image has a constant resolution. Due to the slower speed of the tip thermal drift can be a major problem in this mode. Apart from that, this method is much more time consuming because the feedback loop limits the scanning speed.

2.6. Spectroscopy

Scanning tunneling spectroscopy is the second important measuring method. STS is mainly used for obtaining information about the LDOS of the sample surface. In some cases, STS thus enables an element-specific resolution. Different recording methods are described below.

For the dI/dV spectroscopy the tip remains fixed in x-, y- and z-direction during the spectroscopy measurement [39]. After stabilizing the tip at a stabilization-voltage V_s, the feedback loop is switched off, and the voltage V is varied in a given range of typically a few volts. Thus, one measures the dependence of the tunneling current $I(V)$ on the voltage V. By differentiating the current numerically, one obtains d/dV, which is proportional to the LDOS. Alternatively, it is possible to measure the differential tunneling current directly, using a lock-in amplifier to suppress signal noise.

A very related type of spectroscopy is the dI/dV mapping. Here, the stabilization-voltage is the same as the voltage for the spectroscopic measurement. For a defined voltage, a spectroscopic measuring point is recorded, using the lock-in amplifier output as a second signal, while keeping the feedback loop on. In this case, x- and y-direction are variables, because the sample is scanned in the same way as for topographic measurements, resulting in an image of the LDOS at a defined voltage of a sample area [56]. To get an energy resolution, it is possible to measure dI/dV maps at different energies. For this method, a lock-in amplifier is needed. The lock-in amplifier adds a modulation voltage to the tunneling voltage, which is also reflected in the measured current signal. The amplitude of the current modulation depends on the slope of the $I-V$ curve at the stabilization voltage, resulting in the proportionality to the derivative dI/dV and thus to the LDOS. In the lock-in amplifier the input signal, i.e. the AC component of the tunnel current, is multiplied by the reference voltage and integrated over a certain time. The modulation frequency is limited by the preamplifier of the STM and different resonance frequencies. The input signal has besides the modulation frequency also other parts of disturbing frequencies. Multiplying the two signals of different frequency results in a beat frequency around zero, which does not contribute when it is integrated correspondingly long. Only the part, which has the same frequency as the reference voltage, delivers a non-vanishing contribution after integration, which is proportional to the amplitude and thus to the LDOS. To average other frequencies out optimally, the integration time must be as long as possible, i.e. several oscillation periods, leading to the disadvantage of very long measuring times of several hours.

Another variant is the $I(z)$ spectroscopy. Varying the z-position, i. e., the distance d between the sample surface and tip, at constant tunneling voltage results in a

dependency of the tunneling current $I(d)$ on the distance d. In this case, similar to dI/dV spectroscopy, the tunneling current must be differentiated according to the distance d to obtain information about the DOS [57].

For the tunneling process, there is a simple correlation: the higher the DOS, the higher the tunneling current. However, there are differences between different configurations. If a negative voltage is applied to the tip, the Fermi energy of the tip will be shifted upwards by $|e \cdot V|$, and the majority of the electrons tunnel from the Fermi edge of the tip through the potential barrier into the sample surface [Fig. 2.7]. For a positive voltage at the tip, the Fermi energy of the tip is shifted downwards, and the electrons tunnel from the sample into the tip [58].

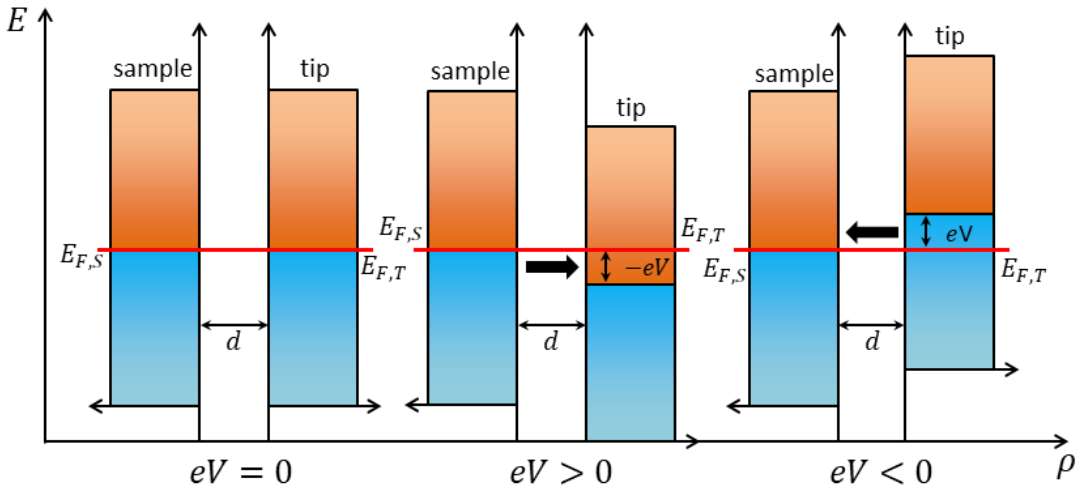

Fig. 2.7. The three possible cases of spectroscopy; sample and tip are each separated by a barrier of width d. Occupied states are marked in blue, unoccupied states in orange. In the first case, there is no voltage, so the Fermi energy of sample and tip are equal, and no electrons are tunneling. The second case $eV > 0$ assumes a positive voltage at the tip. The Fermi energy is shifted upwards, and the electrons tunnel from the sample surface into the tip, hence the occupied sample states are observed. $eV < 0$ is the opposite case: the negative tip voltage shifts the Fermi energy downwards, and the electrons tunnel from the tip to the sample. Now the unoccupied sample states are investigated.

For negative voltages, the unoccupied states of the sample are observed, for positive voltages the occupied states. By varying the voltage, the energy levels of the tunneling electrons and the number of the involved states in the tunneling process are changed as well. At suitable voltages, the electrons are tunneling into unoccupied, newly attainable surface states of the sample due to the energy shift, resulting in an abrupt increase of the tunneling current. This measurement technique provides information about the electronic structure of the surface and the LDOS at the spectroscopic location [59].

The expression for the tunneling current derived in Section 2.2 depends linearly on the tunneling voltage V. Differentiating the expression at constant distance d with respect to V results in a linear relationship between dI/dV and the DOS of the sample $D_p\,(E_F + e \cdot V)$:

$$\frac{dI}{dU} \sim D_t\left(E_F\right) \cdot D_p\left(E_F \pm e \cdot V\right) \cdot e^{-A\sqrt{\phi_{\text{eff}}}d}, \tag{2.25}$$

with $\sim D_t\left(E_F\right)$ the DOS of the tip. Using the differentiated tunneling current, an image of the LDOS of the sample surface is obtained experimentally.

A spatially resolved spectroscopic map of a sample surface also can be obtained by dI/dV or $I(z)$ spectroscopy. By taking many individual spectra in a mapping grid, it is possible to get an energetically and spatially resolved 3D-data array, but it is therefore comparatively time-consuming. During such a spectroscopy scan the scanner must not move, instead, it is moved between measurements in discrete, previously determined steps.

2.6.1. Spin-Polarized STS

The spin-polarized STS is a modification of STS. It additionally allows the observation and investigation of magnetic contrast. The magnetic contrast is obtained by a tip with a defined spin direction. This can be a ferromagnetic tip or even an antiferromagnetic tip because all that counts is the spin direction of the topmost atom at a tip. In the case of ferromagnetic tips, it is advisable to minimize the ferromagnetic material at the tip to avoid large stray fields that may alter the magnetization structure of the sample. Therefore, the tip is coated with a thin layer of a ferromagnetic material. By magnetizing the tip, electrons with the spin orientation matching the magnetization of the tip are more likely to tunnel than electrons with reverse spin orientation, where the spin is conserved during the tunneling. More precisely, the DOS of the tip is spin-dependent, and therefore, the tunneling current depends on the magnetization state of the sample. The same effect also leads to the tunneling magnetoresistance device used in spintronics.

The tunneling current reacts sensitively to changes in the magnetic properties of the sample. Spin-polarized STS can provide detailed information on the magnetic properties of the sample surface and their correlation to the morphology of the sample surface. Spin-polarized STS allows the precise analysis of magnetic dynamic and static processes of magnetism, for example, the properties of magnetic domains at the atomic level in ferromagnetic and antiferromagnetic systems [60].

2.7. Low-Energy Electron Diffraction

Low-Energy Electron Diffraction is a method for studying the atomic structure of surfaces. The method was developed in 1927 by Davisson and Germer on a Ni single crystal [61, 62]. The underlying effect is the wave interference of electrons reflected at a surface, which leads to the formation of diffraction patterns that are visualized on a fluorescent screen. LEED uses electrons with a de-Broglie wavelength λ depending on the energy E of the electron beam:

$$\lambda = \frac{h}{\sqrt{2mE}}. \tag{2.26}$$

Suitable energies are in the order of 100 eV. Therefore, the penetration depth of the elastically scattered electrons is low, which makes the method very surface sensitive. The LEED is usually operated in UHV and is structured as follows. Electrons are emitted from a hot filament and accelerated towards the sample by an anode. After the electrons have been scattered on the sample, the electrons pass grids in front of a luminescent screen. The first grid is at the potential of the sample holder preventing the distortion of the diffraction pattern by electrical fields between sample and detector. The second and third grid serve as a retarding device, at which the inelastically scattered electrons are reflected. The elastically scattered electrons are accelerated onto the screen that is on a high positive potential of several kilo-electronvolt. The accelerated electrons are converted into light by the luminescent screen.

The LEED pattern ideally comprises sharp spots arranged symmetrically around the (00) spot, representing the mirror reflected beam from the sample surface. Shape and size of the two-dimensional unit cell result from the position of the reflections. The intensities of the reflections significantly vary with the energy of the electrons, which is due to interference with atomic layers below the surface layer. This also offers the possibility to determine atomic positions along the surface normal. To determine the structure, the patterns are recorded with a camera at different energies, and the intensity of reflexes is determined from the images. The structure of the surface can be determined from these intensity curves [63]. Adsorbed molecules or surface reconstructions that form translationally symmetric structures with a larger unit cell than the substrate, lead to superstructure spots in the diffraction pattern. Similar superstructures can be observed when the lattice constants of substrate and adsorbed films are different, forming a moiré pattern.

3. Samples and Theory

This chapter reports the properties of the samples used for the experiments and the theoretical background that is necessary to understand the results of the thesis. First, the sample itself and the different metals that are deposited on it are discussed (Sec. 3.1). A discussion about an important concept for inverse melting, entropy (Sec. 3.2) follows, to get a better understanding of the mobility of Ni (Sec. 3.4) and inverse melting (Sec. 3.3) itself. In the second part, the electronic band structure (Sec. 3.5) is presented. Based on this the surface states (Sec. 3.6) and the Bychkov–Rashba effect (Sec. 3.7) are discussed.

3.1. Rhenium, Gold and Nickel

For the step decoration by submonolayer coverages, there are previous studies of the growth of different metals on Re(0001) [64, 65, 66]. At room temperature, Au and Ni grow at submonolayer coverage as compact single-layer islands. The island edges are mostly formed by close-packed atomic rows in three equivalent directions corresponding to the symmetry of the Re(0001) crystal lattice. The first layer of both metals is growing pseudomorphic. Starting with the second layer, the metals grow with their lattice constants. First, some general information about the metals used in the experiments is presented.

3.1.1. Rhenium

Rhenium is an element with the element symbol Re and the atomic number 75. In the periodic table of elements, it is in the 7th subgroup (manganese group). It is a very rare, hard, silvery-white shining, heavy transition metal. Re crystallizes in a hexagonal close-packed (hcp) structure with the lattice parameters $a = 276.1\,\mathrm{pm}$ and $c = 445.6\,\mathrm{pm}$ with two atoms per elementary cell. Re has a very high density of $21.03\,\mathrm{g/cm^3}$ [67].

With 3459 K Re has one of the highest melting points of all elements. The boiling point is also very high at 5903 K and below 1.7 K Re becomes a superconductor [67]. Although rhenium is not a precious metal, it is non-reactive at room temperature and stable to air. Only when heated it reacts with oxygen, starting at 670 K, to form rhenium (VII) oxide [68].

3.1.2. Gold

Gold is a slightly reddish-yellow element with the element symbol Au and the atomic number 79. It is a transition metal and in the 1st subgroup in the periodic table. Consisting of only one stable isotope, it belongs to the pure elements and can be easily alloyed with several metals. The heavy metal is unalloyed soft with a Mohs hardness of 2.5 to 3, but has a high density of 19.32 g/cm^3. The melting point of Au is 1337.33 K, the boiling point is much higher at 3243 K [67].

Au has very high ductility and elasticity, is unreactive at room temperature and very stable to air. It crystallizes exclusively in a face-centered cubic (fcc) space lattice and thus exhibits the densest cubic spherical packing. The lattice parameter for pure gold is $c = 407.82$ pm with four atoms per unit cell [67].

3.1.3. Nickel

Nickel is a silvery-white chemical element with the element symbol Ni and the atomic number 28. It belongs to the transition metals and in the periodic table, it is in the 10th subgroup (nickel group). With a density of 8.91 g/cm^3, it also belongs to the heavy metals. It is medium hard with a Mohs hardness of 3.8 [67].

Like iron and cobalt, nickel is ferromagnetic, with a Curie temperature of 627 K. The metal crystallizes in a fcc crystal structure with the lattice parameter $a = 352.4$ pm with four formula units per unit cell. It has comparably high electrical and thermal conductivity but, with an fcc crystal structure, the melting point is located comparatively high at 1728 K, so it melts at much higher temperatures than gold but has a lower boiling point of 3003 K [67].

3.1.4. Growth

Thin films grow very differently, depending on the material and surface. Also, impurities on the surface often lead to a change of the surface energy and thus, to a change of the contact angle. Growth over monoatomic layers is called two-dimensional growth or Frank-van der Merwe growth [69, 70] [Fig. 3.1 b)]. Here, the thin film grows evenly layer by layer because the adsorbate-surface and adsorbate-adsorbate interactions are balanced, and the surface energy is isotropic. The Frank-van der Merwe growth additionally requires a lattice matching.

In contrast, Volmer-Weber growth is a three-dimensional growth mechanism [71] through the formation of droplet-like nuclei [Fig. 3.1 a)]. The Islands grow directly on the surface of the substrate and no coating layer is formed. The Volmer-Weber growth leads to a large surface resulting in structures that can exhibit the properties of nanoparticles. This growth mode indicates that adsorbate-adsorbate interactions are stronger than adsorbate-surface interactions.

Between the two growth modes exist a variety of intermediate modes, which can be summarized as Stranski-Krastanov growth [72]. First, a wetting layer is formed, which can consist of one or more layers. Beyond a critical film thickness, which depends

on the strain and chemical potential of the film, the growth continues through the formation of islands.

Au and Ni also grow on Re in a quasi Frank-van der Merwe mode. If a small amount of Au or Ni adsorbs on a crystal surface such as Re(0001), no homogeneous film will be formed. Instead, the deposited metal accumulates in small monolayered, disordered islands, but the second layer only grows after the first layer is ≈ 90% complete [66]. The growth changes from the fourth monolayer onwards and changes into a three-dimensional Volmer-Weber growth. The growth characteristics can be explained by the mobility of adsorbed atoms with high kinetic energy from the evaporation process. The deposited metal can only form closed films when the surface free energy, which depends on the sample material and layer thickness, is large enough.

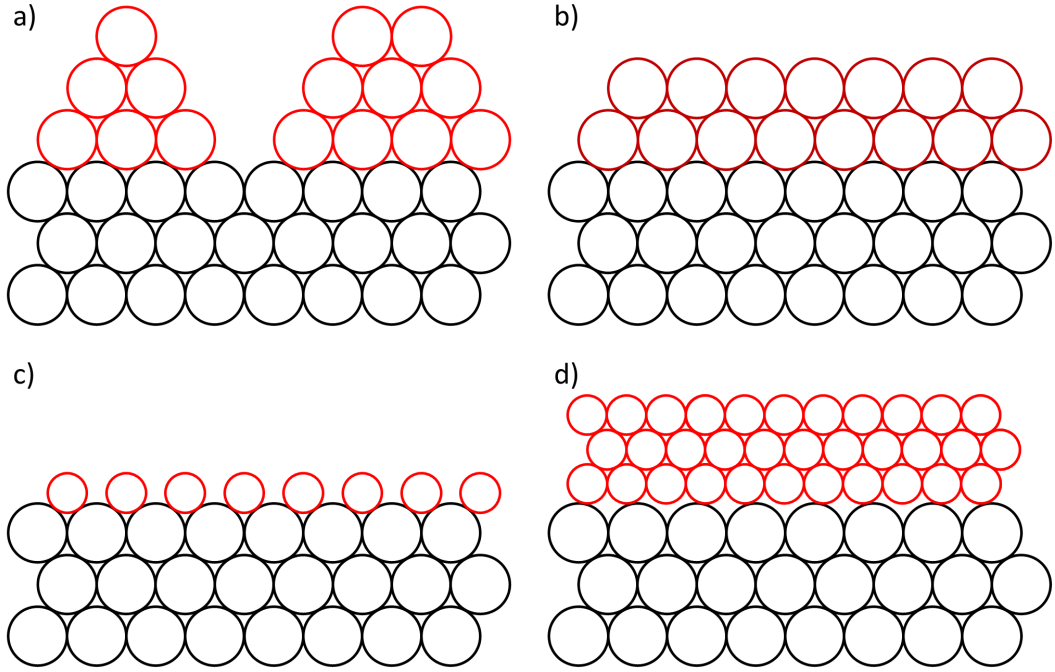

Fig. 3.1. Shown are different growth mechanisms: a) Volmer-Weber growth, forming directly three-dimensional islands; b) Frank-van der Merwe growth, forming successively closed monolayers; c) Pseudomorphic growth; adopting the crystal structure of the underlying crystalline substrate; d) Epitaxial growth; growing in at least one crystallographic orientation as well as in the underlying substrate.

A completely closed layer can be achieved, for example, by increasing the thermal energy through so-called annealing. By increasing the mobility of the atoms, the surface structure changes. The adsorbed atoms diffuse to form larger islands, closed layers, or step edge decorations to achieve an energetically more favorable configuration. The change in growth strongly depends on the annealing temperature. In the comparable Ni/Ru(0001) system, closed monolayers are formed between 700 K and 1100 K. At higher temperatures, three-dimensional islands form [73, 74].

In general, a distinction is made between pseudomorphic and epitaxial crystal growth on crystalline substrates. A pseudomorphic growth is defined by the fact that the deposited

layer adopts the crystal structure and the lattice constants of the underlying substrate [Fig. 3.1 c)]. In contrast, most metals grow epitaxially at larger coverages. Epitaxy describes the form of crystal growth when at least one crystallographic orientation of the growing crystal corresponds to an orientation of the crystalline substrate [Fig. 3.1 d)]. The deposited metal thus grows with its own lattice constant but in the same orientation as the substrate [75, 6]. Au and Ni grow pseudomorphically on Re in the first monolayer. From the second layer on, an epitaxial growth starts.

3.1.5. Mismatch

Due to the different lattice constants of the substrate and adsorbed metals, the crystal lattices do not fit perfectly when Au or Ni are deposited on Re(0001). Since the first layer of both metals grows pseudomorphic, the atoms of the film grow with a different lattice constant than they would have in bulk. This so-called mismatch leads to a considerable strain in the adsorbed film. This strain can increase again due to the different thermal expansion coefficients of the metals. The growth direction of the step decorations also must be considered. The crystal lattices of Re, Au, and Ni are all a close-packing of equal spheres and both metals, Au and Ni, grow on Re(0001) in the (111)-direction. A geometric pre-factor for the calculation of the mismatch of $1/\sqrt{2}$ must be taken into account. At room temperature, the mismatch of Au(111) and Re(0001) is:

$$m_{\mathrm{Au}} = \frac{\frac{\sqrt{2}}{2} \cdot a_{\mathrm{Au}} - a_{\mathrm{Re}}}{a_{\mathrm{Re}}} = +4.45\,\%. \tag{3.1}$$

The mismatch between Ni(111) and Re(0001) is with $m_{\mathrm{Ni}} = -9.74\,\%$ considerably larger. The plus sign means that the atomic distances in the crystal lattice of Au are larger than those of Re, while those of Ni are smaller. Therefore, the Au film is compressed while the Ni film has tensile strain.

At $T = 4.6\,\mathrm{K}$ the different expansion coefficients of the metals must be taken into account. Assuming a temperature-independent linear expansion coefficient α, the change in length can be described using the following formula:

$$L = L_0 \cdot (1 + \alpha \Delta T)\,, \tag{3.2}$$

where ΔT represents temperature difference and L_0 describes the length of the material at room temperature, in this case, the lattice constant. Since Re with $\alpha_{Re} = 6.2 \times 10^{-6}\,\mathrm{K}^{-1}$ has a smaller thermal expansion coefficient than Au with $\alpha_{Au} = 14.2 \times 10^{-6}\,\mathrm{K}^{-1}$ and Ni with $\alpha_{Ni} = 13.4 \times 10^{-6}\,\mathrm{K}^{-1}$ the mismatch of the lattice constants changes at cold temperatures [67]. This results in a reduction to $m_{\text{Au-LHe}} = 4.21\,\%$ for the Au/Re mismatch, but an increase to $m_{\text{Ni-LHe}} = -9.94\,\%$ for Ni/Re, which further increases the strain in the first layer at low temperatures.

3.1.6. Strain

The pressure within a system is a decisive variable for inverse melting. In one and two dimensions, the equivalent of pressure is strain. The strain σ of a body can be calculated using Hook's law [76]:

$$\sigma = E \cdot \epsilon, \tag{3.3}$$

with E being Young's modulus and $\epsilon = (l - l_0)/l_0$ the relative length expansion. For thin plates, i.e., two-dimensional planes, this law can be extended by introducing the Poisson number ν, which represents the ratio of Young's modulus and the shear modulus. This results in the following tensor equation for the three-dimensional tension vector $\vec{\sigma}$ [77]:

$$\begin{pmatrix} \sigma_{xx} \\ \sigma_{yy} \\ \sigma_{xy} \end{pmatrix} = \frac{E}{1-\nu^2} \begin{pmatrix} 1 & \nu & 0 \\ \nu & 1 & 0 \\ 0 & 0 & \frac{1-\nu}{2} \end{pmatrix} \begin{pmatrix} \epsilon_{xx} \\ \epsilon_{yy} \\ 2\epsilon_{xy} \end{pmatrix}. \tag{3.4}$$

For the system Re(0001) with a coverage of one pseudomorphic monolayer this results in a strain of $\sigma_{300\,\mathrm{K}} = 32.07\,\mathrm{GPa}$ at room temperature with $E = 205\,\mathrm{GPa}$ [78]. At $T = 4.6\,\mathrm{K}$ this pressure on the Ni atoms increases further to $\sigma_{4.6\,\mathrm{K}} = 32.80\,\mathrm{GPa}$ according to the mismatch of the lattice constants. In comparison, Au on Re(0001) has a much lower strain of $\sigma_{\mathrm{Au}} = -5.53\,\mathrm{GPa}$ at $T = 4.6\,\mathrm{K}$ with $E = 78\,\mathrm{GPa}$ [78].

This high strain within the layer can be relieved in several ways, including the formation of holes, defects, or dislocation lines. The formation of moiré patterns also causes a significant relaxation within the surface. For example, starting with the second monolayer, a moiré pattern with a 10×10 superstructure is formed in Ni Film, which continues to the twelfth monolayer. Therefore the development of a moiré pattern is energetically very favorable. In the example of Ni, it reduces the remaining strain at $T = 4.6\,\mathrm{K}$ to 0.29%, remaining constant in the wider range of thicknesses [66, 79].

3.2. Entropy

Entropy is a fundamental thermodynamic state variable. At the beginning of the 19th Century, Carnot contemplated thermodynamic cycle processes. He discovered that mechanical work can be completely transformed into heat but that the complete retransformation of heat into mechanical work is impossible. Clausius took up this idea and tried to quantify it. For this purpose, he introduced the state function entropy S. Looking onto a process from an initial state A to an end state B he formulated [80]:

$$S(B) - S(A) \geq \int_A^B \frac{\delta Q}{T}. \tag{3.5}$$

The energy at temperature T transmitted from a heat reservoir to the system of the heat engine is described by δQ. Clausius generally distinguished between reversible and irreversible circular processes, hence the equal sign applies for a reversible transition and the larger-than sign for irreversible transition processes. Processes in which the entropy in a system increases are called irreversible. They can only be reversed if another system absorbs the entropy.

The entropy differential according to Clausius can be further reformulated with the help of the first law of thermodynamics, $\mathrm{d}U = \delta W + \delta Q$. Taking advantage of the fact that the work $\delta W = (-p\,\mathrm{d}V + \mu\,\mathrm{d}N + \dots)$ consists of all processes possible for the experimenter. Additionally, changing the system variables results in:

$$\mathrm{d}S \geq \frac{\delta Q_{\mathrm{rev}}}{T} \geq \frac{1}{T}\left(\mathrm{d}U + p\,\mathrm{d}V - \mu\,\mathrm{d}N - \dots\right). \tag{3.6}$$

The supply of heat or matter causes an increase in entropy in a system as all spontaneous processes within the system do, such as mixing, heat conduction, chemical reaction, or conversion of mechanical energy into thermal energy by friction. The entropy of a system can only decrease by the release of heat or matter. Therefore, the entropy can never decrease in an isolated thermodynamic system. Thus, Clausius established one of the different formulations of the second law of thermodynamics: for two successive equilibrium positions in an isolated system one obtains:

$$S(t_2) - S(t_1) \geq 0 \quad \text{with} \quad t_2 > t_1. \tag{3.7}$$

Boltzmann built his definition of entropy on a different foundation. By using the definition of the internal energy, he found a statistical description based on a microscopic level: a new formulation for the macroscopic state function entropy. The entropy S of a macrostate is calculated by the probabilities p_i of the microstates i with the proportionality factor k_{B}, the Boltzmann constant [81]:

$$S = -k_{\mathrm{B}} \sum_i p_i \ln(p_i) = k_{\mathrm{B}} \ln \Omega. \tag{3.8}$$

Strictly speaking, entropy is proportional to the logarithm of the phase space volume associated with the values of the thermodynamic variables. In an isolated system, the spontaneous internal processes in the statistical mean are leading the system to approach the macrostate, which has the highest possible entropy for the same energy.

Phase Space Volume

The canonical equations of classical mechanics describe the temporal evolution of the system, the phase trajectory. All phase points, called microstates, which can be reached under given macroscopic boundary conditions, such as total energy E, volume V, and particle number N, form a coherent phase space volume Ω. The fundamental assumption of statistical thermodynamics is that the occupation of any microstate is assumed to be equally probable $p_i = 1/\Omega$. With Ω, the number of microstates, this assumption is usually justified for an isolated system in equilibrium.

Internal Energy

The internal energy U is the total energy available for the thermodynamic conversion processes of a system in thermodynamic equilibrium. The internal energy is composed of a variety of other forms of energy, such as heat Q and work W. It is constant in a closed system according to the first law of thermodynamics. The internal energy only changes when the system exchanges heat or work with its environment. It is therefore an extensive state variable and a thermodynamic potential of the system.

Macrostate

A macrostate describes a defined system with many degrees of freedom, which is described by macroscopic, averaged state variables such as energy, temperature, volume, pressure, chemical composition or magnetization. The macrostate of a system becomes more probable the higher its entropy is. Thus, entropy is determined by the number of accessible, energetically equivalent microstates. A thermodynamic system with a given macrostate occupies different microstates of energy E_i with a certain probability p_i. Many parameters of the system can be calculated from these microstates.

Microstate

A microstate is given by determining all locations and momenta of the particles of a system. A microstate $(\vec{q}, \vec{p})$ is therefore a point in a 6N-dimensional space, which in this context is called phase space. Hence, it is the complete microscopic description of a thermodynamic system. A microstate thus corresponds to a point in the phase space of the whole system.

Boltzmann's approach is based on energy conservation and the observation that two systems have the same temperature in thermal equilibrium. Due to the countability of Ω it is in principle possible to calculate the entropy of each system in equilibrium. In contrast to Clausius' definition of entropy, which is limited to processes involving heat

exchange, Boltzmann's concept of entropy can be applied to any macroscopic system in equilibrium. Entropy can thus be defined as the missing knowledge of the energy distribution or as a measure of the lack of knowledge of the states of all individual particles.

3.3. Inverse Melting

Inverse melting is a counter-intuitive and very rare phenomenon. In general, IM is defined as a transition from a phase with a higher-order to one with lower order by reducing the temperature [4], first predicted by G. Tammann in 1903 [5]. Tammann designed a phase diagram for crystalline and liquid/amorphous phases [Fig. 3.2]. The curved line is the function of the melting temperature versus pressure and defines the boundary between the crystalline and the liquid/amorphous regions. Furthermore, two straight lines can be found along which the volume difference, i.e., the entropy difference, disappears.

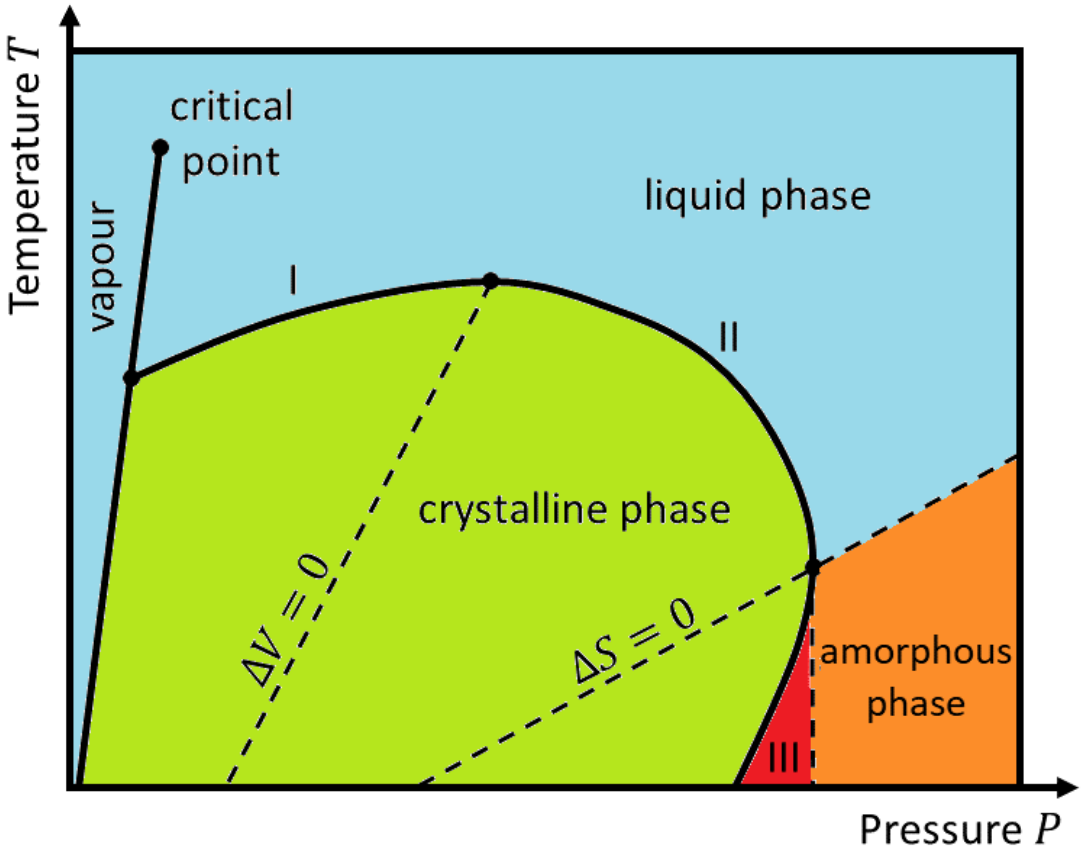

Fig. 3.2. The pressure-temperature phase diagram from Tammann [5]; the melting curve separates the crystalline area (green) from the liquid phase. This phase further can be divided into liquid (blue) and amorphous (orange) phase. Normal melting takes place in zones I and II. Inverse melting is found in the third zone (red), which is defined by the region between the vertical tangent and the melting boundary.

In area I [Fig. 3.2], normal melting occurs with an increase in volume and temperature. In area II, the curve has an opposite slope, the temperature increases while melting but the volume decreases, as in the case of phase transition from ice to water. In region III, the slope is reversed once again: temperature and volume are decreasing simultaneously. This is the area of inverse melting. The transition from a crystalline phase to the liquid phase, in contrast to the transition from liquid to vapor, does not have a critical point from which the two phases become indistinguishable, hence there is a symmetry breaking between the crystalline and liquid phase. Thus, the loop shape of the melting curve prevents the extension of this curve to infinity. For a long period, IM was only observed under extreme conditions, such as high pressure.

The first observation of IM as a reversible process at moderate conditions has been reported by Rastogi et al. in 1999 [82] when studying a phase transition on poly(4-methylpentene-1) molecules from an amorphous to a crystalline phase at about $T = 400\,\mathrm{K}$ between 2 kbar and 4 kbar. At first sight, the IM in this system causes an entropy inversion, which means that the order of the system through heat dissipation increases. But in the loosely packed lattice of poly(4-methylpentene-1) molecules, the variational entropy growth is larger than the loss of configurational entropy of the solid. The ordered crystalline or frozen amorphous phase has higher entropy than the disordered state, which means a high short-range ordering and a low long-range ordering of the crystal. This is unusual because the seemingly disordered state has a higher-order and respectively higher symmetry. The loss of entropy due to freezing has to be compensated by a higher degree of disorder in some other characteristic parameter. For example, the increase of the degrees of freedom, which are coupled to the position of the center of mass, contributes to an increase in the amount of such excitations [83]. Such behavior often is found in systems of highly degenerate order.

IM also has been found in several binary, metallic alloys based on the early transition metals combined with late transition metals. In the metastable crystalline bcc Ti-Cr alloy, an amorphous state near the glass transition temperature is polymorphously generated. This reversible process occurs in the temperature range between 900 K and 1100 K [84, 85].

IM has been found in two dimensional systems like molecular arrangements [86] and ultra-thin magnetic Fe films on Cu(100) that are magnetized perpendicularly to the film plane [87]. For the latter, a temperature increase from low temperatures to room temperature transforms a stripe domain structure into a labyrinth structure of higher symmetry within several hours. The transition is driven by an increase of topological defects, such as dislocations and disclinations that lead to a straightening of the labyrinth pattern when the temperature is increased even further.

3.4. Mobility of Ni

Considering the thermal stability of Ni, the mobility of Ni atoms at low temperatures has never been reported, and it is more than unexpected but at moderate temperatures, various investigations were carried out. The mobility of Ni adatoms has previously been investigated mostly for bulk samples and on tungsten substrates [88]. Low-temperature

movements of single Ni atoms on W(110) have been investigated at $T = 178\,\mathrm{K}$ by Field-Ion-Microscopy (FIM) [89]. Further investigations showed that for dimers, linear chains, and clusters higher temperatures up to $T = 370\,\mathrm{K}$ are needed to cause a movement [90]. The larger a cluster is, the more energy is required to increase individual atomic mobility, therefore, the clusters move as a unit. Additionally, it is assumed that higher stability is caused by a better lattice match between substrate and adsorbate lattice parameters [90].

One of the central results of the FIM studies of Ni is the very high mobility of Ni on W(110) [88, 89, 90]. Another study concerning Ni films with two or more monolayers reported moving atoms in measurable rates at a temperature range of 350 K to 460 K, while the first layer needs higher activation energy than subsequent layers [91]. The moving process is controlled by diffusion of second and higher layers of Ni above the first layer. This moving mechanism of Ni atoms on the tungsten surface at the layer edge called "unrolling carpet" mechanism, is based on the comparably low activation energy of 0.93 eV.

A mobility study of Ni clusters shows two changes in mobility with increasing temperature [92]. At about 60 K the first abrupt increase of mobility takes place, and the Ni clusters assume a pre-melting state. The second change occurs at about 1000 K, where Ni transforms into a liquid-like state. This behavior significantly differs from bulk behavior and opens the question of whether bulk clusters and two-dimensional systems of the same element can exhibit a different phase transition behavior. In a study published in 1995 [93] of Ni on Ru(0001), an element with a very similar lattice structure to Re(0001), the growth of Ni within the first monolayers was investigated. In the STM experiments at room temperature, a strongly increased mobility of the Ni atoms was assumed but could not be shown conclusively.

Stindtmann et al. [66] investigated the growth of Ni on Re(0001) using STM. This study shows that the deposited Ni atoms, at least for the first 3 ML, can move freely across step edges and see no Ehrlich-Schwoebel barrier at room temperature. Consequently, one observes a layer-by-layer (Frank-van der Merwe) growth mode for the first 3 ML. Also, speckles and small clusters were observed at larger coverages in the STM images, indicating that these Ni clusters move easily on the surface and can be pulled around by the STM tip [66].

3.5. Electronic Band Structure

The electronic band structure describes the states of electrons and holes of a crystalline solid in momentum space and is thus the dispersion relation of electrons under the influence of a lattice potential. Several macroscopic properties can be understood via the electronic band structure, such as electrical, thermal, and optical properties as well as transport properties.

The electrons of a single atom occupy atomic orbitals with discrete energy levels. If two or more atoms join together to form a molecule, their atomic orbitals will overlap. The Pauli principle states that not all quantum numbers of two electrons may coincide. So, when two identical atoms join together to form a molecule, the atomic orbitals

split into molecular orbitals of different energies so that the electrons can occupy the new orbital structure without violating the Pauli principle.

Similarly, the number of states extends when many identical atoms form a solid: In a crystal lattice, for example, the atomic orbitals of adjacent atoms overlap. Here, too, the Pauli principle comes into play, which again leads to energy splitting. Because of the large number of atoms in a solid, the number of orbitals becomes very large and the energetic distance very small. The energy of neighboring levels is close enough to regard them as a continuum, a so-called energy band. This band formation is usually a feature of the outermost valence electrons in the atom since the inner electron orbitals do not overlap significantly so that their bands are very narrow [94].

Band structure calculations exploit the periodic nature of a crystal lattice and its symmetry. In principle, the crystal is approximated using a single-particle Schrödinger equation and solved with the aid of ansatz functions in the form of Bloch functions [95]. There are a lot of different methods to calculate the electronic band structure, some of them are briefly introduced here.

Nearly free Electron Approximation

The nearly free electron model extends the free electron model by a weak periodic electrostatic potential for the approximate description of the positively charged atomic nuclei in the crystal lattice. First, the periodicity of the energy bands in the reciprocal space is used, which, taking into account a small lattice potential, has a band gap at the zone boundaries. The model allows a theoretical prediction of the band gap and thus a division of the solids into electrical conductors, semiconductors, and insulators and forms the foundation of the band model. As in the free electron model, the electrical interactions of the electrons with each other are not considered. Therefore, it is more accurate when the atoms are close together and the overlap between the orbitals is large, as is the case in some metals, for example [96].

Tight-Binding Model

The opposite of the nearly free electron approximation is the tight-binding model, assuming the electrons in the crystal behave more like an assembly of constituent atoms. Hence, it is based on the superposition of wave functions of isolated atoms, expressed by a linear combination of the atomic orbitals. The tight-binding model works well in materials with a small overlap between atomic orbitals on neighboring atoms, for example, semiconductors, and can be combined with other models. Due to the atomistic approach, the model also provides a basis for the calculation of surface states and an application in various kinds of many-body problems and quasiparticle calculations [97].

Density-Functional Theory

The density-functional theory (DFT) is based on the location-dependent electron density and the Hohenberg-Kohn theorem [98]. It says that the ground state of a system of N electrons is clearly defined by the location-dependent electron density. Therefore, only the electron density in the quantum mechanical ground state is needed. From this, theoretically, all other properties, the so-called functionals, can be determined. Therefore the core problem of the DFT is to find the corresponding functional. The advantage is that the complete solution of the Schrödinger equation is not necessary for the many-electron system. Therefore, calculations of larger systems with today's computing power are possible. Nevertheless, calculations of the properties of complex molecules or crystals using density functional theory are very complex. There are numerous extensions of the theory and combinations with other approaches [99].

Dynamical Mean-Field Theory

The dynamical mean-field theory (DMFT) is a method for determining the electronic structure of strongly correlated materials. In such materials, an approximation of independent electrons, as in DFT, does not lead to a fitting solution. The DMFT, therefore, works by a non-perturbative treatment of the local interactions between electrons [100]. By mapping a multi-body lattice problem to a local multi-body problem, the DMFT makes the calculations possible. In this case, an approximation is only that the lattice self-energy is assumed to be momentum independent. However, the mapping itself does not represent an approximation. Just like the DFT, this method can be extended and combined in many different ways [99].

Plotting the energy E of the electrons in a diagram versus their wave vector $\vec{k}$ results in the dispersion relation $E(\vec{k})$. This band structure diagram is also called a zone diagram, where overlaps and gaps of bands can occur. Distinctive points in the band structure are the symmetry points, such as the Γ point at $\vec{k} = (0, 0, 0)$. Here is the $\vec{p} = \vec{k} = \vec{0}$. Depending on the crystal structure, certain propagation directions are energetically more favorable. These can be recognized as minima in the zone diagram and have a higher charge carrier density.

The parabolas that are symmetric around the Γ point can be approximated by a parabolic energy dispersion relation depending on the wave vector $\vec{k}$:

$$E\left(\vec{k}\right) = \frac{\hbar^2 \vec{k}^2}{2m^*} + E_0, \tag{3.9}$$

with m^*, the effective mass. The idea of an effective mass is that the electrons and holes in the potential of a crystal behave like they were free particles in a vacuum, with

only a different mass. Compared to the electron mass m_e, statements about the crystal and the potential can be made, and it is an important parameter for determining transport phenomena [101, 102].

Band structures of real crystals can be very complex. Often several approaches have to be combined or modified to obtain an approximate mapping of the bands of a crystal. For example, in Fig. 3.3 the band model of a pristine Re single crystal is shown. It was calculated using DFT and the result is represented by the Bloch spectral density function [26]. Even small inhomogeneities or lattice errors can have a large impact on the model. Thin layers as well as interfaces and surfaces add new constraints to the models provoking additional electronic states. The symmetry breaking at surfaces also results in additional states, the so-called surface states, which have to be considered in the band model.

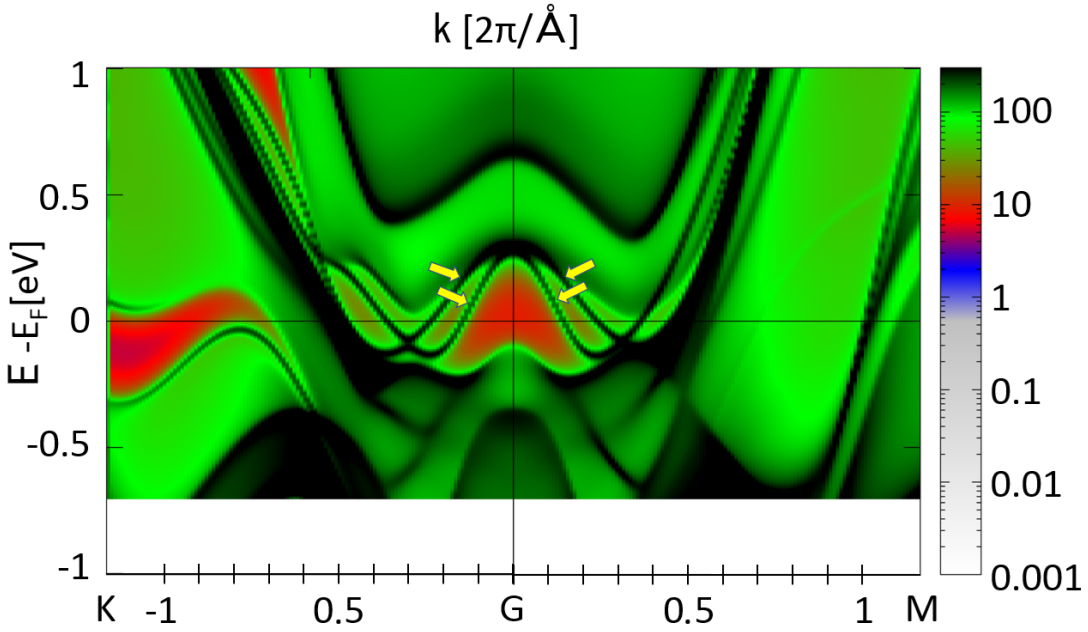

Fig. 3.3. A theoretical band structure of Re calculated by DFT; the Figure represents the Bloch spectral density function [26]. The two inverted parabolas in the center of the model symmetrically around the Γ point represent the Rashba split surface states (marked by yellow arrows). Bulk states are also visible.

An energy range within the band model, where no state exists, is called a band gap. If the Fermi energy lies within this gap the material is insulating without thermal activation. Depending on the width of this energy range, materials can be divided into semiconductors or insulators. In general, the band structure is always filled with the available electrons up to the Fermi energy E_F [96].

The highest occupied state is called the highest occupied molecular orbital (HOMO), the first un-occupied state is called the lowest-occupied molecular orbital (LUMO). In equilibrium, the Fermi energy is between them. The DOS $D(E)$ is a physical quantity that indicates the number of states per energy interval dE in a physical system. The DOS can be calculated by integration in k-space over the first Brillouin zone of a band structure [96].

3.6. Surface States

Surface states are electronic states that are localized at the surface of solid matter. Since the atoms of a body at the surface have fewer neighboring atoms, the forces at the surface are different from those within the bulk. The lack of neighboring atoms leads to weakened potential and costs energy. Therefore, new electronic levels and changed physical effects are formed on the surface. Surface states only are found in the atomic layers closest to the surface and decay exponentially with increasing distance from the surface.

There is a general difference between true surface states and surface resonances. Surface states are characterized by energy bands that are not degenerated with bulk energy bands. Hence, for the formation of surface states, a projected band gap along k_z is necessary. This means that no volume state with the corresponding energy and a parallel pulse in k_{xy} direction exists, thus there is a forbidden energy gap. A surface state can occur in the projected band gap, which is strongly localized at the surface. Therefore, the amplitude of a surface state always decreases exponentially with increasing distance from the surface, i.e., in the vacuum direction as well as in the bulk direction.

The surface resonance, on the other hand, has a connection to volume bands and therefore does not require a band gap. The state does not decay exponentially in the direction of volume, but only in the direction of vacuum. This means that surface resonances are also new states that occur due to the symmetry breaking at the surface, but with less surface localization. Therefore, surface resonances can propagate deep into the volume while retaining an enhanced amplitude close to the surface. A surface state band can also change into a surface resonance with varying energy when the band leaves the area of the projected gap. In contrast, volume states generally show a dispersion with k_z.

A general distinction is made between Shockley states [103] and Tamm states [104]. There is no real physical distinction between the two terms, but the mathematical approach for describing the surface states is different, as explained in the following section.

3.6.1. Bloch Wave

The Bloch wave is the solution of the stationary Schrödinger equation for a particle in a periodic potential [95]. The shape of the wave functions ψ is determined by the Bloch theorem. Let there be a periodic potential $V(\vec{r})$ with the periodicity $\vec{R}$:

$$V(\vec{r}) = V(\vec{r} + \vec{R}), \tag{3.10}$$

then a basis of solutions of the stationary Schrödinger equation exists:

$$\psi_{\vec{k}}(\vec{r}) = e^{\mathrm{i}\vec{k}\cdot\vec{r}} \cdot u_{\vec{k}}(\vec{r}) \tag{3.11}$$

with a vector $\vec{k}$ and a periodic function $u_{\vec{k}}(\vec{r})$ depending on the parameter $\vec{k}$ with period $\vec{R}$: $u_{\vec{k}}(\vec{r}) = u_{\vec{k}}(\vec{r} + \vec{R})$.

The periodicity of the potential $V(\vec{r})$ is thus transferred to the probability density $|\psi(\vec{r})|^2 = |\psi(\vec{r} + \vec{R})|^2$ of the particle under consideration. Hence, for an electron the probability density in each elementary cell is the same. In a crystalline solid the periodicity is given by the crystal lattice.

3.6.2. Shockley-States

Shockley states are surface states that are created as solutions of the Schrödinger equation in the approximation of nearly free electrons for an ideal surface [103]. They originate from the change of the electron potential at the transition between crystal and vacuum. This approach is suitable for the description of normal metals and some semiconductors with narrow gaps.

Since real surface states are very complex states with many factors to consider, a simpler model of a surface is used for understanding the basics. A monoatomic linear chain ending at one end is a good approximation, which can be solved by the Schrödinger equation in near-free-electron approximation. With this model, it is possible to derive the essential properties of surface states and to generalize the results from a two-dimensional surface of an ideal crystal. In this model, the end of the chain represents the surface of the body. Within the crystal, the potential is assumed to be periodic with the periodicity of the lattice. A Bloch wave is used as a basic solution, which represents eigenstates of the one-electron Schrödinger equation in a perfectly periodic potential [12]:

$$\phi_{\mathrm{ss}}\left(\vec{r}_{||}, z\right) = u_{\vec{k}_{||}}\left(\vec{r}_{||}, z\right) \exp\left(i\vec{k}_{||} \cdot \vec{r}_{||}\right), \tag{3.12}$$

with $\vec{r}_{||} = (x, y)$ and $\vec{k}_{||} = (k_x, k_y)$, the coordinates and the wave vector parallel to the surface. The modulation function $u_{\vec{k}_{||}}$ has the periodicity of the surface. Starting with the Schrödinger equation:

$$\left[-\frac{\hbar^2}{2m}\frac{d^2}{dz^2} + V(z)\right]\psi(z) = E\psi(z), \tag{3.13}$$

and the periodic potential $V(z)$:

$$V(z) = \begin{cases} 2\hat{V}\cos\left(\frac{2\pi z}{a}\right), & \text{for} \quad z < 0 \\ V_0, & \text{for} \quad z \geq 0 \end{cases} \tag{3.14}$$

The surface ($z = 0$) is modeled by a simple potential step V_0, which is an oversimplification for any realistic surface. The electronic wave function must be taken in the lowest-order approximation, as a superposition of two plane waves:

$$\psi(z) = Ae^{\mathrm{i}k_\perp z} + Be^{\{\mathrm{i}[k_\perp - (2\pi/a)]z\}}. \tag{3.15}$$

The solution must be calculated independently for the two ranges $z < 0$ and $z > 0$. The simplest possible solution is based on pure Bloch waves due to the periodic potential inside the crystal [Fig. 3.4 a)]. The solution inside the crystal is a linear combination of an incident wave and a wave reflected from the surface. Outside the crystal, the wave decays exponentially:

$$\psi_i(z) = \begin{cases} Bu_{-k}e^{-ikz} + Cu_k e^{ikz}, & \text{for} \quad z \leq 0, i \neq 0 \\ D\exp\left[-\sqrt{\frac{2mz}{\hbar^2}(V_0 - E)}\right], & \text{for} \quad z > 0, i = 0, E < V_0 \end{cases} \tag{3.16}$$

To get a complete continuous solution, the matching conditions must be fulfilled. Hence, $\psi_i(z)$ and the first derivative have to be continuous at $z = 0$:

$$\psi_0(z = 0) = \Psi_i(z = 0) \quad \text{and} \quad \left.\frac{\mathrm{d}\psi_0}{\mathrm{d}z}\right|_{z=0} = \left.\frac{\mathrm{d}\psi_i}{\mathrm{d}z}\right|_{z=0}. \tag{3.17}$$

An additional surface solution will become possible if complex wave vectors are allowed:

$$\psi_i(z) = \begin{cases} Fe^{qz}\left\{\exp\left[\mathrm{i}\left(\frac{\pi}{a}z \pm \delta\right)\right] \mp \exp\left[-\mathrm{i}\left(\frac{\pi}{a}z \pm \delta\right)\right]\right\} e^{\mp \mathrm{i}\delta}, & \text{for} \quad z \leq 0, i \neq 0 \\ D\exp\left[-\sqrt{\frac{2mz}{\hbar^2}(V_0 - E)}\right], & \text{for} \quad z > 0, i = 0, E < V_0 \end{cases} \tag{3.18}$$

For the second solution, the matching conditions must also be fulfilled. For this matching, there are exactly two free parameters: the energy eigenvalue E and the ratio D/F of the wave function amplitudes. The wave function of the resulting electronic surface state is shown qualitatively in Fig. 3.4 b).

The results for surface states of a monatomic linear chain can partially be generalized to the case of a three-dimensional crystal. But for realistic calculations of the electronic structure of surfaces of a three-dimensional crystal, using structural models is necessary.

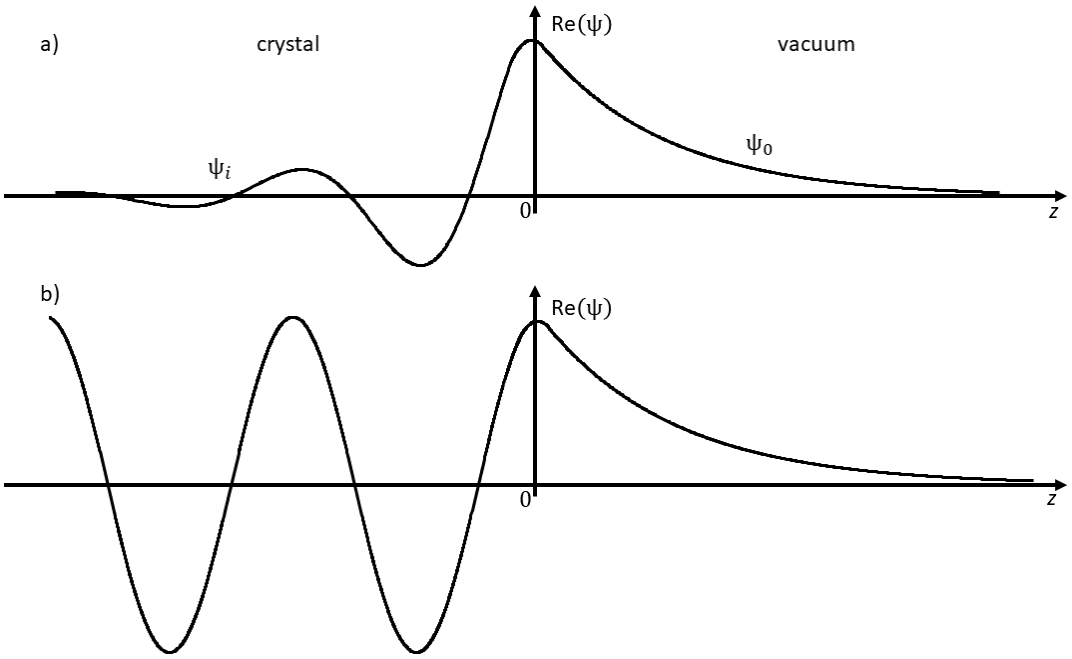

Fig. 3.4. a) a surface-state wave function localized at the surface is shown. This is the surface state, according to the Shockley model. The surface resonance in b) is the real part of the solution, the one-electron wave function: a standing Bloch wave, matched to an exponentially decaying tail in the vacuum.

3.6.3. Tamm-States

Surface states calculated by the tight-binding model are called Tamm states [104]. In contrast to the nearly free electron model used to describe the Shockley states, these states are suitable to describe transition metals and wide gap semiconductors. Since the atoms of the uppermost surface layer lack their binding partners on one side, their atom orbitals have less overlap with the orbitals of neighboring atoms. The splitting and shifting of the energy levels of the surface are therefore smaller.

A perturbed Kronig-Penney potential in combination with the one-dimensional time-independent Dirac equation is the simplest model for a solution [105]. The one-dimensional model is based on a series of potential wells, each separated by a barrier [106]. The wells represent the area near the atomic nuclei, where the electrons are attracted by the nuclear charge. In the areas in between the barriers, the charge of the nuclei is shielded by the electrons. Additionally, an infinite lattice is supposed, and according to the Bloch theorem, spatially periodic solutions of the Schrödinger equation are obtained. The solutions are functions with a strongly localized character, split from flat bulk d bands by the surface perturbation. In the Shockley model, however, the wave functions are sp-like, i.e., plane waves parallel to the surface associated with a hybridization gap [107].

3.6.4. Friedel Oscillations

Friedel oscillations are caused by localized disturbances due to defects in a system and therefore require quasiparticle or scattering treatment [32]. They represent a characteristic exponential decay of the fermion density near the defect. The electrons, moving freely through the solid, are scattered at foreign atoms by their deviating potential. This scattering can also occur by measuring surface states with the STM, originating from the elastic scattering on defects. For planar waves, the resulting Friedel-oscillations, appearing as circular waves, create a wave vector which corresponds to the scattering vector. The model assumes a homogeneous electron density in an undisturbed region, as for plane waves, but can be generalized to determine the scattering vector for Tamm states.

3.7. Bychkov–Rashba Effect

The Bychkov–Rashba effect after Emmanuil Iossifowitsch Raschba and Yurii A. Bychkov is the coupling of the electron spin to the orbital motion of an electron [13, 108]. Hence, it is an effect of spin-orbit coupling. Classically, an electric field is the direction of the electron motion, i.e. perpendicular to the surface, and causes a precession motion that changes the spin orientation. This only occurs when there is an inversion asymmetry in the system structure, for example, at surfaces. The SOC can quantum-mechanically be described, using a special expansion term of the Dirac equation [109]. It describes the properties and behavior of a fermion with spin 1/2:

$$\mathcal{H} = \mathcal{H}_0 + \mathcal{H}_\mathrm{B} + \mathcal{H}_\mathrm{SOC} = \frac{\vec{p}^2}{2m} + V(\vec{r}) - \frac{Q}{m}\vec{B}_{ext}\cdot\vec{S} - \frac{Q}{2m^2c^2}\left(\vec{E}\times\vec{p}\right)\cdot\vec{S}, \tag{3.19}$$

with the particle moving in a potential $\mathcal{H}_0$, the coupling of spin and external magnetic field $\mathcal{H}_\mathrm{B}$ and the spin-orbit coupling term $\mathcal{H}_\mathrm{SOC}$. Assuming a two-dimensional electron gas without external magnetic field and writing the electric field as $-Q\vec{E} = \vec{\nabla}V(\vec{r})$ one obtains:

$$\mathcal{H} = \mathcal{H}_0 + \mathcal{H}_\mathrm{SOC} = \frac{\vec{p_{||}}^2}{2m} + \gamma\left(\vec{\nabla}V(\vec{r})\times\vec{p_{||}}\right)\cdot\vec{S} \quad \text{with} \quad \gamma = \frac{1}{2m^2c^2}. \tag{3.20}$$

Now solving the eigenvalue equation for $z = 0$ results in the following solution with the help of a quadratic addition:

$$E_\mathrm{B} = \frac{\hbar^2}{2m}\left(k_{||} \pm \frac{m}{\hbar^2}\xi\right)^2 - \frac{m}{2\hbar^2}\xi^2 \quad \text{with} \quad \xi = \gamma\frac{\partial V(z)}{\partial z}|_{z=0}\frac{\hbar^2}{2}. \tag{3.21}$$

When the energy is plotted versus the wavenumber component k, the equation describes a parabola that is shifted to the left or right on the abscissa and downwards on the ordinate. A graphical representation of the dispersion relation is shown in Fig. 3.5 a). Looking at a cross section, one gets two circles like in Fig. 3.5 b). Here, it can be seen that the spin is always perpendicular to k and parallel to the surface. This relation is isotropic, i.e. independent of the selected k-direction. Thus, for the energy dispersions along any two-dimensional impulses on the surface the dispersion is the same. In Figure 3.5 c) the plot is shown three-dimensionally. The graph shows the two conical dispersions, plotted against the energy.

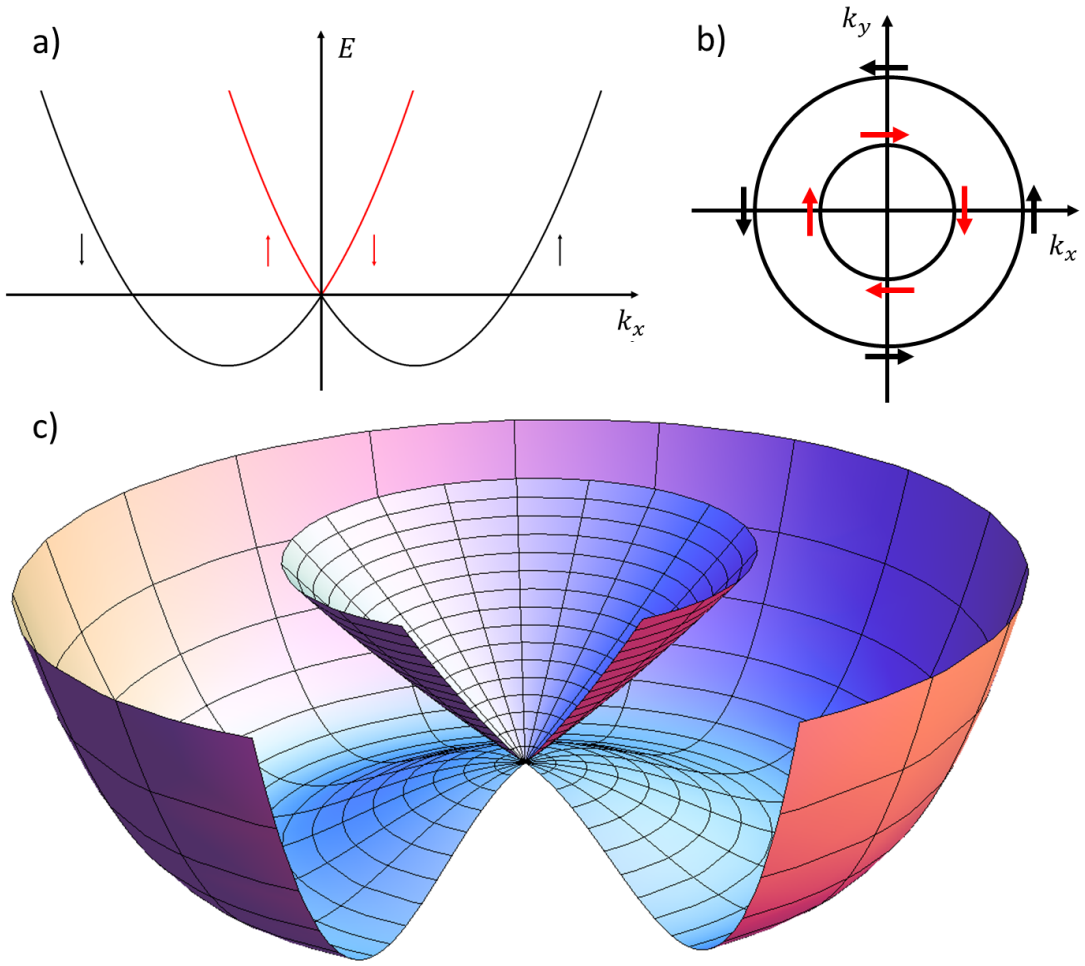

Fig. 3.5. The effect of the spin-orbit coupling at the surface is in the simplest case a dispersion relation represented in the splitting of a free electron-like parabola into two parabolas, shown in a). The inner branches (red) correspond to the solution of the downspin, the outer branches with the up-spin to the solution in black. In b), the spin polarization is shown in one view. The spin is always perpendicular to k and parallel to the surface. c) Since the relation is isotropic with respect to k_x and k_y, the parabolas form three-dimensional cones as rotational bodies around the origin.

The Rashba effect is calculated for various metallic surfaces such as Au, Ag, Pt, Cu, Sb, Lu, and Re, but could not be experimentally confirmed on all of them until

now [110, 109]. The experimental proof of the Rashba effect, due to the comparatively small effects on the band structure, could only be provided after its discovery. The Rashba effect can be observed on surfaces of a variety of metallic crystals and alloys and is relevant in many research areas such as topological insulators, Majorana fermions or cold-atom systems [111, 112].

For the experimental proof of the Rashba effect, it must be strongly pronounced in order to be able to observe the splitting of the parabolas. The Rashba effect is enhanced for materials comprising elements with a high nuclear charge number Z. Although the Rashba effect exists for bulk states, too, it is stronger for surface states residing in the potential gradient at an interface [13]. Since the Rashba effect is comparatively weak and the two Rashba branches are difficult to distinguish, there are only a few methods to measure it. With ARPES, the energy dispersion curves can be scanned, whereby the momentum and energy of the photoemitted electrons are measured. From the difference of the kinetic energy of the electrons, the band splitting and the binding energy can be calculated. By measuring the angle, the corresponding momentum, or wave vector can be determined.

All conditions are given for electrons at the Au(111) surface as calculations of band structures show [19]. With the help of ARPES, the Rashba effect on the surface of Au could be proven unambiguously for the first time in 1996 by Lashell et al. [30]. Later it was possible to achieve excellent agreement between experimental data and the results of theoretical calculations [113]. The measurements were supplemented by spin-resolved measurements, which could prove the orientation of the spin [114].

The Rashba effect could also be experimentally investigated in other systems, for example, on $BiCu_2$/Cu(111) with a combined study of ARPES and STM [18]. Another interesting example, where Rashba splitting could be detected, is Bi/Ag(111)$R30°$, because it is a system with several surface bands where the splitting occurs in the different bands [17, 16]. Furthermore, surface resonance can exhibit a Rashba splitting too, as shown, for example, by a system of one to four monolayers Ag on Pt(111) [115]. The split surface bands are also clearly distinguishable in Re so that the Rashba effect on the pristine Re surface could be demonstrated by ARPES measurements [26].

The Rashba effect is often experimentally proven with combined studies of STM and ARPES. However, spin splitting itself can only be measured with ARPES. The STM can map a scattering vector, but because the DOS oscillations are generated by a linear combination of the Rashba split wave vectors, the presence of the Rashba effect itself cannot be verified by FT of STS measurements in the first place [19, 20].

4. Design and Methodology

The physical principles of the scanning tunneling microscopy were explained in Chapter 2. This section deals with the experimental equipment, setup, and techniques used in this work. In addition, the performance of the measurements and the associated problems are discussed.

All measurements were performed using an UHV low-temperature (LT) STM (Scienta Omicron). Sample preparation, as well as the measurements, were operated under UHV conditions. The pressure during the measurements varied between $P = 7 \cdot 10^{-10}$ mbar and $P = 4 \cdot 10^{-11}$ mbar, where the low pressure only could be achieved at low temperatures.

Section 4.1 introduces the setup of the microscope with the different chambers and options. In the following (Sec. 4.2), it is dealt with the UHV conditions of the microscope. Section 4.3 introduces the measuring electronics of the system. The sensitivity of the STM is an important factor during the measurements. This will be discussed in detail in Paragraph 4.4. Section 4.5 deals with the heart of the microscope, the tunneling tip, and especially with tip preparation. Finally, the sample preparation is presented and a short explanation of the measurement is given (Sec. 4.6).

4.1. The Scanning Tunneling Microscope

The setup used for the measurements consists of a measuring chamber with the STM, a preparation chamber, a cleaving chamber, and a load lock. As shown in Figure 4.1, the chambers are connected by tubes, making an internal sample transfer in the vacuum possible. Four transfer rods are installed in the UHV system for sample transfer. A long transfer rod is used to transfer the sample between the chambers. In each chamber, a transfer rod is mounted to move the sample to different locations.

Measuring Chamber

The measuring chamber is the most important part of the system, where the microscope with tip and electronics is located. In Fig. 4.2, the measuring head can be seen through the window in the cooling shield. Centrally above the microscope is the helium tank with a volume of about 3.5 liters. The tank is directly connected to the inner cooling shield, which allows the sample to be completely shielded during the measurement. A cylindrical nitrogen tank is placed around the inner He-tank and connected to the outer cooling shield. Both shields have four windows to allow optical and mechanical access to the sample.

During the measurement, the shields can be closed for a complete shielding to keep the microscope as cold as possible for a long time.

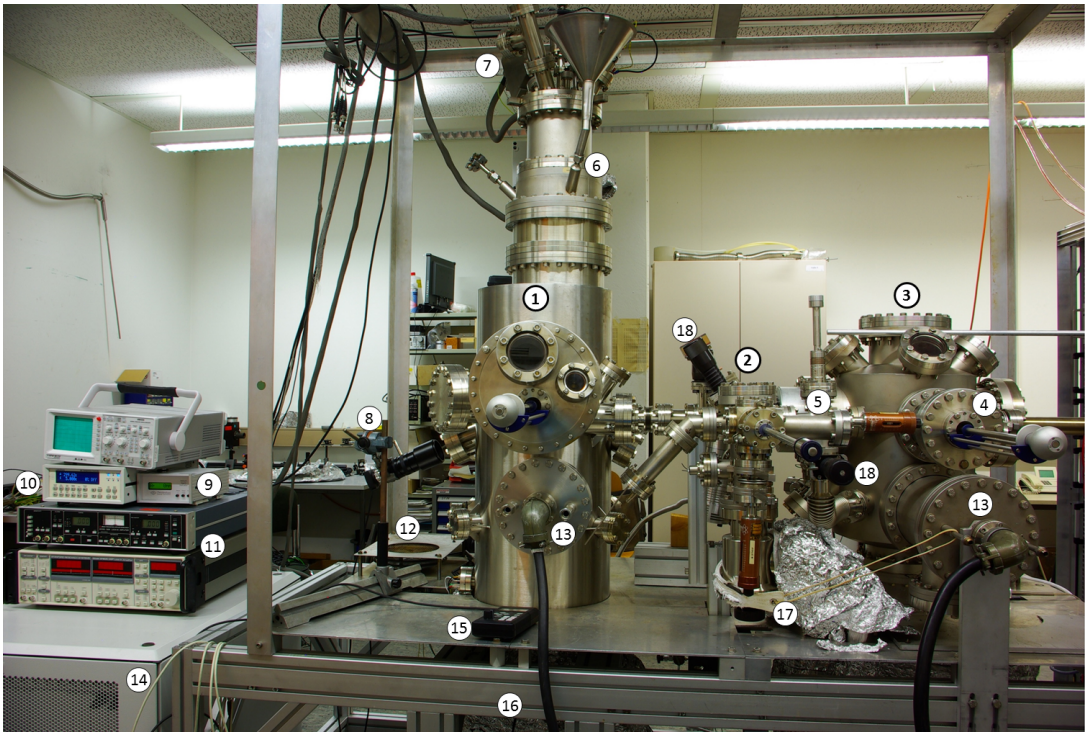

Fig. 4.1. A picture of the STM used for the measurements. The most important components are briefly labeled below: (1) Measuring chamber of the microscope containing measuring head and a sample carousel. (2) Cutting chamber with a device for cutting organic crystals. This chamber can also be used as a lock. (3) Preparation chamber with metal evaporators, the heating stage for flashing, mass spectrometer, and LEED. (4) One of the wobble sticks for sample transfer. (5) Cutting pliers for sample preparation. (6) Filler neck for the outer thermal shield, above it the funnel for filling with liquid nitrogen. (7) The electronic connectors for the sample heating, the temperature sensor, and the tunneling current signal are located at the top of the microscope. The preamplifier and voltage converter for the tunneling current signal are also located there. (8) Camera for approach and transfer. (9) Measuring device for the helium filling level. (10) Temperature measuring device for the vacuum chamber. (11) Lock-in amplifier. (12) One of the heaters for baking out the system. (13) The power inputs for the TSP pumps. (14) “Matrix“ measurement electronics from the company “Scienta Omicron“. (15) Control element for approach and adjustment of the tip. (16) The getter pumps are wrapped in aluminum foil underneath the chamber. (17) The connection of the turbo-molecular pump, wrapped in aluminum foil, with a valve next to it. The cutting chamber can be separated from the rest of the system by two valves (18) and thus separately baked out.

The system is capable of operating at three different temperatures: room temperature, nitrogen temperature, and helium temperature[1]. In order to reduce mechanical noise originating from the acoustic coupling or building vibrations, the microscope is suspended from springs hence it can swing freely. This also minimizes the contact surface to the rest of the system and thus the heat transfer. In addition, the microscope is damped by an eddy current retarder in the lower part of the chamber. For cooling the microscope can be brought into thermal contact with the He-tank via a lever so that it cools down as quickly as possible. A setting for sample transfer is also possible. Here, the microscope is brought into mechanical contact for stabilization to enable vibration-free sample transfer.

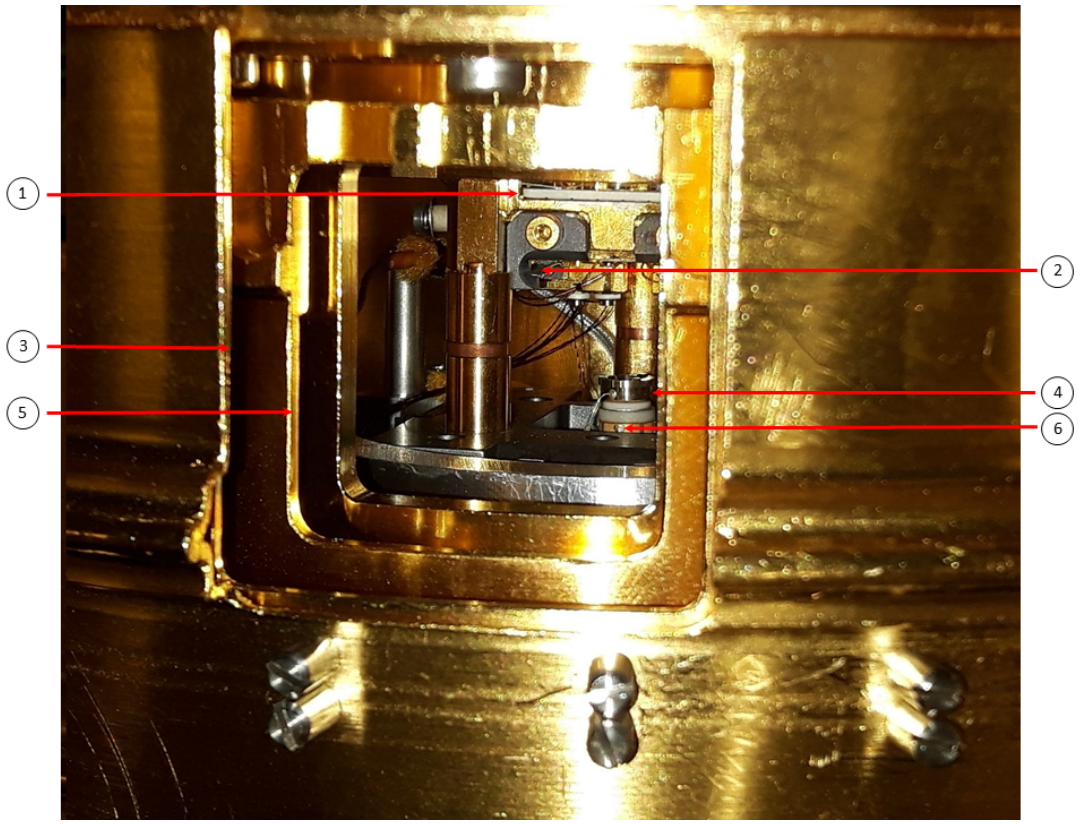

Fig. 4.2. The measuring head, seen through the two cooling shields; the most important components are marked with numbers: (1) The sample heating to regulate the temperature in the range between approx. 4.6 K and 30 K. (2) The sample guide rail is precisely adapted to the sample holders. (3) The outer cooling shield is connected to the nitrogen tank. (4) Inside the tip-disk is a magnet, thus the tip has good contact but is also easy to change. (5) The inner cooling shield is attached to the helium tank. (6) The scanner with a piezo tube is connected by five electrodes.

A sample carousel is mounted in the front part of the measuring chamber. A maximum of six tips or samples can be stored. For sample transfer, a wobble-stick is attached to the front of the chamber. With the help of these pliers, the sample

[1] room temperature corresponds to about $T_R = 291\,\mathrm{K}$, nitrogen temperature is about $T_S = 77.5\,\mathrm{K}$ and helium temperature reaches about $T_H = 4.6\,\mathrm{K}$

can be moved and rotated freely in a conical action area. The sample can thus be taken from the transfer rod and guided into the holder of the STM or deposited in the sample carousel.

Preparation Chamber with LEED

The preparation chamber is on the right side of the system [Fig. 4.1 (3)]. It contains a movable heating stage for sample and tip preparation. A high voltage can be applied to the sample in addition to a direct voltage. For heating up, the sample electrons can be accelerated from the heating filament to the sample. With this method, temperatures up to $T = 2500\,\mathrm{K}$ can be reached. For further sample preparation, a dosing valve offers to let oxygen in the chamber to create a light oxygen atmosphere.

In addition, a metal evaporator with six BeO crucibles for the production of ultra-thin layers by molecular beam epitaxy is placed in the chamber. Above this, a quartz monitor is mounted, which is used to determine the amount of evaporated metal. Additionally, a shutter is installed for closing the crucibles to immediately interrupt the evaporation process. Furthermore, the preparation chamber is equipped with a LEED system for the investigation of periodic surfaces and thin films. Just like in the measuring chamber, a wobble stick for sample transfer is installed here as well.

The preparation chamber also contains a mass spectrometer for the analysis of the residual gas composition. However, this does not include an electron multiplier and therefore has a maximum resolving power of about $p = 10^{-9}\,\mathrm{mbar}$. It is used for leak testing after re-closing the vacuum chamber but cannot detect hair leaks in the system. For the leak test, helium is blown against the flanges, and the residual gas composition is measured. If a pressure increase occurs at a mass of $M = 4\,\mathrm{u}$, the helium atoms entered the system, and the leak is detected.

Cleaving Chamber, Loadlock

In the middle of the system, there is a third chamber used for different applications. Since the cleaving chamber can be separated from the rest of the system with two valves, this chamber was used during the experiments to insert new samples and tips into the UHV system. The chamber can be pumped and baked out separately from the rest of the system resulting in considerable time-saving. In addition, this chamber is equipped with pliers for cleaning and cutting organic crystals under UHV conditions to obtain a surface that is as clean and flat as possible.

4.2. Operating in UHV

It is advisable to carry out the measurements with a STM under UHV conditions at a pressure of approximately $p = 10^{-10}$ mbar. Otherwise, adsorbates can deposit and contaminate the sample or the tip and change the system while measuring. Therefore, the whole system is under UHV during measurement, transfer, and preparation. To maintain the low pressure, the system has to fulfill several requirements regarding material choices, leak rates, and pumping capacity.

The vacuum of the system is obtained by two turbo-molecular pumps. Without any further precautions, these pumps reach a minimum pressure of about $p = 10^{-8}$ mbar. Turbo-molecular pumps work similarly to a turbine with a frequency of $f \sim 1.5$ kHz and several rotors. However, due to the vibration generated by the rotating parts of the pump, they cannot be operated during STM measurements.

If the system is filled with air, water always will settle on the chamber walls. In order to prevent a constant diffusion of the water molecules and the associated contamination of the vacuum after closing the system, it must be baked out. For this purpose, the complete UHV system is packed into an insulating tent and brought to a temperature between $T = 120\,°\text{C}$ and $T = 150\,°\text{C}$ for several days using fan heaters and heating tapes. Meanwhile, the cooled turbo-molecular pumps are used to pump the vacuum. After baking, they are separated from the system by valves and are no longer needed.

During the measurements, two ion getter pumps, which are mounted below the chambers, are operated to maintain the vacuum. The ion getter pumps ionize residual particles by electron collisions and accelerate them by an electric field onto a titanium surface. There the particles are chemically bound or implanted. When the ions hit the surface, further Ti atoms are released, which can bury adsorbed residual gas particles. Thus, the pump has no gas outlet opening but adsorbs the pumped atoms at the inner surfaces of the pump or “buries“ them in the metal. Because there are no moving parts the pump is vibration-free.

Two titanium sublimation pumps are also integrated in the system for rapid pressure improvement. These are special UHV pumps based on the gettering capability of freshly evaporated titanium: the titanium is evaporated onto a high purity, coolable adsorbent surface where it traps the randomly impinging gas atoms by chemisorption. Gases such as oxygen, nitrogen, or carbon dioxide can thus be chemically bound to the titanium.

Moving the sample in a vacuum is rather complex and therefore requires some practice and skill. In total, the sample can only be moved indirectly with the transfer rods described in Section 4.1. However, there is only a little space in the chambers and the small sample holders have to be positioned relatively accurately. Otherwise, the sample may be lost in the chambers. In this case, the system must be opened since the wobble sticks also have a very limited range of action and if the sample is lost, access to it will be usually lost, too. This results in a considerable loss of time due to the complex UHV conditions. A further difficulty is the severely restricted visibility.

For the approach between tip and sample as well as the sample exchange, two additional cameras from different angles are used to enlarge and improve the view of the process.

The cameras are equipped with telescope optics to magnify the image. However, there is always uncertainty during transferring and approaching.

Before measuring, the tip must be brought very close to the sample. For this purpose, a rough approximation is carried out first: the tip is moved manually close to the sample surface by a piezo motor until it almost touches its mirror image on the sample. Then, the automatic approach mode of the control software is used. This moves the tip step by step to the sample and measures the tunneling current after each step. If the electronics find a tunneling signal, the tip is in the measurement position. Afterward, the tip can be approached manually some more steps in order to center the deflection of the scanner. This avoids collisions and the tip running out of the measuring range during the measurements.

4.3. Electronics

In the topography area, the tunneling current is adjustable in two modes between $I = 0.0003\,\mathrm{nA}$ and $I = 333\,\mathrm{nA}$. It follows from Section 2.2 that the distance between sample and tip decreases logarithmically with increasing tunneling current. The tunneling voltage can also be varied in two ranges between $U = -10\,\mathrm{V}$ and $U = 10\,\mathrm{V}$, where a larger voltage at constant tunneling current causes a linearly larger distance. At higher voltages, the tip becomes more unstable overall. This increases the probability that the tip will drop or change parts and making the measurement useless.

Another possibility to optimize the measurement is the loop gain. It determines how fast the electronics readjusts the tip-sample distance, i.e. how sensitive the electronics react. If it is set too low, the images are blurred or only roughly reproduced and step edges become indistinct. If the loop gain is set too high, abrupt changes in height will result in disturbing overshoots or the control loop will oscillate completely. An optimal adjustment of the loop gain depends on the measuring speed and the roughness of the sample. The aim is to use the loop gain to bring the for- and backward image as close as possible. In general, the loop gain is adjustable between $0.01\,\%$ and $100\,\%$.

Although the surface structure theoretically can be resolved more precisely if the distance between the sample and the tip decreases, it cannot be said that the image improves overall. A large tunneling voltage can even partially tear sample structures apart and thus destroy the sample locally. Often the sharpness of the image depends on small details. To get a better resolution, it is usually useful to reduce the image section instead of varying the tunneling parameters.

For spectroscopy mode, voltage start and endpoints can be selected in the range mentioned above. The step size, i.e. the number of recorded points as well as their temporal distance, are free parameters. The software also offers the possibility to stabilize the tip with parameters, freely selectable in the described ranges to determine the stabilization times exactly. Often each parameter must be adjusted to obtain a meaningful measurement. The measuring parameters have to be also adjusted with the lock-in amplifier to get good results.

4.4. Sensitivity of STM

In Section 4.1 the damping of the microscope is explained. Since the system is located on the first floor, it is important to minimize vibrations. To do this, it is essential that the STM section has no contact with the rest of the system, except for the springs for suspension and the wires of the measuring head. In the system itself, various electrical interferences between $f = 6\,\mathrm{Hz}$ and $f = 3000\,\mathrm{Hz}$ are coupled in, which have an immediate and strong effect on the measurement in case of contact.

The vibrations can be analyzed particularly well by continuously scanning a point on the sample with the measuring software: since the topographical information is hidden in this way, pure background noise is visible. The STM can be aligned via four height-adjustable feet. The adjustment aims to achieve a state in which the measuring head can freely oscillate in any direction. The system also has to get adjusted differently for the different temperature levels in order to minimize disturbances. The system is extremely sensitive, so opening the laboratory door, walking through the laboratory, or loud noises are easily noticeable and often disturbing the measurements. Therefore, an active damping system was additionally installed under the microscope, reducing the background noise by a factor of about ten.

4.5. Tunneling Tip

The tunneling tip is crucial for a good measurement. At the same time, it is one of the most sensitive and susceptible components of the microscope. Tips are usually made from metals such as tungsten by etching processes but can also be produced by tearing off a platinum-iridium wire. Etching a tip takes only a few minutes. It is important to switch off the voltage immediately after finishing the tip. Afterward, the tip has to be removed from the lye bath and cleaned form the lye to become not blunt again. Mostly NaOH or KOH are used as lye, but better results can be achieved with KOH [116]. In general, the tip should be as sharp as possible, ideally, it has exactly one atom closest to the sample. The largest part of the tunneling current flows through this atom due to the exponential relationship between distance and tunneling current. In general, industrially etched tungsten tips are used for the measurements in order to obtain results that are as comparable and reproducible as possible.

Tungsten is a reactive metal. When it comes into contact with the oxygen in the air, it forms an oxide layer that protects the metal against further corrosion. This oxide layer forms at the tip apex and disturbs the tunneling current. There are two ways to remove oxide layers from the tip:

Flashing

Flashing is a technique in which the tip is extremely heated for a few seconds. The heating stage described in Section 4.1 is used for this; the tip can be placed in a special holder just above the filament. The filament operated by a DC voltage emits electrons which are accelerated towards the tip by a high voltage of

$V_H = 830\,\mathrm{V}$ applied to the tip until the emission-current increases to $I = 250\,\mathrm{mA}$. The accelerated electrons are decelerated by the tip and release their energy. From this, the tip obtains the necessary thermal energy.

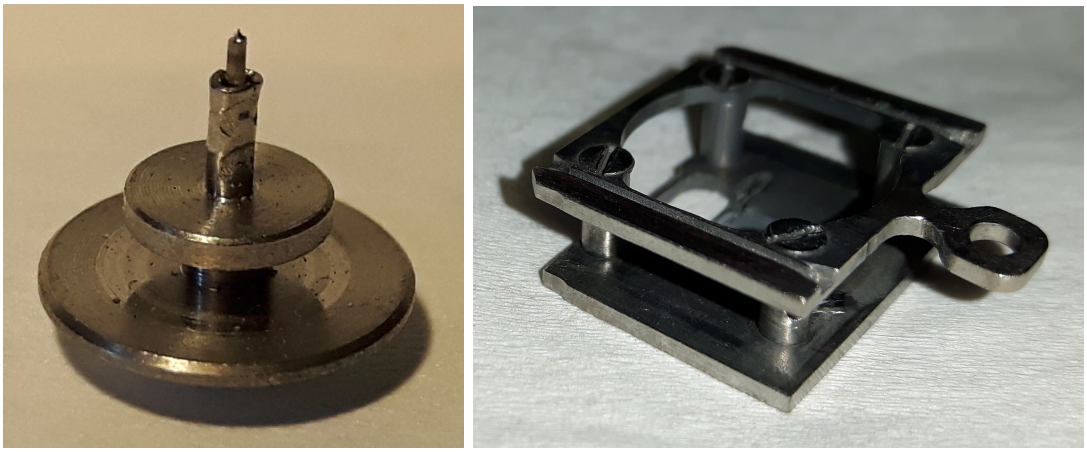

(a) Tip (b) Tip Holder

Fig. 4.3. a) A industrially manufactured tunneling tip with tip base. The base is made of stainless steel, the tip of tungsten. b) Shown is the special tip holder for flashing the tip. The holder is inserted into the sample guiding grooves in the microscope to insert the tip manually, leaving it only loosely in the holder. The flash tip holder is designed for the tip to be as close as possible to the filament.

With this method, the tips, as well as tungsten, molybdenum, and rhenium crystal samples, can be cleaned from most undesired particles by complete evaporation at temperatures of approx. $T = 2200\,^{\circ}\mathrm{C}$. To flash the tip, it must be placed in a special molybdenum flash tip holder [Figure 4.3 b)]. The temperatures reached during the flashing of the tip cannot be measured, because the heated point is very small. It is expected that the temperatures will be much higher than with flat crystal samples since all electrons are much more strongly focused on one point. Therefore, tips are usually flashed only $t_T = 5\,\mathrm{s}$, samples for about $t_S = 10\,\mathrm{s}$. Thus, it is necessary for flashing that the sample holder and sample or tip holder and tip are extremely thermally stable. One of the used tips is shown in Fig. 4.3 a).

Almost all impurities can be removed by flashing [117]. The exceptions are carbon and carbon compounds due to the extremely high melting points. By admitting a small amount of oxygen into the preparation chamber, an oxygen atmosphere is obtained at a pressure of $p = 10^{-7}\,\mathrm{mbar}$. If the sample is heated to about $T = 1500\,\mathrm{K}$ for ten minutes, the carbon will react to CO or CO_2, hence it desorbs after flashing again and can be pumped off.

Pulsing

If the tip does not provide a useful image or is contaminated, it will be treated by voltage pulses. This can randomly make it better or worse. However, repeating the process often enough generates a better tip. The pulses cause small parts of the tip to fall off again and again. In this way, an oxide layer or other impurities can be removed. To get a suitable tip, often many repetitions are necessary, and it depends on the other tunneling parameters whether and how significantly the tip changes. The software offers the possibility to adjust pulse length and height directly to achieve a good pulsing result. The dropping tungsten pieces can contaminate the sample locally.

In general, a new tip has to be flashed once to be usable. For the tip preparation, a cleaned Re(0001) sample is used. The requirements for the tip are on the one hand spectroscopic stability and on the other hand a good topographic image quality. The tip is prepared on the crystal until it met the requirements. For a good recording quality, it is crucial that there is exactly one atom at the top of the tip: if several atoms are at a very similar height, the image will be slightly shifted or superimposed several times. This effect is called double-tip or if there are more than two tip atoms, multiple-tip. Also, in this case, the tip has to be pulsed to eliminate secondary tips until the tip is taking a clear image.

Often a tip that produces good topographic images does not necessarily offer useful spectroscopic information and vice versa. An unstable tip, for example, can record high-quality images, but falls apart during spectroscopic imaging, because much larger forces prevail there. When neither flashing nor pulsing have a positive effect and do not improve the tip, the software offers another possibility: the tip can be rammed into the tungsten sample in a targeted and controlled way to wipe off the particles. However, this makes the tip blunter and this procedure has rarely been used as a last resort.

4.6. Sample Preparation and Experimental Procedure

The Re(0001) single crystal was prepared by alternate flashing at $T \approx 1800\,\mathrm{K}$ for around $t = 10\,\mathrm{s}$ and annealing in an oxygen atmosphere of $3 \cdot 10^{-8}\,\mathrm{mbar}$ at $T \approx 1400\,\mathrm{K}$ for ten minutes, resulting in a nearly clean surface [64]. For this work, two different Re(0001) crystals are used. However, no significant differences in the measurement results between the two samples could be found, but the much older crystal contained more defective and foreign atoms, so it only was used at the beginning of the experiments. The second sample, fixed to a standard sample holder with two plates is shown in Fig. 4.4.

The step decorations are grown by deposing one-tenth of a monolayer of Ni or Au via molecular beam epitaxy onto the cleaned Re(0001) surface and annealing at $T \approx 750\,\mathrm{K}$ for $t = 300\,\mathrm{s}$. Thus, narrow stripes of the adsorbed metals form at the step edges of Re. The sample is then transferred *insitu* into the STM. Topographic STM images were recorded in the constant-current mode (Sec. 2.5.2) at a stabilizing current I between $0.1\,\mathrm{nA}$ and $2\,\mathrm{nA}$ with the bias voltage V applied to the tip.

The STM images shown here are recorded with a fast vertical scan direction and a slow horizontal scan direction from left to right. Topographic data is recorded in the forward and backward scan direction resulting in two images recorded almost simultaneously. Each image comprises 512×512 pixels. After measuring the last line of an image, the tip moves straight back to the starting point with constant speed and starts scanning the next image or scans the sample area in the opposite direction[2]. The scanning speed for an image, requiring an acquisition time of 35 min, is ca. 100 nm/s.

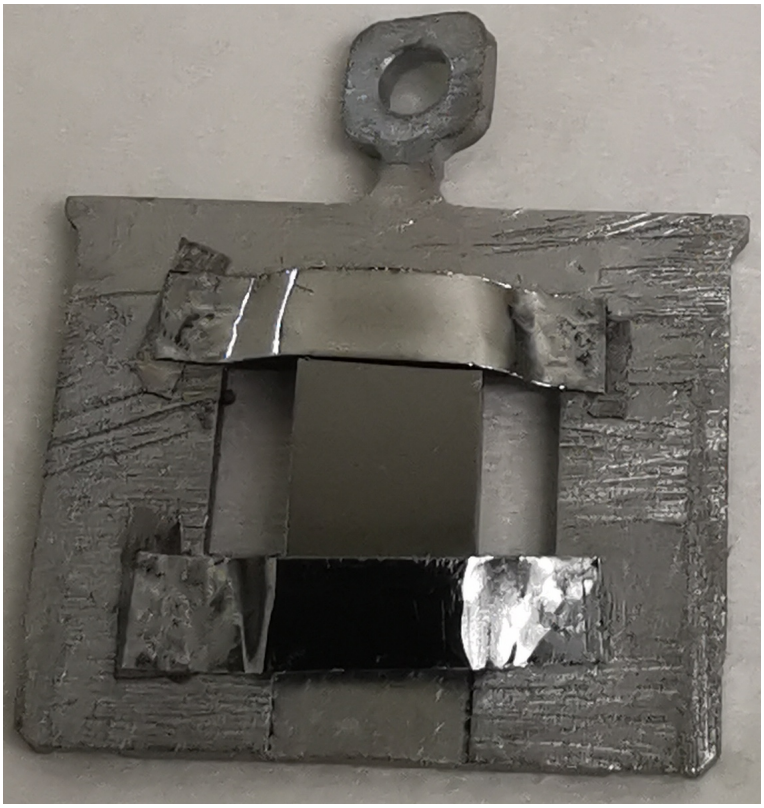

Fig. 4.4. The sample is fixed indirectly to the sample holder, made of Mo using two Mo plates. With the sample holder the sample can be transferred between the different chambers inside the STM for preparation. The Re(0001) single crystal in the center is thus protected from mechanical damage.

By measuring the differential conductance dI/dV as a function of the sample bias V with lock-in technique [$V_{\mathrm{mod}} = 6\,\mathrm{mV}$ (rms), $f = 786\,\mathrm{Hz}$] dI/dV maps are obtained. For the dI/dV maps, an especially stable tip is needed because of measuring times up to 22 hours. Most images are taken at helium temperature at $T = 4.6\,\mathrm{K}$. For the mobility measurements of Ni, there are also chosen additional temperatures. By opening the thermal shields, a nearly stable temperature at $T = 13\,\mathrm{K}$ is accomplished. Additionally, the mobility of Ni atoms is measured at nitrogen and room temperature. For image processing, WSXM is used [118].

[2] (indicated on the corresponding measurements)

5. Growth of Ni and Au on Re(0001)

While the growth of ferromagnetic 3d transition metals on high-melting single crystal surfaces of 5d transition metals has been an active research field since the seminal work of E. Bauer [74], only a few studies focused on hcp surfaces [64, 65, 66, 73, 79]. The growth of Ni on Re(0001) as studied by atomic emission spectroscopy (AES) and LEED found that at 325 K Ni grows in the quasi Frank-van der Merwe mode at least up to 4 atomic layers. The first monolayer grows pseudomorphic, i.e. in registry with the substrate atoms. Subsequent atomic layers up to about 10 ML form an (10×10) coincidence lattice, which can be interpreted by a misfit dislocation network and double scattering [79]. STM studies confirmed the results obtained by electron diffraction [66]. Annealing above 600 K leads to coalescence of islands [74, 73]. The fact that the growth of Ni on Ru(0001) differs from the growth of Ni on Re(0001) even though the lattice constants are quite similar, demonstrates how sensitive the growth characteristics can depend on subtle differences of lattice parameters. In the following, we present LEED results for Ni and Au on Re(0001) to confirm previously reported results (Sec. 5.1). The samples are then analyzed using STM, and the corresponding results are shown and discussed in Section 5.2.

5.1. LEED Results

LEED measurements were performed to analyze the structure of adsorbed Au and Ni films. Figure 5.1 a) shows the LEED pattern of the cleaned Re crystal. The six first-order symmetric main reflexes [Fig. 5.1 a) 1-6] form a regular hexagon and reflect the hexagonal structure of the hcp lattice in the (0001)-direction. In the picture, the reflexes of the second [7-8] and third [9-10] order can be seen. The LEED pattern of the Re(0001) sample covered with 0.95 ML Au after annealing is shown in Fig. 5.1 b). The pattern shows a similar hexagonal pattern of reflexes.

In Figure 5.1 c) a LEED pattern of Re covered with 0.5 ML Ni is depicted. The higher electron energy of 120 eV reduces the diffraction angle of the scattered electrons, which increases the number of higher-order reflexes that can be observed on the screen. Therefore, in addition to the first and second-order reflexes, which occur at the same spot positions as in the pattern of clean Re(0001), some third-order reflexes can also be observed. So it can be concluded that the growth of the first monolayer of Ni and Au on Re(0001) is pseudomorphic.

Figure 5.1 d) shows a LEED pattern of 0.66 ML Ni on Re(0001) before annealing. At room temperature, Ni grows in islands of different heights as shown by STM images in Figs. 5.4 a) and c). The LEED pattern shows additional superstructure reflexes around the first order reflexes. These are partly weakly pronounced, as it is not a complete coverage of two monolayers, but the important features can be recognized.

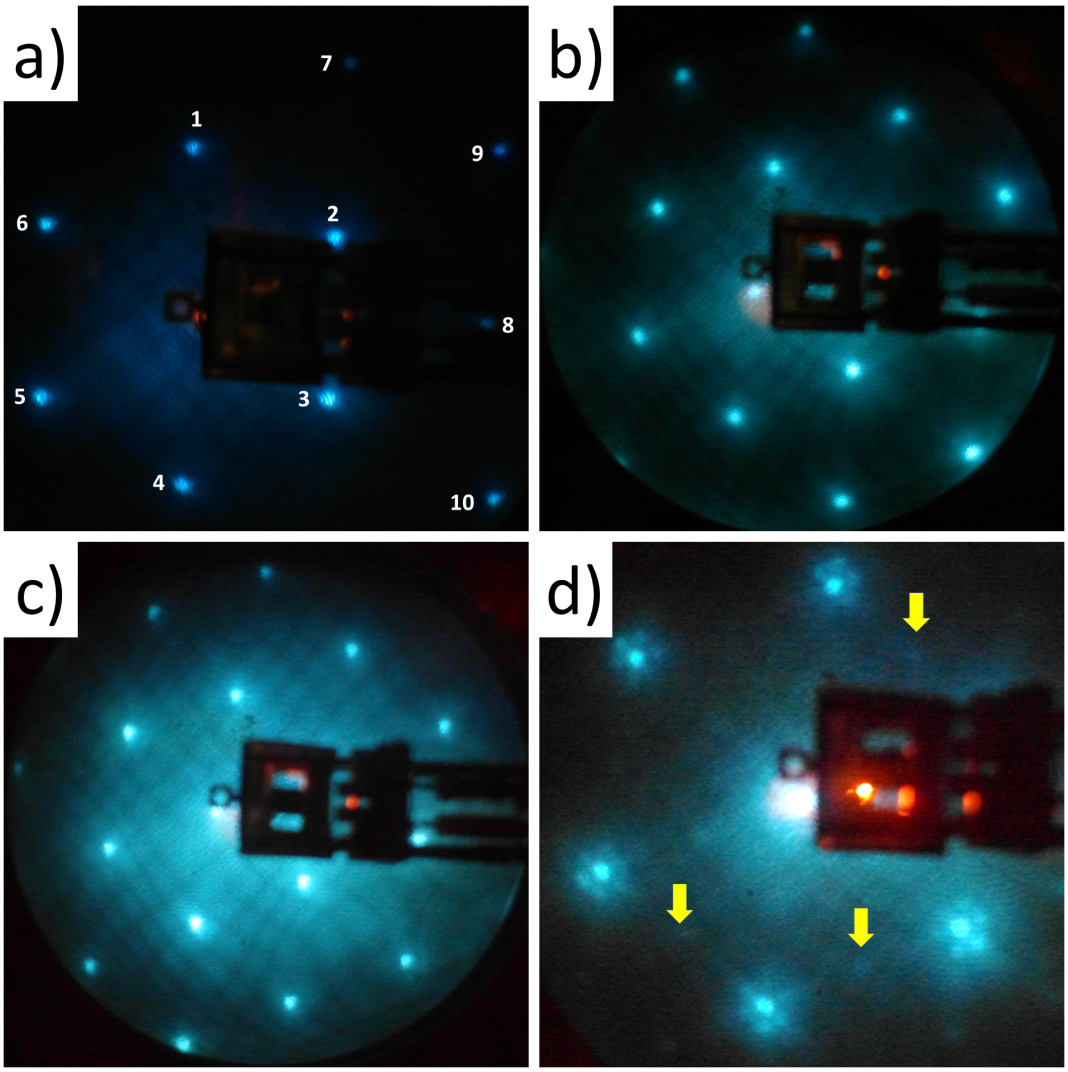

Fig. 5.1. a) LEED pattern of a cleaned Re(0001) single crystal surface (electron energy 100 eV). The six-fold symmetry of the hcp lattice is reflected in the six first-order reflexes [1-6]. In the right part of the picture, the reflexes of the second [7-8] and third [9-10] order are visible. b) LEED image (electron energy 100 eV) of 0.95 ML Au on Re(0001) after annealing, showing as well as the Re(0001) surface the six low-index reflexes and some higher order reflexes indicating a pseudomorphic growth of the first layer. c) LEED pattern (electron energy 120 eV) of 0.5 ML Ni on Re(0001) after annealing. The pattern reveals reflexes at the same positions as the pristine Re(0001) surface. The higher energy leads to the occurrence of higher order reflexes in the field of view. d) LEED pattern (electron energy 70 eV) of 0.66 ML Ni on Re(0001) without annealing. Here, one observes a set of six superstructure spots around each main reflex. Additionally, between them, there are weak reflexes marked by yellow arrows.

Another reflex can be seen between the main reflexes, marked with yellow arrows. These reflexes are weak, indicating little contamination with residual gas molecules. As known from previous studies [73, 119, 26] CO molecules form islands of a regular

2×2 superstructure even for a small number of adsorbed molecules. The absorption of the gas at certain periodic lattice sites could explain this arrangement of the reflexes. Comparable LEED measurements of four atomic Ni layers on Re do not show these reflexes [79].

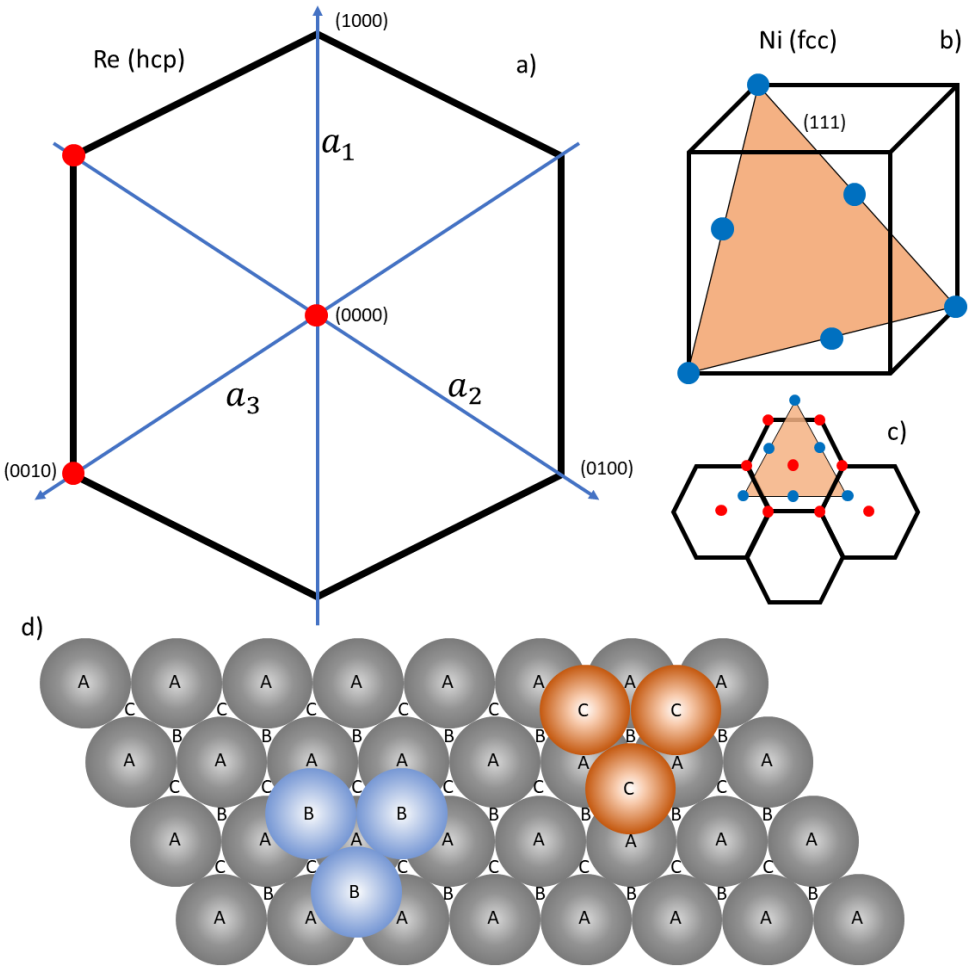

Fig. 5.2. The sketch illustrates the growth from Ni(111) on Re(0001). The hcp crystal lattice of Re is the densest spherical packing. Re(0001) is oriented so that the hexagonal pattern, shown in a), can be seen from the top view. Ni grows in the fcc lattice, which is the second variant of the densest sphere packing. The (111) plane is a diagonal cut through the crystal (b). In c) is shown how the (111) plane lies over the Re(0001) surface without displacement. There are two possibilities for the relative position of an atomic layer compared to the two layers below. In d), both possibilities of the densest sphere packing are shown. Based on layer A, either layer B or layer C can be formed. Both are the densest sphere packing and cannot be distinguished in LEED measurements.

Close to each main reflex, a set of superstructure spots occurs. The superstructure pattern, corresponding roughly to a 10×10 superstructure originates from the moiré pattern that forms when the lattice constants of substrate and adsorbate differ slightly. Starting with the second layer there is a relaxation of the lattice constant for subse-

quent layers. Therefore, additional layers grow epitaxially with a lattice constant that approaches the bulk value. This growth mode is further confirmed by STM images discussed in the following that directly image the moiré patterns, which are visible up to the tenth layer [79]. The LEED images offer the possibility to deduce the residual strain of the adsorbed layers averaged over a larger fraction of the sample surface.

Taking LEED measurements into account, the growth of an fcc-lattice can be reconstructed from Au or Ni onto Re(0001). Both fcc and hcp lattices are the two realizations of the densest sphere packing and therefore perfectly fit together as crystal lattices. As in Fig. 5.2 b) it is not the (100) plane but the (111) plane of the fcc unit cell that is needed to fit the hcp lattice aligned in (0001)-direction, as shown in Fig. 5.2 c). In Figure 5.2 a) the main axes (a_1, a_2 and a_3) of the hcp lattice are drawn. Accordingly, the first fcc layer grows pseudomorphic with the fcc in-plane directions parallel to [1200][1-100] and [-2-100]. Thereby, there are two possibilities of growth as shown in Fig. 5.2 d). While the hcp lattice is formed of two alternating layers (ABABAB), the fcc structure shows an ABCABC structure. The first Ni monolayer can therefore grow in both C and B hollow sites. Because of the spatial averaging, it is impossible to distinguish the two possibilities in the LEED images: if the fcc position would be homogeneously distributed over the whole surface, the LEED image would be threefold. Thus, only atomic resolution STM images could provide information on this question.

5.2. STM Results

Using topographic STM measurements, local growth properties of Ni and Au on Re(0001) can be determined. Figure 5.3 a) shows a constant-current image of the cleaned Re single crystal surface at 4.6 K. The (0001) surface of Re shows large atomically flat terraces with an average step width of 40 nm separated in three regions by two diagonally running step edges. A few dark spots are marked by blue arrows. The brighter areas correspond to higher topography or larger LDOS. Respectively, the impurities appear as holes because of their low LDOS, possibly indicating adsorbed CO molecules or oxygen atoms remaining from the cleaning process [64]. One of these defects is shown in the magnified image depicted in Fig. 5.3 b). With a diameter of $d \approx 0.1$ nm and a length of $d \approx 0.2$ nm, the defect has an elliptical shape which, indicates a diatomic molecule. The defects can be found on the surface in three different orientations or as round spots with no orientation.

An STM image of the Re(0001) surface covered with 4 ML Ni, deposited at room temperature and before annealing is shown in Fig. 5.4 a). The islands with different sizes form a stacked coverage of up to seven atomic layers. Only by annealing at moderate temperatures (Section 4.6) the island morphology changes: the Ni forms closed atomic layers. In Fig. 5.4 c) a sample is shown after the annealing process but coated with only 0.15 ML Ni. Here, the step edge runs vertically, and there is a small Ni stripe attached to the edge. On the Ni/Re(0001) surface, a larger number of defects appear with respect to the cleaned Re surface, likely caused by the increased pressure during the metal evaporation process. A similar topography has been observed for submonolayer coverages of Au [Fig. 5.4 d)].

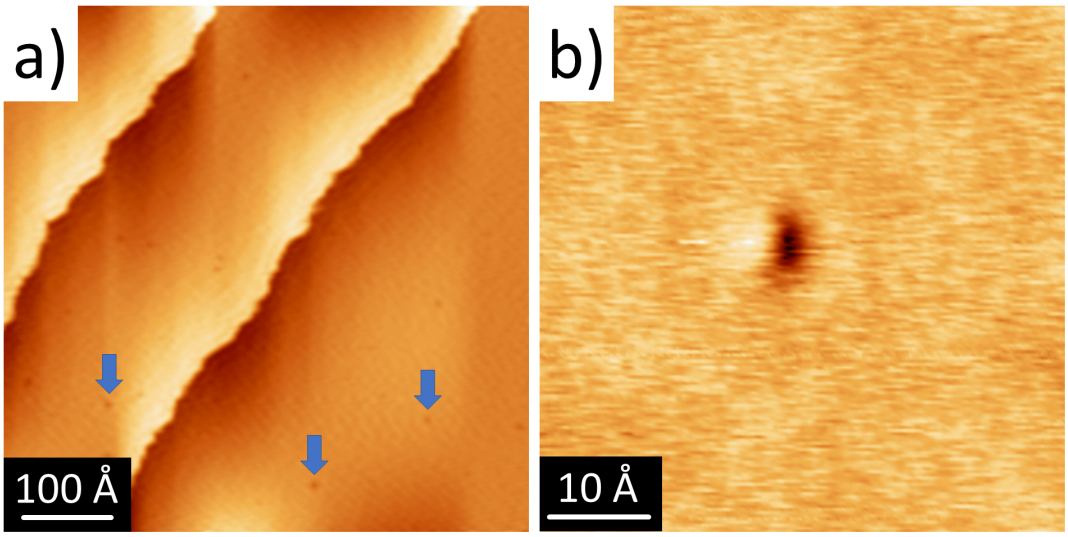

Fig. 5.3. a) Constant-current image of the cleaned Re(0001) surface ($V = 100\,\mathrm{mV}$, $I = 2\,\mathrm{nA}$), the blue arrows mark point defects appearing as dark spots due to a lower LDOS. b) An enlarged defect on the Re surface ($V = -250\,\mathrm{mV}$, $I = 3\,\mathrm{nA}$). The elliptical shape with a size of two to one ångström strongly resembles CO molecules likely caused by adsorbed residual gas molecules.

Figure 5.4 b) shows a STM image of 0.95 ML Au on Re(0001) grown at room temperature and before annealing. Au grows at submonolayer coverages as compact single-layer islands. In this case, the orientation of the step edges of the islands shows a preferential orientation, which is determined according to Section 5.1. The island edges are mostly formed by close-packed atomic rows in three equivalent axes separated by an angle of sixty degree corresponding to the symmetry of the Re(0001) crystal lattice, marked by black arrows. Single-layer thick Ni islands are mostly free of atoms in the second layer: there are very few Ni islands in the first layer where another island grows upon (examples marked with blue arrows), but often a Ni island grows over the edge and forms a second Ni layer (examples marked with green arrows). Therefore, the total coverage of second layer Au is about 6% compared to coverage of Au islands on the Re terraces of 89%. The Au atoms eventually hitting an already existing Au island migrate to the island boundary and pass the island edges by dropping over the Au step edge to enlarge the first layer islands, which indicates a small energy barrier of the islands (Schwoebel barrier) [8, 9].

At larger coverages of 0.95 ML Au on Re the closed Au surface forms small holes and defects which reduce the strain of the surface layer caused by the lattice mismatch, as shown in example Fig. 5.5 b). Interestingly, this phenomenon does not occur for Ni, although the strain is much higher. A limit of the area of adsorbed Au islands is resulting, making the examination of surface states on Au at a coverage of one monolayer difficult. The occurrence of holes and defects in the Au monolayer is independent of the annealing temperature in a wide temperature range. The STM image shown in Fig. 5.5 c) depicts a Ni coverage of 4 ML. A height difference occurs at Re(0001) substrate steps between the nth layer on an upper terrace and the $(n+1)$th layer on a lower terrace

decreases steadily with increasing Ni thickness. At the transition between the first and second monolayer, the substrate step leads to a height difference of $h_{1\to2} \approx 60\,\text{pm}$. At the transition between the third and fourth monolayer there is only $h_{3\to4} \approx 40\,\text{pm}$ an form sixth and seventh monolayer it is reduced to $h_{6\to7} \approx 20\,\text{pm}$. Thus for larger coverages, the underlying step edges of the Re crystal play only a minor role, and after 20 ML layers the height difference is no longer detectable. The Ni step edges are no longer parallel to the high-density directions as in the case of monolayer islands but are freely oriented.

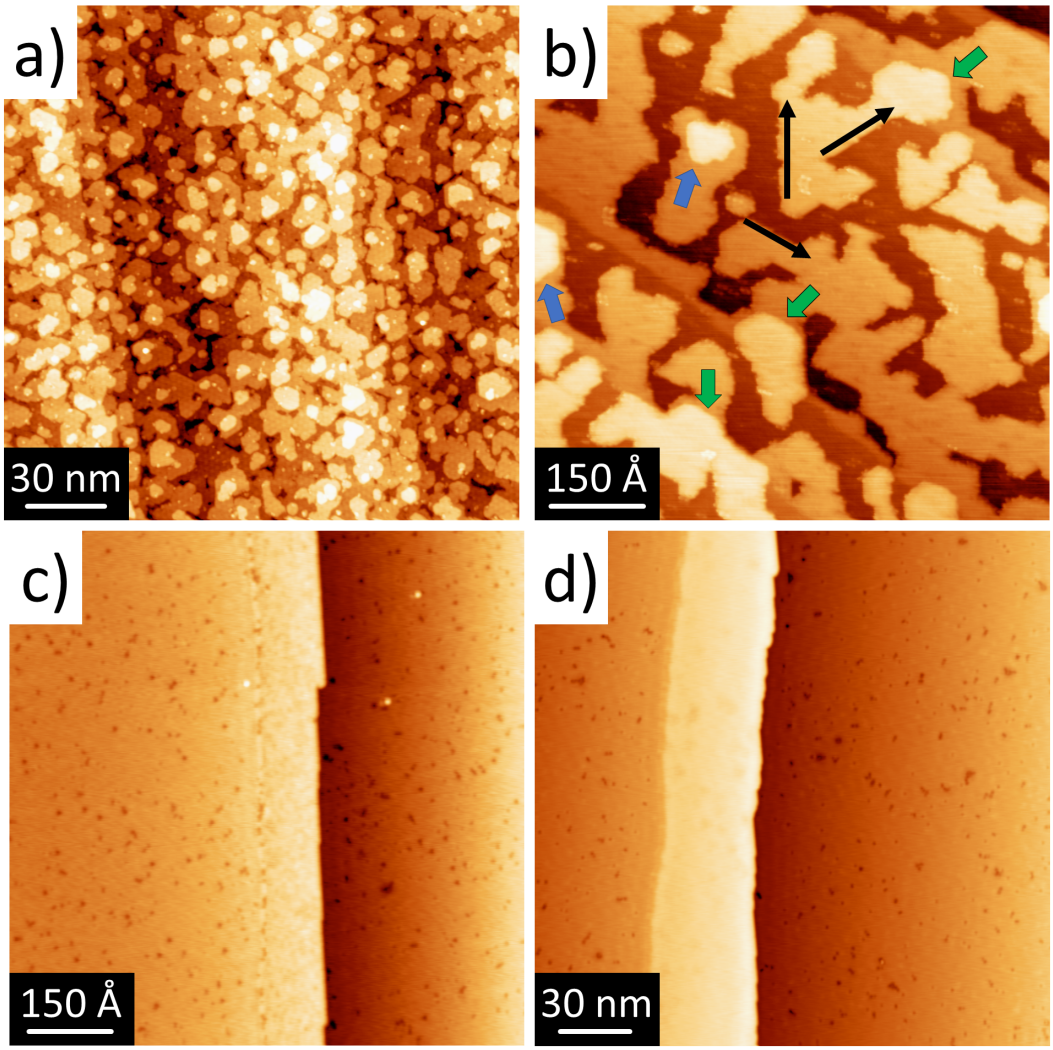

Fig. 5.4. a) the Ni plated Re-crystal with 4 ML of Ni deposited before annealing ($V = 1000\,\text{mV}$, $I = 0.1\,\text{nA}$). There are no defects visible but the Ni is distributed on 7 different layers of islands. b) Au (0.95 ML Au) islands on Re before annealing ($V = -1000\,\text{mV}$ $I = 0.5\,\text{nA}$). The arrows mark the three crystal axes of preferred island edges. c) 0.15 ML Ni coverage on Re after annealing ($V = 50\,\text{mV}$ $I = 2\,\text{nA}$), due to the vapor deposition process there are clearly more defects to be seen. d) The Re surface covered with 0.15 ML of Au after annealing ($V = 50\,\text{mV}$, $I = 2\,\text{nA}$). A brighter stripe attached to the step edge is formed by the Au coverage.

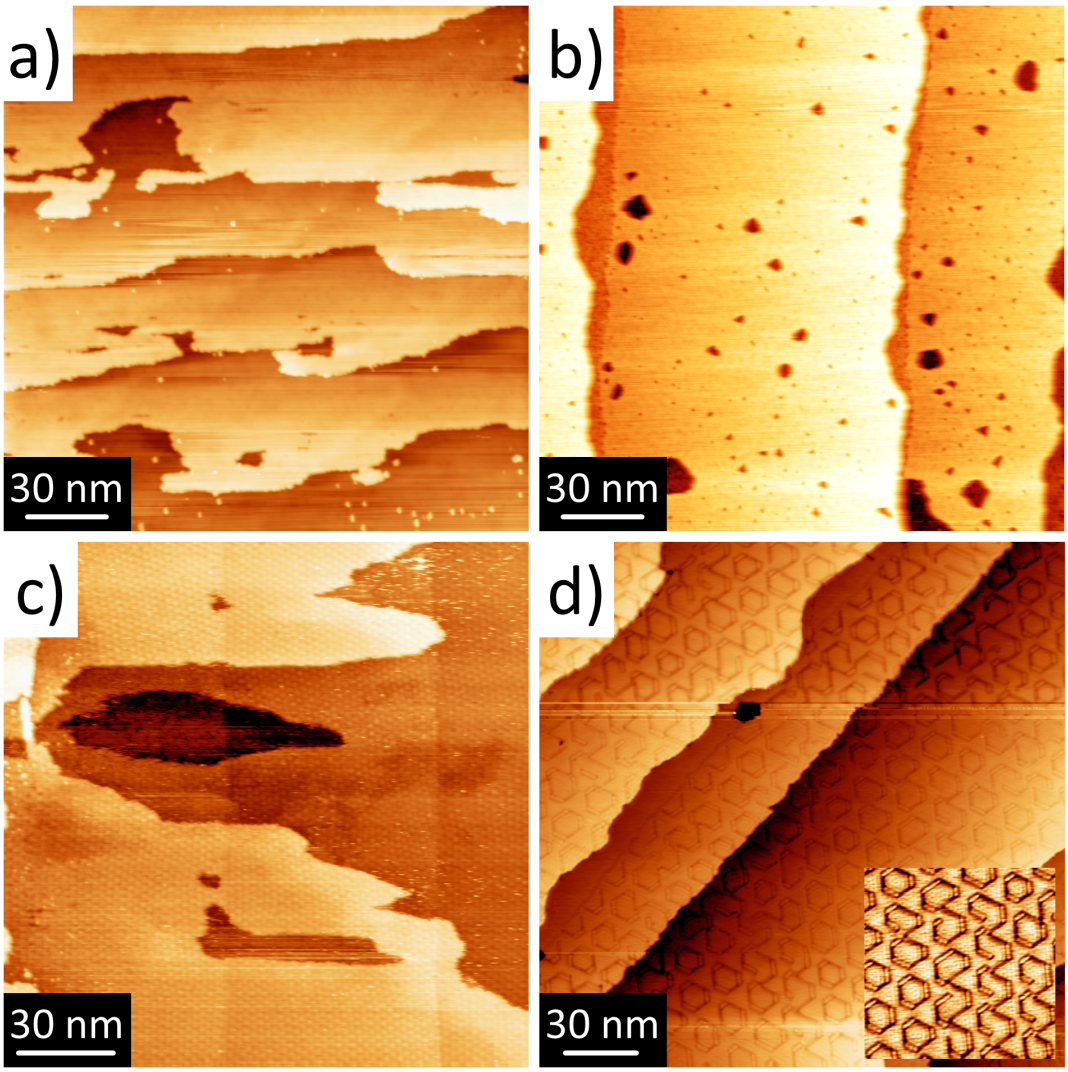

Fig. 5.5. a) 20 ML Ni on Re surface ($V = 50\,\text{mV}$, $I = 2\,\text{nA}$), the moiré pattern known from smaller coverages disappears, and the surface is smooth, but marked by larger holes to reduce the tension. In contrast to Au, Ni has a rather flat surface with small droplets of Ni. b) The Re surface covered with 0.95 ML of Au after annealing ($V = 50\,\text{mV}$, $I = 2\,\text{nA}$). Broader Au strips have significantly more defects and larger holes despite annealing. c) The Ni plated Re-crystal with 4 ML of Ni deposited after annealing ($V = 325\,\text{mV}$, $I = 2\,\text{nA}$). The step edges are no longer straight as in Re but grow in free curved forms. The moiré pattern is clearly visible on the upper layers. In d) a picture with a size of $(180 \times 180)\,\text{nm}^2$ measured at $I = 2\,\text{nA}$ and $V = -0.125\,\text{V}$ of a 3.5 ML Au/Re surface after annealing is shown. A close up with a size of $(60 \times 60)\,\text{nm}^2$ taken at $I = 2\,\text{nA}$ and $V = 0.1\,\text{V}$ is shown in the inset. A labyrinthine pattern is formed by the multi-layered gold surface.

To compensate the strain, stemming from the mismatch between the lattice constants of Re and Ni, a moiré pattern is formed on the Ni surface starting from the second layer. This is created by the superposition of the two regular atomic lattices: a symmetrical

pattern of dark and light points with an average spacing of 2.5 nm forming a 10×10 superstructure. The superstructure disappears with larger coverages of several atomic layers shown in Fig. 5.5 a). Here a lot of small Ni droplets appear. In addition, larger holes are formed in the top layer to reduce strain in the material by enlarging the edge areas. Larger coverages of Au behave significantly different compared to Ni. Figure 5.5 d) illustrates the growth of 3.5 ML Au on Re(0001). Thicker Au coverages form a labyrinthine structure. In the enlarged insert, the six-folded structure of the pattern can be observed. Just as in the case of the Ni this is formed to relieve the strain within the layers caused by the mismatch between the lattice constants of Re and Au. Except for one hole, the Au layer is closed. The step edges are relatively smooth and parallel.

6. Results and Discussion: Surface States

The theory of surface states was discussed in Section 3.6. On Re(0001), a Tamm state forms, a surface state that is described more suitable with the tight-binding model. The surface state was predicted by theoretical calculations and confirmed by ARPES measurements [26]. Using STM, one observes quantum interference patterns. The surface state leads to the quantum interference state when it is scattered at defects and step edges. In the following, the most important findings are discussed.

In this chapter, the results of the experiments, performed for the investigation of the Tamm surface state, are presented. Parts of the results have been published in Ref. [120]. After a general analysis of the wavelength (Sec. 6.1), the attenuation of the quantum interference patterns with increasing distance from defects is discussed in detail (Sec. 6.2). By examining the phase angles of the states in the vicinity of step edges, clear differences between the variable step decorations were found (Sec. 6.3). The surface state on the gold layer is discussed in Section 6.4. The examination of the surface states with spin resolution can be found in the following Paragraph 6.5. In most measurements, regular long-range defects, discussed in Section 6.6, occur.

6.1. Wave Length Analysis

To characterize the surface state one of the most important properties is the energy dispersion. In the case of the surface state on Re(0001), the wavelength of the surface state increases with increasing energy. To study the energy dispersion, we measure spectroscopic dI/dV maps on the pristine Re(0001) surface and the Re(0001) surface with submonolayer coverages of Au and Ni.

Figure 6.1 shows representative dI/dV maps at various energies and two different surfaces: Re(0001) [Figs. 6.1 a)-e)] and Au/Re [Figs. 6.1 f)-j)]. They were measured in the same region as in Fig. 5.3 a) and Fig. 5.4 d). The dI/dV maps show quantum interference patterns originating from the reflection of electron waves from defects. Step edges, representing a one-dimensional defect, result in a planar wave front, while point defects cause concentric patterns. The images display results for five different energies, as indicated in Fig. 6.1, to show the energy-dependent wavelengths of the standing wave pattern. The wavelength is directly related to the dispersion relation of the surface bands [27, 28]. The quasiparticle interference pattern is caused by the scattering between initial and final states at the same constant-energy contour in momentum space. For binding energies above 0.35 eV and below -0.2 eV, the amplitude of the QPI pattern becomes very weak, preventing the determination of the wavelength. The decreasing amplitude might be caused by an increasing hybridization with bulk states.

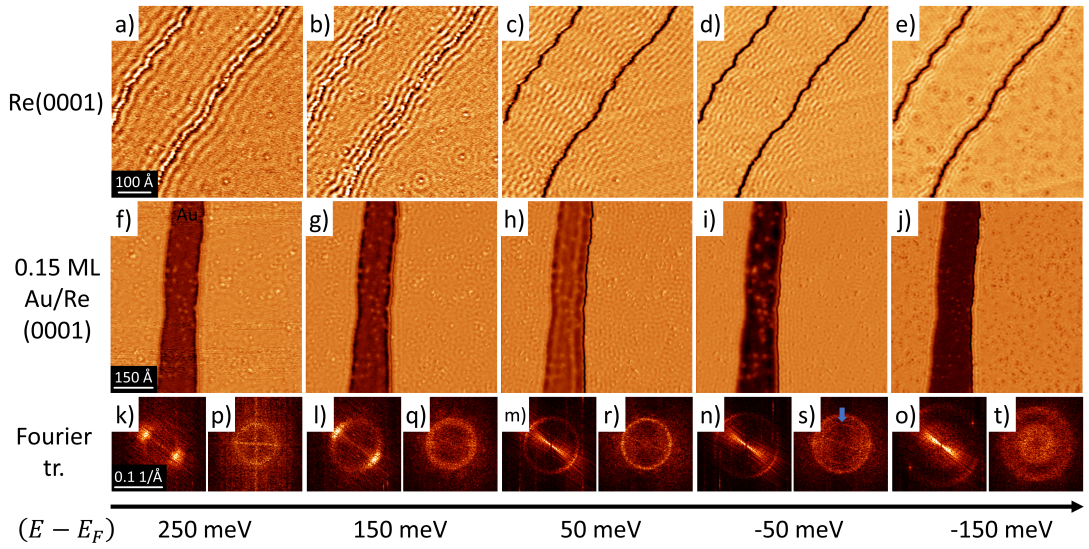

Fig. 6.1. Quantum interference patterns at different energies a)-e) on Re(0001) and f)-j) on 0.15 ML Au/Re(0001); dI/dV maps were recorded with tunneling parameters of $I = 2\,\mathrm{nA}$, $V_{\mathrm{mod}} = 6\,\mathrm{mA}$, and variable tip-sample voltage. Corresponding topographic images are shown in Fig. 5.3 a) and Fig. 5.4 b). The evaporated and annealed Au coverage in the second row covers about 15 % of the surface. k)-t) Power maps from two-dimensional Fourier transformation of the dI/dV maps for clean [k)-o)] and Au-covered [p)-t)] Re(0001). The double-ring phenomenon, marked, for example, in s) by a blue arrow, is discussed in the text.

The power map of the two-dimensional Fourier transformation (FT) [Figs. 6.1 k)-t)] reveals a centered ring-shaped feature that is caused by the quantum interference pattern. The diameter increases with decreasing energy, reflecting the decreasing wavelength in the dI/dV maps. The ring-shaped feature indicates an isotropic effective mass of the corresponding surface state [121]. Two intensity maxima on the ring are caused by the planar wave front originating from the step edges. The fanning-out lines, which are rotated by 90° relative to the step direction in the real-space image, originate from the step edges, too. The dI/dV and power maps for submonolayer coverages of Ni look very similar to those of Au-covered surfaces.

Additional ring-shaped features appearing in some power maps [as marked in Fig. 6.1 s)] are caused by the stabilization voltage for the tip height in constant-current mode [122]. This artifact arises from spatial modulations in the transmission function due to variations in z at each (x, y) pixel that are dependent on the set-point conditions. Figures 6.1 g) and h) show a quantum interference pattern on the thin Au stripe. For more accurate data, this pattern was investigated on a Re surface covered with 0.95 ML Au (discussion in Section 6.4). The pattern can be observed in an energy range from 80 to $-25\,\mathrm{meV}$ and indicates the presence of a surface state on the monolayer Au on Re(0001), too. On the Ni monolayer, there is no comparable pattern visible.

For evaluation of the FT power map, a radial average over the whole image area is used. The maxima are determined using a Gaussian fit. The resulting dispersion relations, shown in Fig. 6.2, are obtained by averaging five to ten independent measurements.

Within error limits, the dispersion relation for the Tamm surface state on Re(0001) is identical for pristine Re, Au/Re, and Ni/Re. This is also shown by the effective masses of $m^*_{Re} = -0.30\,m_e \pm 0.01\,m_e$, $m^*_{Au/Re} = -0.31\,m_e \pm 0.01\,m_e$, and $m^*_{Ni/Re} = -0.30\,m_e \pm 0.01\,m_e$ determined at the Γ point via parabolic fits. The result is also in good agreement with ARPES measurements and density-functional theory calculations [26]. However, because the DOS oscillations are generated by a linear combination of the Rashba split wave vectors, the presence of the Rashba effect could not be verified by FT of STS measurements [19, 20].

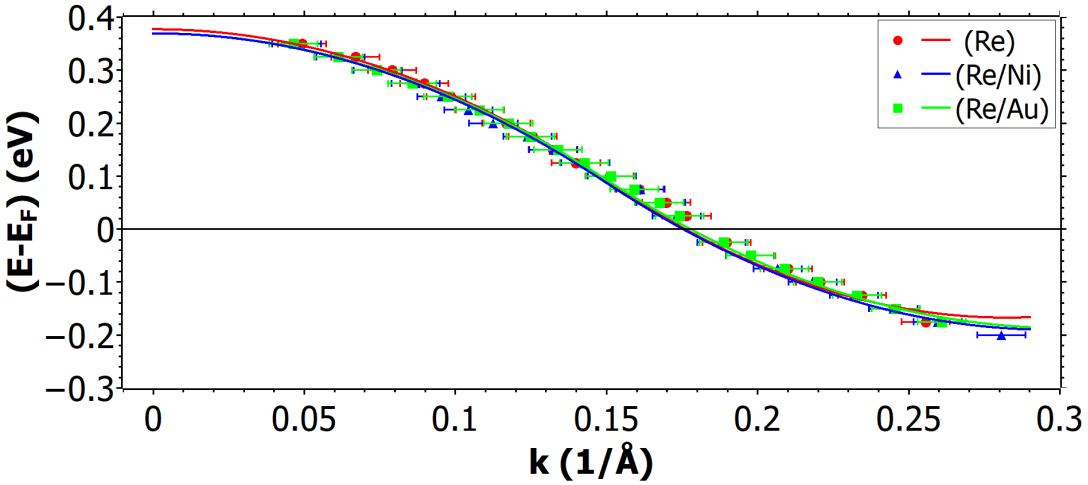

Fig. 6.2. Energy dispersion relation (energy vs wavenumber) deduced from Fourier power maps for the three samples, pristine Re(0001), 0.15 ML Au/Re(0001), and 0.15 ML Ni/Re(0001). For the data acquisition, five to ten series of measurements are averaged. There are no significant differences between the results for the three samples. The solid line is a plot of two parabolas, which are connected continuously at the inflection point. Because of the continuity condition, the lower parabola has only one free parameter and fits slightly less accurate than the parabola at the Γ point.

Quantum interference patterns result from scattering events, where the scattering wave vector combines two states with opposite momenta. For a spin momentum locked Rashba state interband backscattering is forbidden to first order. Intraband scattering from the inner to the outer Rashba band is allowed instead. The scattering vectors of inter- and intraband scattering differ slightly. Small differences between ARPES and STM data are in favor of interband scattering between the two branches of the Rashba split surface state.

6.2. Attenuation

For further analysis, we discuss the decrease of the scattering amplitude with increasing distance from the step edge. Reference [123] reports that a spin-prohibited scattering process leads to a more rapid decay of the standing wave pattern than an allowed scattering process. The attenuation factor has been experimentally and theoretically investigated for various materials, resulting in an exponent of $\beta = -1/2$ for allowed

backscattering and $\beta = -3/2$ for forbidden backscattering regarding the following fit function:

$$A = A_0 \sin(bx + c) \left(\frac{x}{x_0}\right)^{\beta} + d. \tag{6.1}$$

Figure 6.3 shows the analysis of the amplitude attenuation at the step edges on pristine Re as well as on the surfaces with step decorations. Table 6.1 summarizes the fitted values for β. The attenuation exponent varies between upper and lower terraces. For the upper terrace $\beta \approx -1/2$ is determined, while for the lower terrace, the value is $\beta \approx -3/2$. The comparison of the experimental data (Fig. 6.3) with the fitted curve and with both model values indicates the significance of this result. The remaining differences of model values and fitted values showed up in other measurements as well [124].

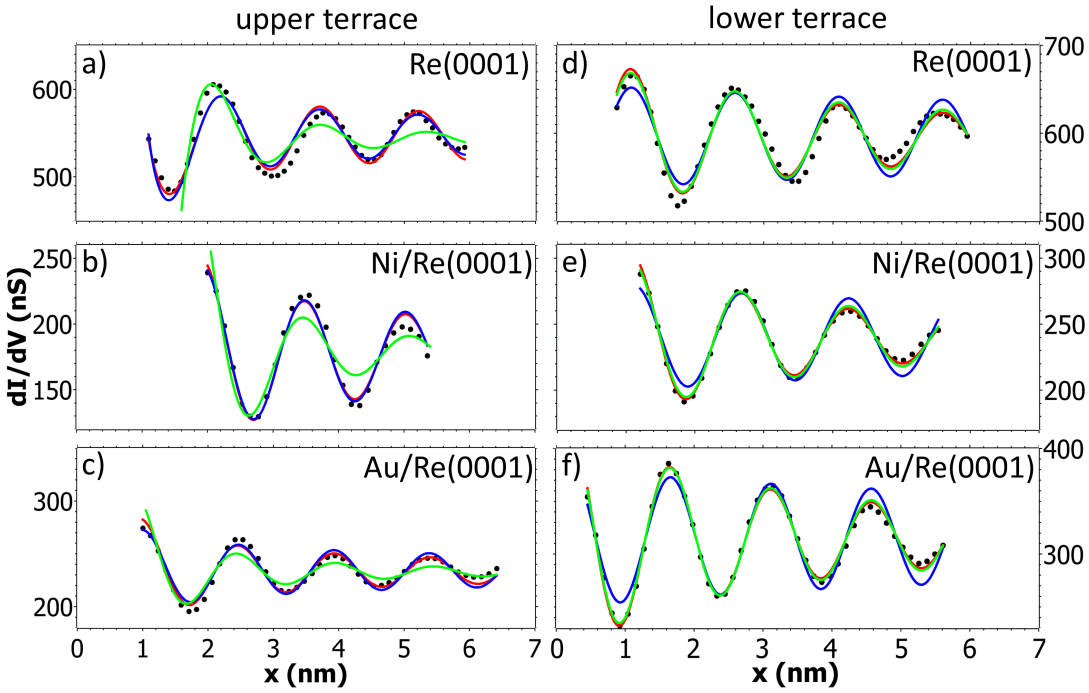

Fig. 6.3. Examples of the attenuation of quantum interference patterns at a step edge of a) the pristine Re, b) the Ni/Re and c) the Au/Re surfaces, measured with tunneling parameters $V = 100\,\mathrm{mV}$, $I = 2\,\mathrm{nA}$, $V_{\mathrm{mod}} = 6\,\mathrm{mV}$. The solid red line is the fit with Eq. (1) with parameters presented in Table 6.1. The blue (green) line represents Eq. (1) with an exponent of $\beta = -1/2$ ($\beta = -3/2$). A significant difference between upper and lower terraces is noticeable.

We assume that the differences are explained by the fact that the SS on the lower terrace scatters partially into bulk states. This scattering into bulk states is not possible on the upper terrace for geometrical reasons. Therefore, fewer electrons will be backscattered on the lower terrace, which leads to a faster decay of the QPI pattern. Another reason for the different attenuation behavior on both sides of the step edge is the so-called

smoothing effect [125], which causes the electron density not to follow the sudden change in geometry but to change smoothly from the upper to the lower terrace [126].

Upper terrace			
	Re	Ni/Re	Au/Re
Fig. 6.3	-0.37	-0.78	-0.59
Average	-0.52 ± 0.02	-0.66 ± 0.01	-0.70 ± 0.01
Lower terrace			
Fig. 6.3	-1.81	-1.65	-1.79
Average	-1.37 ± 0.16	-1.66 ± 0.06	-1.94 ± 0.14

Tab. 6.1. Calculated attenuation parameters for the measured wave patterns. The first row is related to the data in Fig. 6.3, the second row shows averages over all energies from −125 meV to 150 meV with the standard deviation of the mean value, representing a statistical error.

The surface state on the upper terrace is thus not suppressed for other reasons, and we take the data for the upper terrace for comparison with the model discussed in Ref. [123]. Thus, the smaller attenuation exponent of $\beta = -1/2$ determined for the unperturbed surface state on the upper terrace indicates an allowed interband scattering process.

6.3. Phase Angle

The analysis of the phase angle of the QPI pattern reveals a direct connection to the energy barrier: a phase of 0° implies a fixed end and a barrier wall with infinite height. A phase of 180° would correspond to a loose end with a negative energy barrier. Figure 6.4 illustrates the data evaluation process for the extraction of the phase with an example for pristine Re [Figs. 6.4 a)-d)] and one for Au/Re [Figs. 6.4 e)-h)]. The topographic images [Fig. 6.4 a) and e)] are used to determine the center of the step edge in half of the height decrease or increase in the height profiles shown in Figs. 6.4 b) and f). The simultaneously recorded dI/dV maps of the identical regions reveal the QPI pattern [Figs. 6.4 c) and g)]. The corresponding profile of the dI/dV modulation [Figs. 6.4 d) and h)] is separately fitted by Eq. (1) for the upper terrace with $\beta = -1/2$ and for the lower terrace with $\beta = -3/2$.

The example shown in Fig. 6.4 reveals a prominent difference between a pristine Re step edge and a step edge decorated with Au. In Fig. 6.4 d) both fits subtend the step edge at the maximum of about 90°, with the intersection points varying slightly. The Au/Re sample behaves contrarily at the same energy: the extrapolated wave of the upper terrace crosses the step edge at the minimum of about 270°, as can also be seen in Fig. 6.5. The intersection of the surface wave on the lower terrace is at about 40°. The behavior changes when the sign of the tip-sample voltage changes, which leads to a characteristic phase jump.

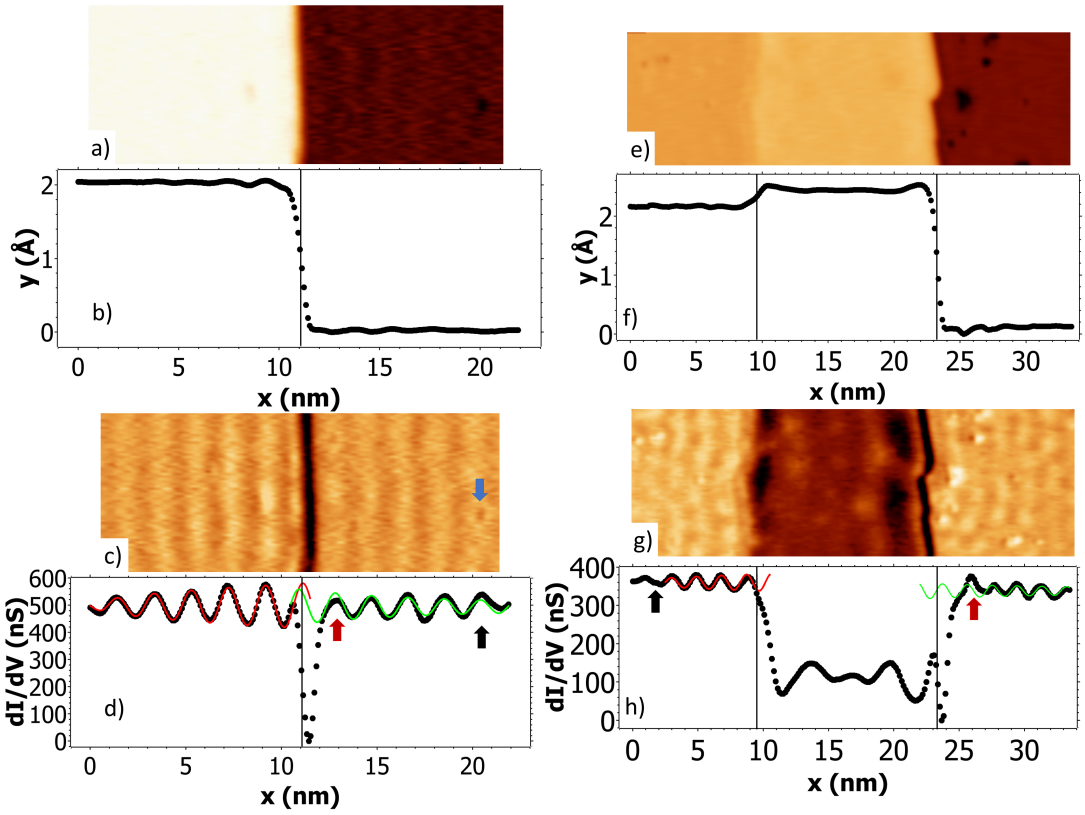

Fig. 6.4. Two examples for the determination of phase angles at an energy of $V = 75\,\mathrm{mV}$ with a tunneling current of $I = 2\,\mathrm{nA}$ are shown. a) and e) Topographic images of a step edge running vertically through the image, on a) Re and e) 0.15 ML Au/Re. b) and f) Height profiles along the horizontal axis. c) and g) Differential conductivity maps from the identical region shown in a) and e). d) and h) Profiles of the dI/dV values along the horizontal axis. By fitting and extrapolating the profile (red and green solid lines) to the center of the step edge (vertical black lines), the phase angle is determined. The red fits on the upper terraces are fitted by using Eq. (1) with $\beta = -1/2$; the green fits on the lower terraces are fitted with $\beta = -3/2$.

In both wave profiles, the red fit is more accurate than the green one. This can be explained by the fact that the first crest of the wave on the lower terrace, marked by a red arrow, does not match the surface state in amplitude and wavelength but is manipulated by the potential of the step edge. Therefore, the surface state was fitted from only the second peak onwards and extrapolated over the distance to the step edge. Even small imperfections have considerable effects on the wave profile. For example, the defect marked with a blue arrow in Fig. 6.4 c) changes the amplitude and wavelength of the last peak marked with a black arrow in Fig. 6.4 d). On the Au/Re sample, these effects were amplified by the higher defect density (black arrow). Due to the fringy step decoration, it is often not possible to obtain parallel wave crests over larger areas, which leads to the fluctuating amplitude and a particularly distorted first-wave crest as in Fig. 6.4 h). For this reason, narrower profiles were usually used to analyze the phase angles.

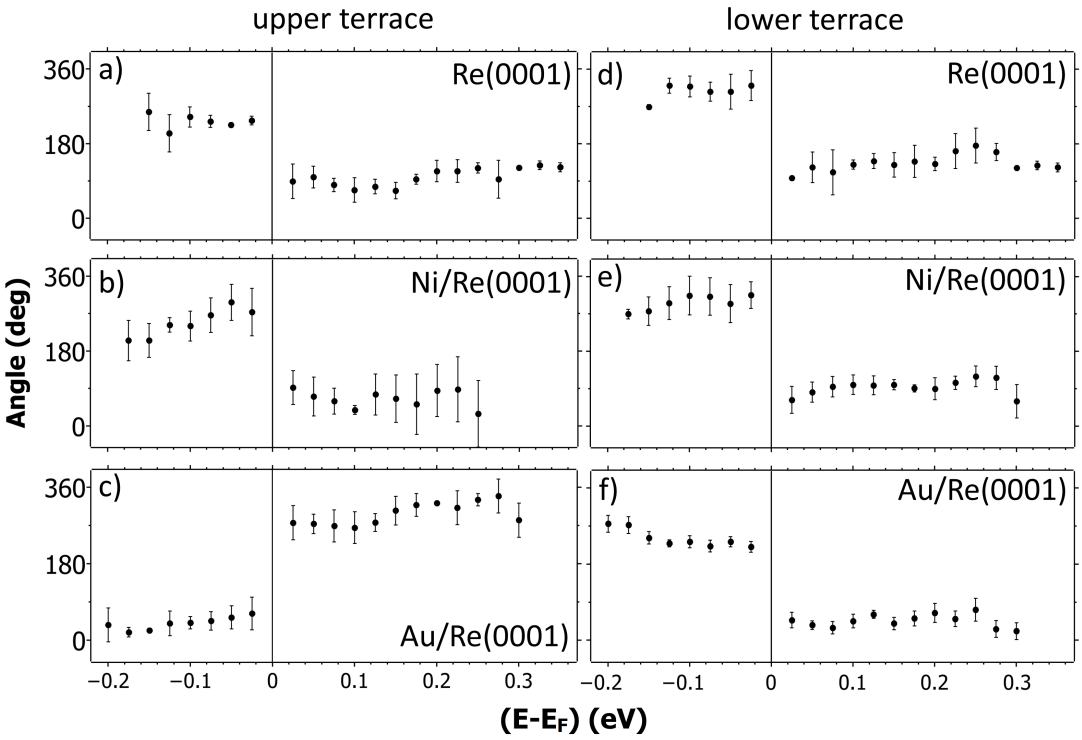

Fig. 6.5. The phase angles of the QPI at the step edge determined on the a)-c) upper and d)-f) lower terraces. The phase is determined with respect to the center of the step edge [Fig. 6.4]. Shown on a) and d) pristine Re(0001), b) and e) Re(0001) with 0.15 ML Ni evaporated, and c) and f) Re(0001) with 0.15 ML Au evaporated. The phase shift at E_F, where Au stands out with a reverse behavior, is remarkable.

Figure 6.5 summarizes the fit values for the phase for all samples and higher and lower terraces, respectively. The striking observation is a phase shift of about 180° at E_F, which is reflected in all measurements, independent of the step decoration. The error bars shown in the plots represent statistical errors resulting from averaging four measurements each. We are aware of additional systematic errors of the fit procedure, for example, the precise position of the step edge. The variation of the step edge position would result in a common shift of all phase angle values yet not eliminate the phase jump at E_F.

In addition to the phase shift, linear tendencies can be seen. With increasing energy, one observes a linear increase or decrease of the phase, which might be attributed to a change in the effective barrier height with energy. Generally, the lower range of phase angles is between 50° and 150°, and the upper range is between 250° and 350°. An average phase jump of less than 180° indicates a medium barrier height. The occurrence of the phase shift can be explained with the following model. With the STM, unoccupied sample states are investigated with negative voltages, and occupied sample states are investigated with positive voltages. Unoccupied states are known in semiconductor physics as holes with positive charge; occupied states are electrons with negative charge. A potential barrier, behaving like a wall for electrons, will become a valley for holes because of the opposite charge, resulting in a phase jump of

approximately 180°.

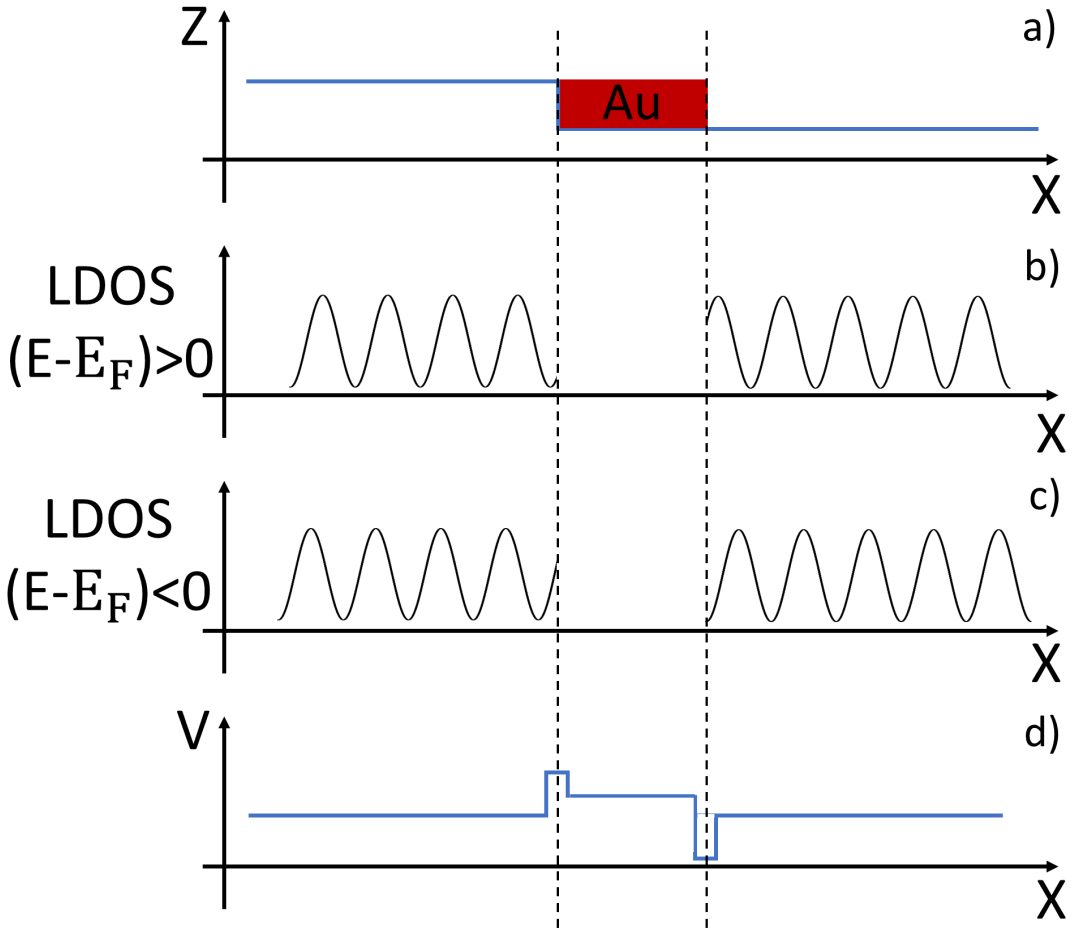

Fig. 6.6. This diagram shows the effect of the step edge, decorated with Au on the surface state and the potential. a) shows a cross-section of the surface. The step edge leads to a phase difference of the surface state between the lower and upper terrace. At the same time, there is a phase shift when passing through the Fermi energy, shown in b) and c). A double barrier with a potential wall from the upper terrace and a potential pot from the lower terrace can explain this phase difference.

While there is little difference between the upper and lower terraces for Re and Ni/Re, there is a significant difference for Au/Re: the phase shift is reversed on the upper terrace side of the step with respect to the other cases. This behavior is likely caused by the previously mentioned surface state on gold. On the upper terrace, the Au surface state and the SS on Re(0001) are coupled. Such a coupling is enabled by the fact that the topmost Re layer on the upper terrace is continued by the topmost Au layer at the same height. The line boundary between the topmost Re and Au layers is the one-dimensional analog to a two-dimensional metal-metal interface. The coupling of surface states is not possible on the lower terrace because the Re(0001) surface layer is not continued at the same height; hence, the behavior does not differ from the other step decorations.

Figure 6.6 sketches the influence of the Au step decoration on the surface state. Depending on whether positive or negative energies are measured, the phase and phase offset of the surface state on the two step edges are different [Figs. 6.6 b) and c)]. A possible potential V is shown in Fig. 6.6 d) for positive energies. On the upper terrace, the standing wave is reflected by a potential wall, on the lower terrace by a trench. This is the origin of the different phase angles for differently decorated steps, influenced by the coupling of the surface state on gold. The two potential barriers are reversed when the tip-sample voltage changes sign. Since the phase changes from the occupied to the unoccupied states, the potential wall now appears as a trench and vice versa, which explains the phase jump.

6.4. Surface States on Au

In addition to the surface state on Re, a second state was found on the deposited Au stripe. The surface state could not be further analyzed on 0.15 ML Au because the step decoration was too small to see the pattern in an expansion of several wavelengths. Therefore, a layer of 0.95 ML Au was deposited on Re for the investigation. To study the electronic state, we measured spectroscopic dI/dV maps on the Au/Re(0001) surface. Figs. 6.7 a)-e) shows representative dI/dV maps at various energies. They are measured in the region, shown in Fig. 5.5 b).

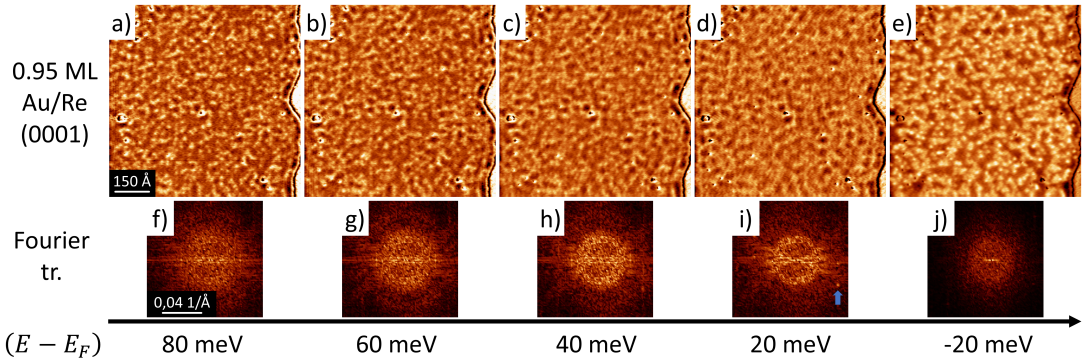

Fig. 6.7. a)-e) Quantum interference patterns at different energies on 0.95 M Au(111) on Re(0001); dI/dV maps were recorded with tunneling parameters of $I = 2\,\mathrm{nA}$, $V_{\mathrm{mod}} = 6\,\mathrm{mA}$ and variable tip-sample voltage. The evaporated and annealed Au covers nearly the complete surface to obtain larger areas with a surface state. f)-j) Power maps from two-dimensional Fourier transformation of the dI/dV maps for Au-covered Re(0001); In the FT-maps, the double-ring phenomenon can be seen. Additionally, a bright spot stemming from a disturbance frequency is marked by a blue arrow, for example, in i).

The dI/dV maps show quantum interference patterns originating from the reflection of electron waves from defects. Step edges, representing a one-dimensional defect, result in a planar wave front, while point defects cause concentric patterns, just as in the case of the surface state on Re. The image displays results for five different energies, as indicated in Fig. 6.7, to show the energy-dependent wavelengths of the standing wave pattern. The quasiparticle interference pattern is caused by the scattering between

initial and final states at the same constant-energy contour in the momentum space. For binding energies above 80 meV and below −20 meV, the amplitude of the QPI pattern becomes very weak preventing the determination of the wavelength. The decreasing amplitude might be caused by an increasing hybridization with bulk states.

The power map of the two-dimensional FT [Fig. 6.7 f)-j)] reveals a centered ring-shaped feature that is caused by the quantum interference pattern. The diameter increases with increasing energy, reflecting the increasing wavelength in the dI/dV maps. The fanning-out lines, which are rotated by 90 degree relative to the step direction in the real-space image, originate from the step edge. Additional ring-shaped features appearing in some power maps, such as in the Re(0001) measurements, are caused by the stabilization voltage for the tip height in constant-current mode [122]. Another feature are the bright spots in the FT-images, such as marked in Fig. 6.7 i) by a blue arrow. These are not caused by the surface state, but from a disturbance frequency.

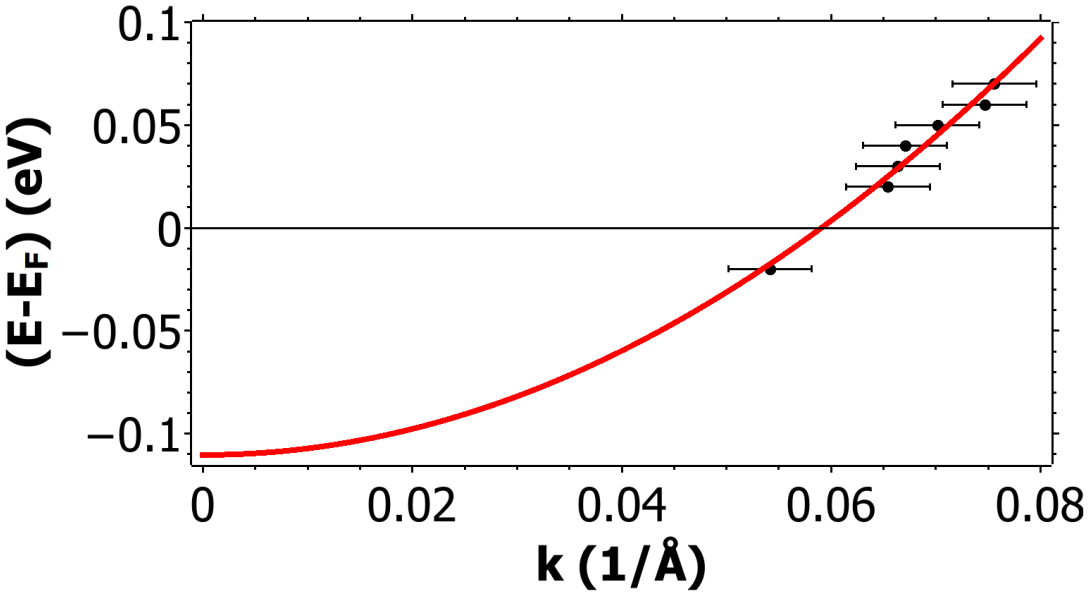

Fig. 6.8. Energy dispersion relation (energy vs wavenumber) deduced from Fourier power maps for 0.95 ML Au on Re(0001) surface state. For data acquisition, four series of measurements are averaged. In comparison to the surface state on Re, this one has an inverted gradient and is visible in a much narrower energy range. The solid red line is a parabola plot through the Γ point to determine the effective mass.

For evaluation of the FT power map, a radial average over the whole image area is used. The maxima are determined using a Gaussian fit. The resulting dispersion relation, shown in Fig. 6.8, is obtained by averaging four independent measurements. Since the rings in the FT images are slightly indistinct and blurred, the error bars are correspondingly large. Noticeable is the inverted slope compared to the surface state on Re, which leads to a positive effective mass of $m^*_{pAu} = 0.12\,m_e \pm 0.01\,m_e$. In addition, the state occurs only close to the Fermi energy and has a much lower amplitude, and it must be extrapolated very far to the Γ point. The obtained data is therefore not quite as reliable as the surface state on Re.

6.5. Surface States with Spin-Resolved STS

Another measuring method of the STM is the spin-polarized STS, presented in Section 2.6.1. In order to investigate the mechanism of backscattering on step edges and defects, spectroscopic measurements with a 10 ML iron-coated tip are performed. We measured spectroscopic dI/dV maps on the pristine Re(0001) surface and the Re(0001) surface with submonolayer coverages of ferromagnetic Ni for investigations of the Spin.

Based on an interband scattering of the electron waves at step edges and defects there are two possible scattering channels of the electrons. From the Rashba split band of the surface state, spin down and spin up electrons scatter into the opposite band with the same spin to avoid a spin-flip scattering. The electron density wave of the surface state on the pristine Re consists of equal parts of spin up and spin down electrons. In measurements with a magnetic tip, a suppression of one spin direction of the wave, depending on the orientation of the magnetic moment of the tip, would be expected. This suppression would not change the wave structure itself, but the amplitude would decrease by about half. If the waves scatter at the ferromagnetic Ni step decorations, this behavior could change. Depending on the orientation of the magnetic moment in the Ni, one spin direction is directly suppressed by the step decoration. If the orientation of the magnetic moment of the tip is antiparallel to the Ni step decoration, both spin directions would be suppressed, with the effect, that no wave fronts parallel to the Ni step decoration can be observed. The circular waves around the defects have a reduced amplitude but should still be measurable.

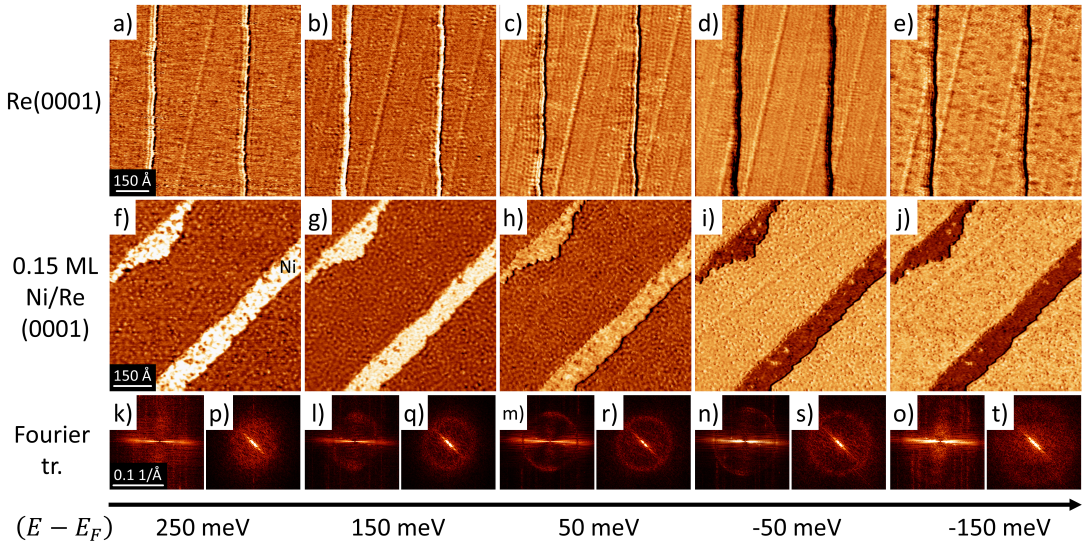

Fig. 6.9. a)-e) Quantum interference patterns at different energies on Re(0001) and on 0.15 ML Ni/Re(0001) in f)-j); The dI/dV maps are recorded with tunneling parameters of $I = 2\,\text{nA}$, $V_{\text{mod}} = 6\,\text{mA}$ and variable tip-sample voltage. For these measurements the tunneling tip is covered with about 10 ML Fe, for spin-resolved measurements. The evaporated and annealed Ni coverage in the second row covers about fifteen percent of the surface. k)-t) Power maps from two-dimensional Fourier transformation of the dI/dV maps for clean [k)-o)] and Ni-covered [p)-t)] Re(0001).

In Fig. 6.9 representative dI/dV maps at various energies on two different surfaces are shown: Re(0001) [Figs. 6.9 a)-e)] and Ni/Re [Figs. 6.9 f)-j)]. The dI/dV maps show quantum interference patterns from step edges, resulting in a planar wave front and point defects, causing concentric patterns as seen in the other power maps of surface states. The image shows results for five different energies, as indicated in Fig. 6.9, to show the energy-dependent wavelengths of the standing wave pattern. Also, the other properties are similar to the non-spin-resolved measurements. The amplitude of the quantum interference patterns is significantly smaller than in the case of a pure tungsten tip. This observation agrees with the expectations: the suppression of one spin component can reduce the amplitude. Additionally, it could be that the different tip material causes a smaller tunneling matrix element for the investigated surface state. The small-amplitude also causes the occurrence of additional straight lines in the dI/dV maps discussed in Section 6.6. It is further noticeable that the amplitude of the quantum interference patterns on the upper terrace is significantly larger than the amplitude on the lower terrace.

The power map of the two-dimensional FT [Figs. 6.9 k)-t)] reveals a centered ring-shaped feature that is caused by the quantum interference pattern with the same dispersion as the spin-averaged measurements. One also observes the fanning-out lines, which are rotated by 90° in relation to the step direction in the real-space image, which originate from the step edges. In the spin-averaged measurements, there are two intensity maxima at the crossing point between the fanning-out lines and the ring of the surface state. This behavior could be explained by the planar wave fronts alignment parallel to the step edges. These maxima do not appear in the spin-polarized FTs, instead, they even seem to turn into a minimum, as can be seen clearly in Fig. 6.9 m). This behavior can be explained by a negative superposition effect of the step edges, which are strongly pronounced in this measurement. Nevertheless, it is interesting that in this measurement many waves run orthogonal to the step edges. Their origin is not visible in the measurements, but this phenomenon increases the intensity of the ring in the vertical axis in the Fourier transformed image.

The measurements of the Ni/Re sample show a comparatively uniform wave pattern without prominent wave fronts near the step edges. This is also reflected in the Fourier transformed images. In the FTs of these measurements, the rings of the surface state are much more symmetrical, without minima or maxima. This behavior was exactly expected for spin-resolved measurements with Ni step decoration. Also, in this case, there is an explanatory approach that can explain the observations: due to the significantly higher defect density, there are significantly more circular waves overlaying the wavefronts in this measurement. However, it was not possible to perform enough spin-resolved measurements to formulate a significant result, but the measurements strengthen the assumption of interband scattering as the dominant scattering mechanism from the previous sections.

6.6. Line Defects

In many of the dI/dV maps shown in the previous chapters, a feature occurs that has been ignored so far. To investigate this feature, additional measurements were performed on the pristine Re(0001) crystal. Figure 6.10 shows representative dI/dV maps: in a)-e) consecutive measurements, taken at $V = 100\,\mathrm{mV}$, and in f)- j) a series of measurements around the Fermi energy. On the dI/dV maps the quantum interference patterns, originating from the reflection of electron waves from defects and step edges, show up as discussed in the previous chapters.

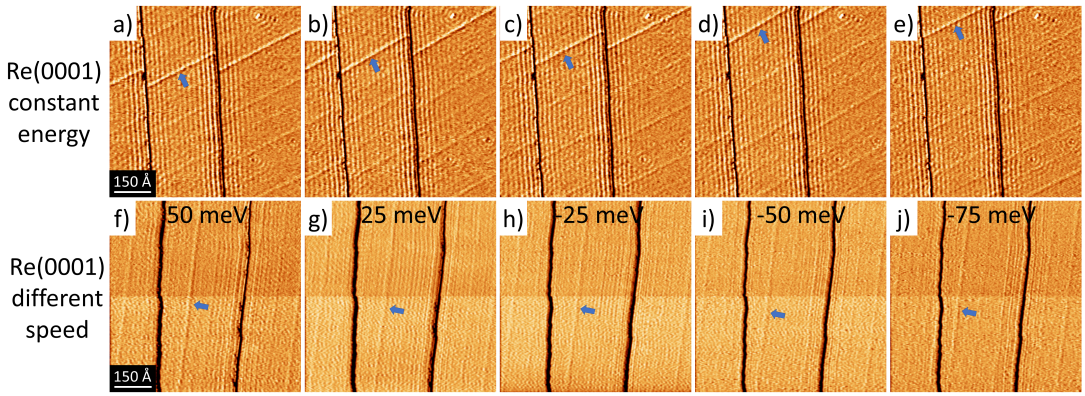

Fig. 6.10. a)-e) Quantum interference patterns on Re(0001), measured at constant energy ($V = 100\,\mathrm{mV}$); f)-j) dI/dV maps of Re(0001), measured at different energies; The dI/dV maps are recorded with tunneling parameters of $I = 2\,\mathrm{nA}$ and $V_{\mathrm{mod}} = 6\,\mathrm{mA}$. Some particularly strong lines are marked with blue arrows. The series in the first row is measured for constant tunneling parameters. The STM images in the second row are scanned with two different scanning speeds: the upper half of the images is measured at $V_1 \approx 97.5\,\mathrm{nm/s}$ and the lower half at $V_2 \approx 46.5\,\mathrm{nm/s}$. The lower noise level for the slower scanning speed leads to a slightly different color scale in the upper half of the images.

In the dI/dV maps of Figs. 6.10 a)-e) straight lines appear on top of the quantum interference patterns. The straight lines of increased dI/dV values extend over the complete image frame, and are perfectly parallel to each other. Their intensity varies slightly over the image frame. The feature is appearing as a wave moving slowly with varying speed in the direction of the upper edge of the measurement. A particularly characteristic strong wave is marked with a blue arrow in Figs. 6.10 a)-j). Figs. 6.10 a)-e) are measured consecutively with identical tunneling parameters. In the images eight lines are visible that have precisely the same distance from each other. The angle and the distance of the parallel lines remain the same during the complete series of measurement. The lines are interrupted at step edges and shifted along the y-direction by almost a complete line distance. Because the images are recorded with a constant scan velocity, the observed line structures translate into a distinct periodicity in time. In some cases, similar lines show up when disturbance frequencies on the tunneling current are present. However, in this case, one would not observe interruptions at step edges but straight lines across the complete image frame. To further exclude disturbance frequencies on the tunneling current, dI/dV maps were recorded with

different scan speeds.

Figures 6.10 f)-j) show a second series of STM images. Here, the scanning speed is changed after half of the frame is recorded. In this case, the lines are more vertical. The lines are again parallel to each other and show the same characteristic interruptions at step edges. The main result of this series is that the lines do not show a change of the slope if the scanning speed is abruptly changed. Such a change of slope would be expected if the lines originate from a constant disturbance frequency. Moreover, the series shows that the directions and distances of lines do not change with the tip-sample voltage. Such changes can be expected when the observed lines would be true sample-related structures.

The line-shaped features are identical for the forward and backward image. Also, the orientation of the lines does not change, whether the starting point of the following image scan is the endpoint of the previous measurement and consecutively is measured in the opposite direction (from right to left) or whether the tip is moved to the starting point of the previous scan and then the next measurement is started. This leads to the conclusion that the appearance of the parallel lines is independent of the scanning process.

The observed line features can be found in almost all dI/dV maps but not in the corresponding topographical images. All lines are interrupted at step edges continued after a jump in the y-direction. The parallel lines always have the same distance within a series of STM measurements. The orientation of the lines may strongly vary for different measurement series. In summary, the observed line features do not relate to true electronic variations on the sample surface, as excluded from the series of STM images with constant tunneling parameters. The lines do not depend on the tunneling parameters, such as tip-sample voltage or scanning speed and direction. Disturbance frequencies on the tunneling current can be excluded because of the line jumps at step edges. The only remaining reproducible parameter is the scanning position itself, i.e. the combination of voltages applied at the piezo scanner tube. This would explain the same distances within one measurement and the different intervals. The peak-increased dI/dV value at a certain position is reproducible because the same voltage is applied to the scanner. Increasing the y-voltage adds a certain shift to the x-voltage causing the same dI/dV peak, explaining the straight-line features. Also, the offset of step edges is explainable: due to the changed topography, an additional z-voltage must be applied to the piezo tube.

For a new series, the tip will be approached with a different voltage offset and the sample may be tilted macroscopically differently. This explains the large differences in line orientation for different series. While the observed lines can be clearly attributed to combinations of scanning piezo voltages, their origin is not clarified yet. The combination of x-, y-, and z-voltages leads to a certain strain condition on the tube scanner. Therefore, the origin is either a pure electronic reason related to the scanning voltages or a mechanical oscillation of the scanner under certain strain conditions. Because we never observed such lines in the dI/dV maps before, we are inclined to attribute the line features to the new STM electronic setup installed prior to the experiments for this thesis.

7. Results and Discussion: Inverse Transition Upon Cooling

During the course to grow ultrathin Ni films on Re(0001) for magnetic investigations, an interesting instability of the Ni surface of the films occurred, which is in the following investigated in more detail. The movement of Ni adatoms at low temperatures in the STM is detected for the first time. Since the mobility of Ni decreases at higher temperatures, the phenomenon is related to inverse melting, as discussed in Section 3.3. In the two-dimensional system of thin Ni layers on Re(0001), the process of melting is not definable. Hence, the mechanism is better described as an inverse transition upon cooling or the decrease of the energy barrier for mobilization upon cooling. In this chapter, the results of the measurements are presented to find a model for the movement of the Ni atoms.

The main part of this chapter focuses on the investigation of the mobility of Ni at low temperatures (Sec. 7.1) and the discussion of the measurements (Sec. 7.2). In the following, some additional phenomena are presented. First, the mobility of Ni at intermediate temperatures in the range of liquid nitrogen is described in Paragraph 7.3. The motion of particularly large and small coverages of Ni is treated in Section 7.4. Then, there is a short digression into the differences to the system Au/Re compared to Ni/Re (Sec. 7.5). Finally, measurements with a magnetic tip are presented and discussed (Sec. 7.6).

7.1. Mobility Measurements

Fig. 7.1 shows four series of STM images successively recorded at four different temperatures. The fast scan direction is vertical and the slow scan direction from left to right. The acquisition time of each image is $t = 2100\,\mathrm{s}$. Tunneling parameters and thickness of the Ni films were identical for the three series. The first series Figs. 7.1 a)-f) at $T = 4.6\,\mathrm{K}$ reveals a rapid movement of islands and step edges. A topmost island is disappearing completely after the second scan (black arrows). Directly above the vanishing island, the lower terrace grows to the bottom of the image (blue arrows). In the center of each image, a horizontal brighter line indicates a step edge of the Re surface several layers below the Ni film. This substrate related step edge is assumed to be fixed in space and can be taken as a topographic marker. In area A1, the formation and movement of a hole in the topmost layer are observed that crosses the substrate step.

The second series of STM images [Figs. 7.1 g)-l)] is measured at 12.9 K. In this case, the step edges and islands move slower compared to the previous low-temperature series. The light areas, i.e. the topmost layer, in the upper part of images Figs. 7.1 g)

and h) are moving downwards, whereas the lowest layer is growing. After the bottom layer is completed, the upper layer fluctuates only slightly, and small holes form at the topmost of the three dislocation lines. The third series of STM images [Figs. 7.1 m)-r)], measured at 78.3 K on a similarly prepared sample shows no movement of step edges. The scanned area drifts slightly downwards, indicated by the position of the bright defect and substrate step edges (blue arrows), likely caused by the higher temperature. In contrast, the topography of the surface itself shows no change of shape during the measurements. The fourth series of measurements [Figs. 7.1 s)-x)] shows the same behavior at room temperature. In conclusion, these three series illustrate a strong decrease in the mobility of the Ni/Re surface with increasing temperature.

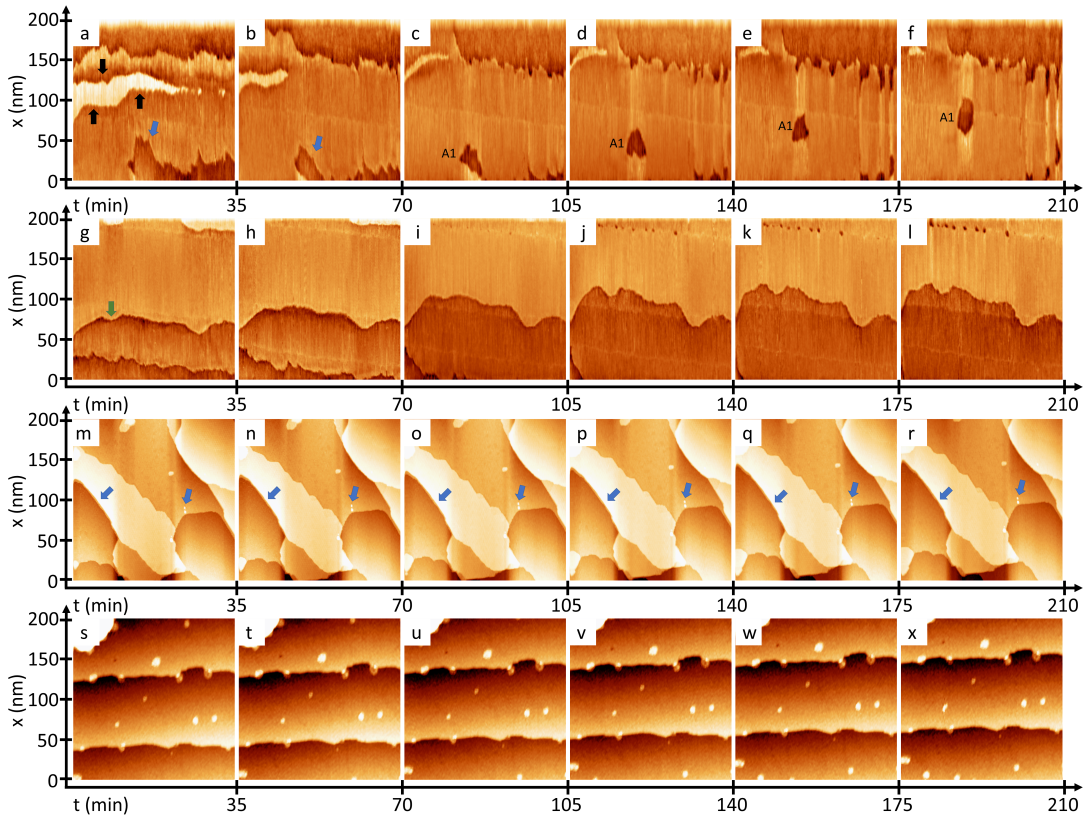

Fig. 7.1. Topographical STM images showing four series of Ni/Re surfaces. All measurements are recorded with the same parameters of $I = 2\,\mathrm{nA}$ and $V = 0.1\,\mathrm{V}$ with a size of $(200 \times 200)\,\mathrm{nm}^2$ and 5 ML Ni for a)-l) and 3.5ML for s)-x). a)-f) shows a series at $T = 4.6\,\mathrm{K}$, g)-l) at $T = 12.9\,\mathrm{K}$, m)-r) at $T = 78.3\,\mathrm{K}$, and s)-x) at room temperature. While the first two rows illustrate a movement of the Ni surface with speed decreasing over time, the third row reveals a stable topography as well as the fourth row [s)-x)]. The thermal drift causes the image area to move, but the relative position of step edges and islands remains the same.

In most cases, as exemplarily shown in the four series discussed above, Ni atoms mainly move within the area of measurement, leading to compensation of increasing and decreasing surface areas. Only a few cases show large size differences between added and removed areas as presented in Fig. 7.2. This means that in these cases a large

exchange of material with regions outside the visible area occurs. Fig. 7.2 displays two image series measured at 4.6 K for a Ni thickness of 4 atomic layers with a relatively large change in the shape of the surface. For the first series a)-f) the same tunneling parameters apply as in Fig. 7.1. The first two images of this series are measured at a particularly high scanning speed (9 minutes per image). One observes a very high speed of 2800 nm^2/min of moved area deduced from the first two consecutive images. The following images [Figs. 7.2 c)-f)] are recorded at a slower scanning speed (35 minutes per image), revealing a decreased speed of the movement with increasing scanning time.

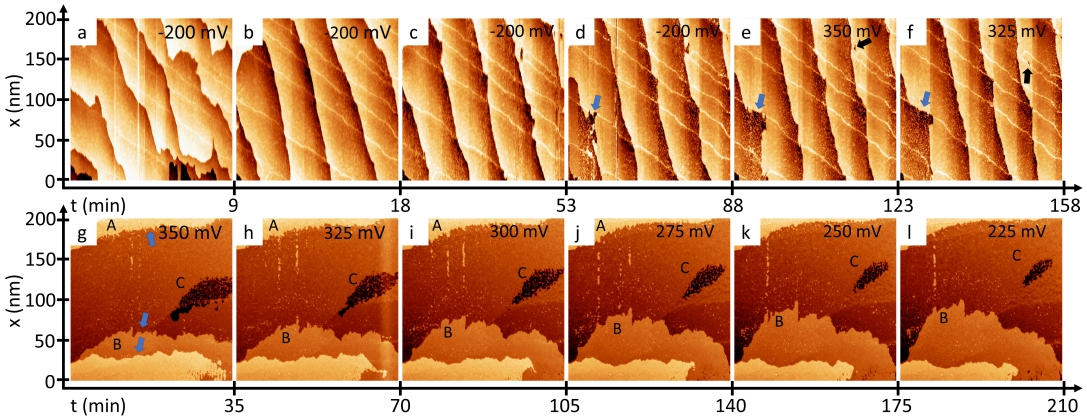

Fig. 7.2. This figure displays two series of measurements that illustrate some particular behaviors of the liquid-like Ni. a)-f) ($I = 2$ nA, $T = 4.6$ K, 8 ML Ni) show a measurement where the first two images are taken in 9 min per image, which is a quarter of the time of a normal measurement. Ni atoms move at high speed. In addition, the influence of fault lines can be seen very clearly here. g)-l) ($I = 1$ nA, $T = 4.6$ K, 4 ML) show a rather fluctuating movement, in which the Ni atoms move in different directions and close a hole. The moiré pattern on the lower island is clearly visible.

Here, a pronounced increase in material in the field of view can be seen. The additional material must have moved in from outside the measured area. For the series shown in Figs. 7.2 a)-f) the substrate steps are clearly visible. The substrate steps cause straight lines of higher strain in the overlying Ni film. In many cases, these lines act as a pinning center for the moving Ni atoms. On the other hand, one observes the creation of holes in the topmost Ni surface just at these lines (marked by blue arrows). The formation of these holes preferentially occurs at substrate steps, indicated by black arrows. The holes are likely caused by a directional flow of Ni atoms, blocked by some sections of the crossed substrate step line, and then coalescing at some distance behind the step.

The second image series, shown in Figs. 7.2 g)-l), reveals the moiré pattern, caused by the different lattice constants of Re and Ni. The island edge at the top of the images (A) slowly moves upwards in the first images until it starts to fluctuate: the step edge does not shift, but the contour changes slowly. The edge of the island (B) also moves upwards but with a higher speed and structured with the moiré pattern. The hole (C) in the center is slowly closing from the sides, filled up by mobile Ni atoms and small clusters, whereas the clusters within this hole disappear. These point defects can

also be seen in other areas and partly form horizontal lines along the scan direction or sometimes vertical lines.

To test to what extent the mobility is influenced by the electrical field between tip and sample, we recorded image series with a much lower tunneling current as depicted in Figs. 7.3 a)-f). Similar to the series shown in Figs. 7.2 g)-l) isolated small bright islands and clusters appear in the images (indicated by blue arrows), shown in Fig. 7.3. They show up in the differences as dark and bright spots, indicating that they do not remain stable from scan to scan. The size of the isolated islands amounts to below 1%. They are particularly high at step edges corresponding to a height of 2 layers. In Fig. 7.3 a), a mainly fluctuating movement of the step edges is observed: along the individual step edges, there is a small in- and decrease of the difference area occurring. In the following scans, on the other hand, there is a directed movement leading to a significant area increase or decrease along the entire step edge. An exception is the bright area (A) at the bottom of Fig. 7.3 g), which is first disappearing, and then growing again in the next three consecutive measurements [Figs. 7.3 h)-j)].

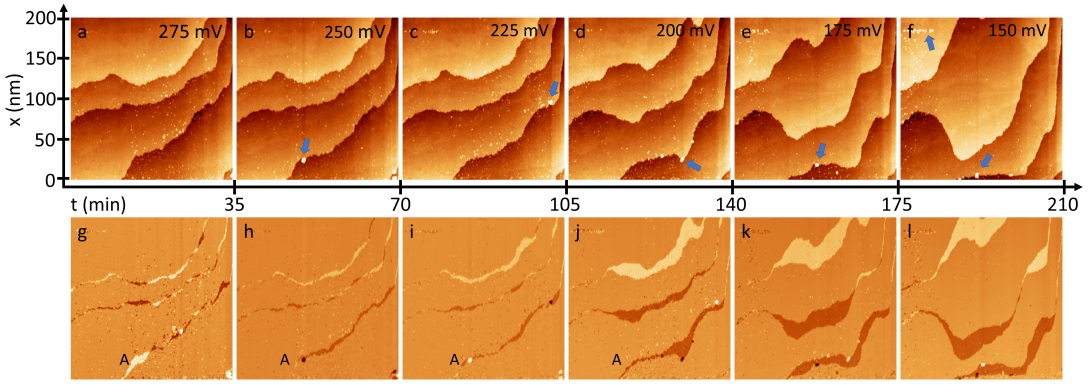

Fig. 7.3. a)-f) STM images measured at $I = 0.1\,\mathrm{nA}$, $T = 4.6\,\mathrm{K}$ with different voltages indicated in each image. The thickness is 4 ML Ni. The series shows an example of increased mobility over time. g)-l) Difference images, where two consecutively scanned images are subtracted. g) Results from the difference of an image measured before a) and a) itself, and h) results from b) minus a). The brighter color indicates increased terrace areas, while the darker color represents decreasing terrace areas. In Tab. 7.1, the fractions of the moved Ni areas are listed.

To illustrate the mobility of Ni atoms, difference images of consecutive scans are shown in addition to the topographic images. The difference images indicate increasing and decreasing areas as white and dark areas. The series, shown in Figs. 7.3 g)-l), illustrates such an analysis of a measurement and reveals increasing mobility over time. The first two images show almost no change while decreased and increased areas increase in size from scan to scan. In most cases, the topmost layer shrinks during the image series, while lower surface areas are increasing. To quantify the amount of transported material the dark and bright regions in the difference images are integrated. Both increased and decreased areas vary from 3% of the image size at the start of the series, to 10% for the last scan [see Tab. 7.1], which means that about $4000\,\mathrm{nm}^2$ of the Ni surface changes within 35 minutes. From these results, we conclude that Ni atoms show high mobility at 4.6 K even for high tunneling resistances, where the tip influence

should be small.

image	g	h	i	j	k	l
ΔA_+	2.3%	2.4%	2.4%	6.6%	9.8%	9.8%
ΔA_-	3.8%	3.1%	4.6%	7.6%	8.6%	7.8%

Tab. 7.1. Terrace area increase (ΔA_+) and decrease (ΔA_-) deduced from scan to scan are listed, corresponding to the light and dark regions in the series, shown in Fig. 7.3. Numbers are given as a percentage of the size of the scanned images of 40000 nm^2.

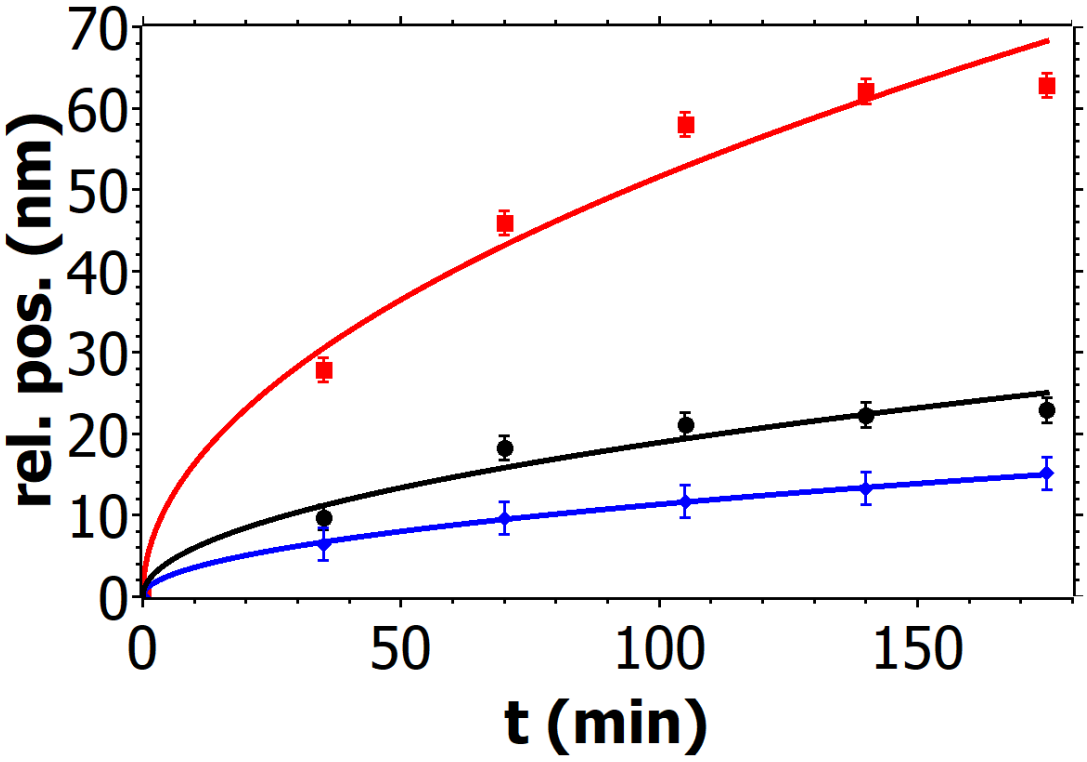

Fig. 7.4. The relative step edge positions for different image series are plotted as a function of time. The black data points result from the movement of the center step edge, marked with a green arrow in Fig. 7.1 g), in Figs. 7.1 g)-l) where five different positions of the step edge were averaged. The red points describe the movement of the island in Figs. 7.1 a)-f), marked with three black arrows in Fig. 7.1 a), and the blue data points originate from the movement of the three different step edges, marked with three blue arrows in Fig. 7.2 g) of the series shown in Figs. 7.2 g)-l). The data is fitted with a square root proportionality $[a \cdot t^{1/2}]$, where a is the only free parameter. The error bars indicate the fluctuation of the movement along the step edge.

Fig. 7.4 shows the step motion as a function of time for different series shown in Figs. 7.1 a)-f), Figs. 7.1 g)-l), and Figs. 7.2 g)-l). The step movement in these series is fast at the start of the series and slows down with increasing time. Assuming a diffusive process across the terrace planes one would expect that the position changes proportional to $t^{1/2}$. If the step movement is caused by diffusion along step edges

one would instead observe a proportionality to $t^{1/4}$. The $t^{1/2}$ scaling describes the data better than the $t^{1/4}$ proportionality. Hence, we conclude that the data favors an on-surface diffusion of Ni adatoms. Considering the continuations of these measurement series, shown in the Appendix A, a cyclic behavior of moving Ni atoms occurs: after decreasing the speed up to a certain point, the increasing movement can be triggered again. For this consecutive cycle, the movement follows again a $t^{1/2}$ law.

7.2. Discussion

In most cases, we observe a movement of Ni atoms along the vertical direction in the images, i.e. along the fast scan direction. To test how the tip movement influences the mobility of Ni atoms the scanning parameters were varied. The experimental results lead to the conclusion that the moving direction of Ni atoms is independent of several scanning parameters. There is no influence on the mobility of the Ni atoms, whether the endpoint of the previous measurement is the starting point of the following image which consecutively is measured in the opposite direction (from right to left), or whether the tip is moved to the starting point of the previous image and then the next measurement is started.

The difference image, presented in Fig. 7.5 b), reveals significant differences only as narrow lines related to the step edges. These differences are caused by a time lag of the feedback loop. If the tip scans over a step edge, for example, from a higher level to a lower level, the tip will approach the new level at a certain delay depending on the feedback loop settings. Therefore, the step edge appears shifted along the scan direction. The same happens in the opposite scan direction. Because the tip moves now in the opposite direction, the step is apparently shifted in the opposite direction, which leads to the observed bright lines in the difference image. Therefore, forward and backward images do not reveal any significant mobility of Ni atoms. Hence, it can be excluded that Ni atoms are pulled along the surface with the tip.

The experimental results suggest a simple model of movement: to explain the mobility of the Ni on the Re(0001) surface, we assume that the atoms at the step edges have the highest mobility and can dissolve there first, except for the few cases where a step edge nucleates on the surface in combination with a defect. Triggered by the electric field and the movement of the tip, the Ni atoms can move freely on the surface. Most of the time, they migrate from higher levels over step edges and then attach themselves there or moves further to even lower planes. During the movement, Ni atoms can also form small clusters, which can sometimes quickly cross several planes. Whether the clusters can be observed during movement depends on the scanning resolution.

The question is, what is the origin of the inverse behavior of the mobility of Ni on the Re(0001) crystal. The behavior of Ni on Re was measured at four different temperatures ($T = 4.6\,\mathrm{K}$, $T = 12.9\,\mathrm{K}$, $T = 78.3\,\mathrm{K}$, $T \approx 308\,\mathrm{K}$). At all temperatures, we could observe mobile Ni, but in the majority of scan series, the mobility of Ni showed the typical behavior as described in Fig. 7.1. At low temperatures ($T = 4.6\,\mathrm{K}$), Ni atoms almost always move at a comparatively high speed. With increasing temperature, the probability of movement and the amount of mobile Ni atoms is significantly

decreased. At $T = 12.9\,\mathrm{K}$, the mobility is significantly smaller than at $T = 4.6\,\mathrm{K}$, and at $T = 78.3\,\mathrm{K}$ or higher temperature we rarely saw any movement at all. The movement is neither uniform nor steady nor linear. We have observed in several cases an increase in movement speed, which then decreases again in the progress of the further scans.

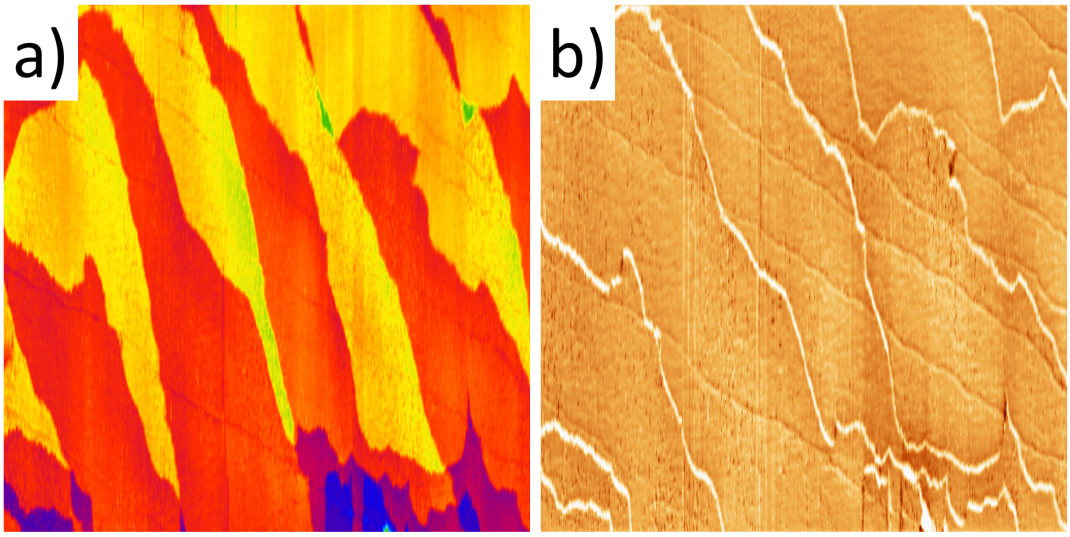

Fig. 7.5. a) The difference image of Figs. 7.2 a) and b); areas of the same level are in yellow. The zones with an increase of one layer (51.15 %) are in red, with two layers (3.87 %) in purple, with three layers (1.35 %) in blue and the turquoise spot at the bottom of the picture is with four layers (0.1 %) of increase. The three green spots on the upper side of the picture (0.28 %) are the only areas where the Ni disappeared. b) A difference picture of for- and backward measurement of Fig. 7.2 a). Apart from the brighter step edges, everything is at the same height.

The velocity and amount of the moved Ni area strongly vary. The difference image of the two scans depicted in Figs. 7.2 a) and b) is shown in Fig. 7.5 a) with a total moving area of 62.94 %, of which 3.78 % is over two and 1.35 % is over three levels moving. This happened in nine minutes resulting in a record speed of approximately $2800\,\mathrm{nm}^2/\mathrm{min}$, which is extremely high at these temperatures. It is not possible to determine which start and endpoint the moving Ni atoms had. Therefore, the actual speed cannot be calculated, also because nearly all (99.6 %) of the grown Ni is coming from regions outside of the scanned area, requiring even longer travel distances for the Ni atoms. One may assume that the Ni moves over several hundred nanometers. Besides, it is not clear if the Ni atoms, which detach at one step, attach directly to the adjacent step or whether they move freely over longer distances. The result, shown in Fig. 7.5 b), suggests a longer traveling distance.

The absolute scanning time for a series of images seems to have a smaller influence on the speed of the Ni atoms than the scanning speed. Thus, the mobility of Ni atoms does not directly depend on the duration of the measurement. The mobility is higher at the beginning of a series of measurement than at the end. This behavior can be traced back to a semi-stable initial situation of the Ni surface: the initial position of the Ni atoms and the associated strength to change to an energetically more favorable

position with fewer tensions in the material triggers a fast initial movement of the Ni atoms but also causes the movement speed to decrease over time. This decrease in diffusion rate occurs in the measurements often in a cyclic manner, i.e. the diffusion rate decreases according to the square root law over several measurements until it rises abruptly in the next cycle and then decreases again.

To summarize the results, no significant correlation between the measuring parameters tunneling current, tip-sample voltage, and scanning speed has been found. Furthermore, the coverage has a rather small influence on Ni mobility. If at all, the average mobility decreases for very thin and very thick layers. The movement was found between 2 and 20 monolayers, but no larger coverages were investigated so that the upper limit could not yet be determined. In most cases, Ni atoms move parallel to the fast scanning direction or fluctuate, but in a few cases, the direction of the moving Ni atoms may change, mainly at dislocation lines. In rare cases the movement starts not at the beginning of the series, i.e. the first one to five scans show no movement at all. Then the movement starts with a high velocity, sometimes combined with a change of the configuration of the STM-tip. This behavior indicates some kind of trigger mechanism activated by the tip. Overall, this behavior indicates a central role of the tip and a tip induced movement, but as previously discussed, the Ni atom movement cannot be directly linked to the tip movement.

The distance between tip and sample is typically between 0.5 nm and 1 nm. At a voltage of $V = 1\,\mathrm{V}$ applied to the tip, the electric field between tip and sample has a local field strength of $0.1\,\mathrm{V/Å}$ to $0.2\,\mathrm{V/Å}$ [127]. This is an extremely strong field of $10^9\,\mathrm{V/m}$, where a wide variety of interactions can occur. Such fields can give rise to several types of vibration, and current-induced mobility is gradually becoming possible. So, for the Ni atoms to start moving, three conditions must be fulfilled. Firstly, the tip must have activated the Ni surface by the electric field, which has the consequence that the surface partially changes to a liquid-like state. Secondly, the system must be in an energetically unfavorable state. Furthermore, the process must be triggered once. This is mainly done by the tip movement but can also be influenced by other factors. The result is a nearly free movement, which is independent of the tip movement, but at the same time, it is ending, respectively fluctuating, when a more favorable energetic state is reached. This model can simultaneously explain the variations in the amount and speed of Ni and the fact that the forward and backward images are identical. As the system is striving for a more energetically favorable state, the entropy of the system is not violated and as the Ni locally changes into a liquid-like phase, the increase or disappearance of Ni from the measured area can be traced, so the surface can therefore be assumed to be a very viscous Ni pool.

Our results confirm previous observations [93, 66] of an absence of an Ehrlich-Schwoebel barrier for the first 3 ML Ni on Re(0001). These studies also indicate that Ni adatoms show higher mobility at room temperature as compared to other metal-on-metal systems [6, 64, 65]. However, to our knowledge, there are no reports of increasing mobility with decreasing temperature. Because there is no obvious reason for this behavior, we discuss in the following the influence of strain as a tentative explanation. With the nearest neighbor distance of $a = 276.1\,\mathrm{pm}$ Re has a mismatch of $-9.74\,\%$ compared to the (111)-plane of Ni with the nearest neighbor distance of $a = 249.2\,\mathrm{pm}$ at room temperature. The strain is largely reduced from the second ML on. From

the moiré pattern with a 10×10 superstructure, one concludes on a strain of 0.28%, remaining constant in the range of thicknesses discussed in this article. This is also in agreement with previously reported results [66, 79]. At low temperatures, the lattice mismatch between the two metals increases to $-9.94\,\%$ [67], due to the different thermal expansion coefficients of Ni and Re [Fig. 7.6]. Consequently, the strain in the thickness range of $> 2\,\mathrm{ML}$ increases to 0.29%.

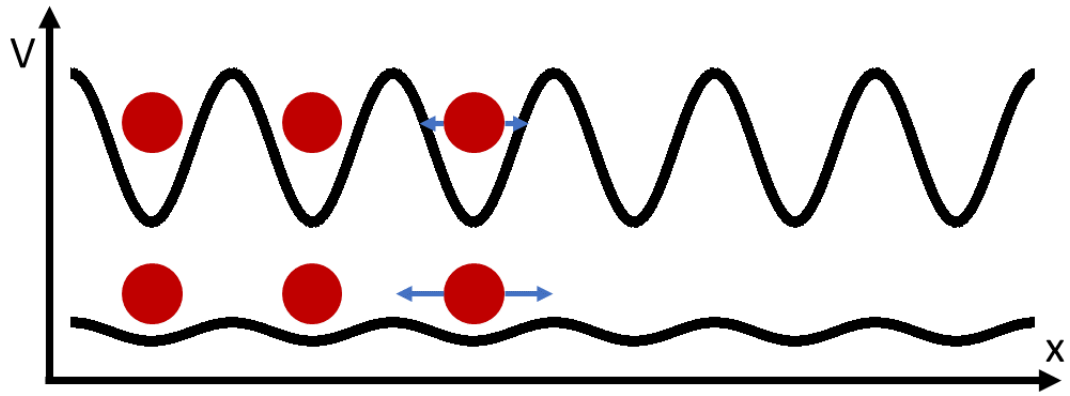

Fig. 7.6. The upper region represents a potential at 300 K, where the atoms are firmly bound. The increased mismatch at 4 K (lower area) reduces the energy barrier, and the atoms can move more easily and freely.

For Ni/Re(0001), an early work [79, 128] reports a constant strain up to 8 ML (from LEED) and up to 50 ML as deduced from magnetic anisotropies in these films. For Co/Mo(110), LEED revealed an expansive lateral strain independent of the thickness in a range of 1 ML to 50 ML [129]. For the slightly larger misfit of the Co/W(110) system, the strain is still constant up to a thickness of 10 ML [130]. For NiFe(111)/Cu(111) films a small misfit of 0.1% is constant up to 13 ML [131]. Thus, we conclude that a constant residual strain of ca. 1% for few monolayer thick metal films is a general phenomenon.

The increase of the strain at low temperatures represents an increase in local energy per Ni atom, which may contribute to the available energy for overcoming energy barriers and thus may initiate the observed increased mobility of Ni adatoms at low temperatures. The strain as deduced from LEED remains constant in a large range of thicknesses, which explains the observation of low-temperature mobility in the same thickness range. With increasing thickness, the number of strain releasing dislocation lines increases, explaining the measured reduction of mobility speed.

7.3. Movement at Higher Temperatures

At higher temperatures, the mobility of Ni severely is restricted, and the movement is rarely seen. However, the movement process of the Ni atoms is also changing slightly. While at low temperatures a fast motion with the formation of few to moderate Ni clusters could be observed, the formation of clusters of different sizes is predominant during the motion at $T = 78.3\,\mathrm{K}$. Figure 7.7 illustrates such movement at higher temperatures.

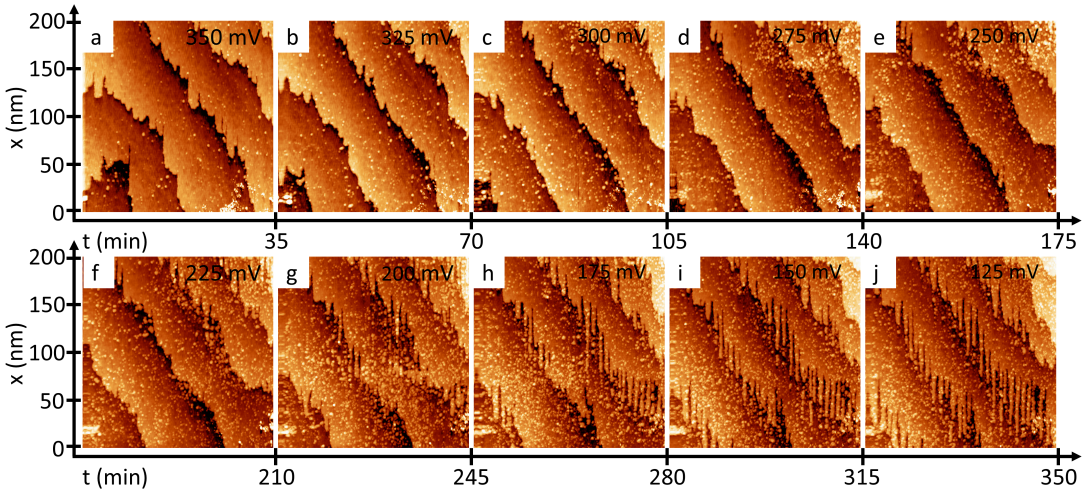

Fig. 7.7. A series of measurements, illustrating a special behavior of the Ni mobility at higher temperatures ($T = 78.3\,\mathrm{K}$); Recorded with the following tunneling parameters ($I = 1\,\mathrm{nA}$, $T = 78.3\,\mathrm{K}$), the series shows the formation of an especially large amount of Ni clusters and thin stripes along the fast scanning direction.

Already at the beginning of the series of measurements, some Ni clusters can be seen. These increase from image to image, which leads to the speckled pattern in the later measurements. Observing the step edges, a very fringy edge is noticeable. In the second part of the series [Figs. 7.7 f)-j)], this edge forms a stiff pattern parallel to the fast scan direction. In general, the movement is strongly directed in the fast scanning direction. In the lower-left corner, such a high concentration of clusters is formed that it reaches a height of 2 ML. That the movement of the Ni atoms partially occurs via the formation of clusters is already assumed before, but this measurement series particularly supports this thesis.

7.4. Dependence on Film Thickness

Most mobility measurements of Ni were performed on samples with moderate coverages between 1.5 ML and 7 ML. To test if there is a maximum or minimum limit above or below the Ni atoms are not mobile at all, more extreme thicknesses were also investigated. At thicknesses below 1 ML no typical movement could be observed in any of the measurements. This coverage can be assumed as the minimum limit at which the mobility of Ni normally is not possible. However, in two measurements, we

see something like the mobility of single Ni atoms and small clusters at 0.8 ML. In Figure 7.8 one of the series of measurements with a Ni coverage below a monolayer is displayed.

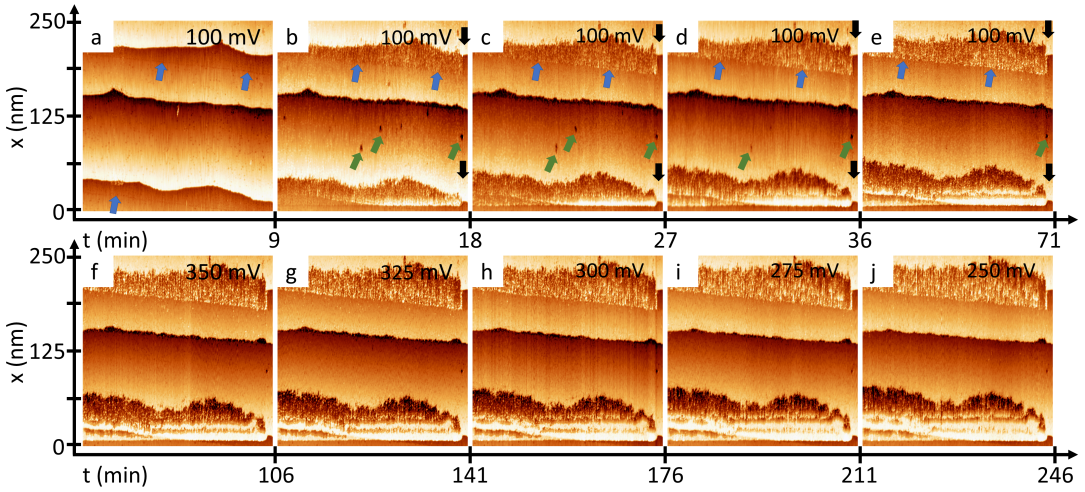

Fig. 7.8. This series of measurements is recorded at $I = 2\,\mathrm{nA}$, $T = 4.6\,\mathrm{K}$ with different voltages and scanning speeds written in each image and 0.8 monolayers of Ni deposited. With a coverage below a full monolayer, it is a rare example for another kind of movement: very small Ni clusters are formed in this case, that move only up to the substrate step edge (marked with blue arrows) and form a wall there. Notable is also a small area on the right edge the images that does not move at all (marked with black arrows).

In Figure 7.8 a), the first picture of this series is shown. The Ni monolayer areas are attached to the step edges of the Re crystal, marked by blue arrows, and have a smooth edge. Beginning with the second image [Fig. 7.8 b)], the smooth step edges of the Ni stripes become more and more fringy and slowly shift upwards. The mobility of Ni is very moderate and does not seem to go far beyond the Re step edges. Instead, the Ni atoms stop at the edge and form walls during the measurement. Especially in the lower part of the measurements the formation of several walls, one after another, can be observed.

The type of mobility is similar to the movement of thicker layers at higher temperatures [Sec. 7.3]: there is a cluster formation, which drives the movement forward. In this case, however, the clusters are much smaller, and it is assumed that some of them are monatomic clusters moving slowly in the direction of the step edges. Also, a formation of holes within the Ni surface, marked by green arrows, can be observed, which partly closes again in the course of the measurement. Interestingly, the holes do not form on step edges, as usual, but in the center of the smooth Ni surface.

However, the movement is not comparable to the mobility of Ni atoms above a coverage of one monolayer. Some of the atoms move just a few nanometers, and only at two of the three steps atoms are moving: the step edge in the center remains stable from the beginning to the end of the measurement. Various explanations for this behavior are conceivable. The most likely explanation is that in this kind of movement, the

tip plays a much more active role. It tears the Ni atoms out of the step decoration and actively pulls them forward until the tip loses the atoms at the next step edge or even before. This mechanism would explain both the very fringy step edge and the formation of single atoms and small clusters. A recording error caused by a tip that has picked up a Ni atom or another unknown measurement error also could be a possible explanation.

Notable is a small plateau at the left edge of the pictures, marked by black arrows. In contrast to other areas, the Ni layer does not move in this small section but forms a stable area. This stable area can be found on both step edges and remains throughout the entire series. This is a rare phenomenon that occurs in very few measurements. The reason for this phenomenon is unclear. It is assumed that a defect on the outer edge of the plateau pins the step edge. Accordingly, there is no movement beginning with the pinned step edge.

For coverages from 2 to 20 ML, no significant differences in mobility could be detected. At larger coverages, the formation of holes within closed Ni areas occurs more frequently. In addition, the movement speed decreases slowly with increasing thickness of the layers. In order to set an upper limit above which the Ni atoms cease to move, further measurements would be necessary with even larger coverages. This limit is very likely to exist at the latest when the Ni changes into a bulk state.

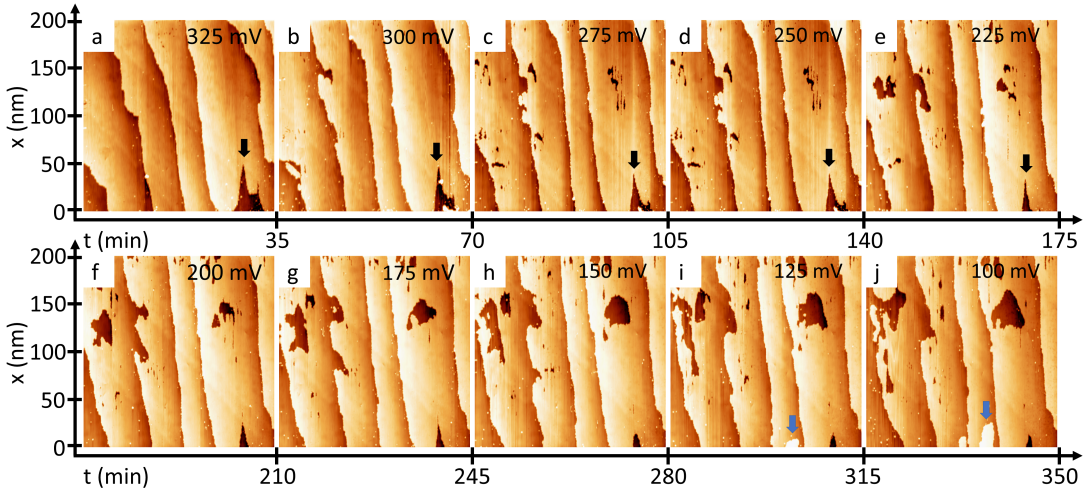

Fig. 7.9. A series of measurements, illustrating the mobility of Ni at a coverage of 20 ML; The images are recorded with a tunneling current of $I = 2\,\mathrm{nA}$ and variable voltages, indicated in the images. The series shows moderate mobility at $T = 4.6\,\mathrm{K}$. In this case, however, there is both a movement of the Ni atoms parallel and perpendicular to the fast scan direction. In addition, larger holes form on smooth surfaces.

In Figure 7.9 a series of measurements on Re covered with 20 ML Ni at $T = 4.6\,\mathrm{K}$ is shown. Similar to measurements on thinner layers, bright spots are distributed over the entire measurement, so the cluster formation does not differ from other measurements. The Ni step edges grow slowly to the left, orthogonal to the fast scan direction. This is unusual but can also be observed in other measurements. Much more significant is the growth of larger Ni islands in the center of the Ni areas in the last images of the

series marked, with blue arrows. These grow parallel to fast scan direction, so in this measurement growth in all directions is observable.

At the start of the series, there is a big hole at the bottom of the image, marked with black arrows, which is shrinking during the measurements. In contrast, starting with Fig. 7.9 c), holes appear in all areas of the surface. The formation is independent of defects or stepped edges of the underlying Re crystal. The holes are subject to a dynamically fluctuating growth and can both grow larger and shrink again. This behavior indicates that even at larger coverages the strain within the Ni layer is still present. Through the formation of holes, the strain can be partially relieved, especially for larger coverages, by extending the edges: the energy can be significantly reduced through the relaxation of the edge atoms. Therefore, further experiments on thicker layers will be very interesting, also to determine an upper thickness limit of mobility.

7.5. Au on Re(0001)

In order to compare the mobility of Ni films on Re(0001) with a different metal, measurements are carried out on Au films on Re(0001). Under conditions as similar as possible, 3.5 ML Au are deposited on the Re crystal and annealed. The purpose of the measurements is to verify if other metals, such as Au with a smaller mismatch between the lattice constants, move on the Re crystal as well. Measurements were made at three different temperatures ($T = 4.6\,\mathrm{K}$, $T = 13.1\,\mathrm{K}$ and $T = 78.7\,\mathrm{K}$) on the Au surface using similar tunneling parameters.

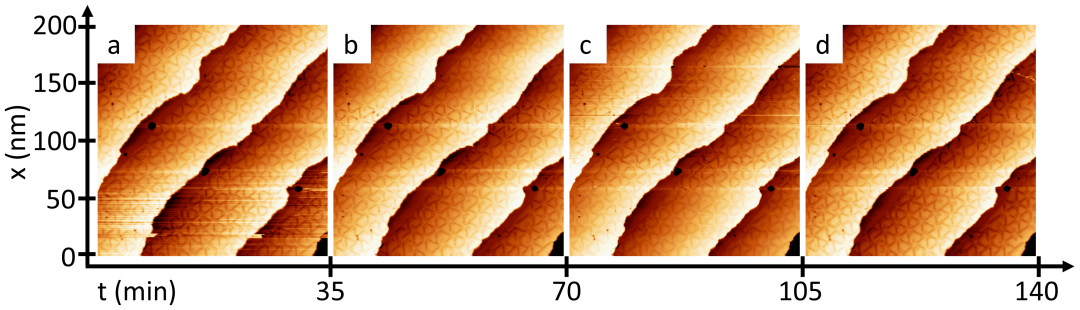

Fig. 7.10. This figure displays a series of STM images for 3.5 ML Au on Re(0001). The series is recorded with tunneling parameters of $I = 2\,\mathrm{nA}$ and $V = 100\,\mathrm{mV}$ at $T = 4.6\,\mathrm{K}$. The measurements on Au show a labyrinthine pattern. In contrast to the measurements on Ni, the Au atoms show no movement at all.

The result of this investigation is quite clear: none of the Au surfaces are mobile, confirming that Ni/Re(0001) shows an unexpected behavior. In Figure 7.10, one of these measurements is presented. As discussed in Chapter 5, the Au monolayer shows a labyrinth pattern for thicker coverages, and the step edges grow straight. A movement of the Au atoms is not observed which might be explained by the different strains for these two systems. For Au(111)/Re(0001) the misfit of the lattice constants is significantly lower. This observation supports the thesis that the considerable mismatch of the different lattice constants between Re and Ni contributes to the high mobility of

the Ni atoms. To further confirm this assumption, it would be necessary to evaporate other metals onto Re(0001) and to investigate them. Especially metals with a similar mismatch as Ni could also show increased mobility. On the other hand, if these metals do not show significant mobility, it would be interesting to investigate, which properties of Ni additionally contribute to the unusually high mobility of Ni on Re at low temperatures.

7.6. Spin-Resolved Measurements

Just like the surface states [Sec. 6.5], the Re(0001) crystal, covered with several monolayers of Ni, was investigated with spin-resolved STS. The Ni atoms, which are very mobile when using a tungsten tip at low temperatures, were unexpectedly solid and often did not move when measured with the Fe-coated tip. Therefore, in some measurements, a light-dark contrast of the Ni surface could be made visible until a part of the tip fell off and the Ni moved again. However, this stable state of Ni could not be reproduced. Nevertheless, this behavior raises the question of the influence of the tip on the mobility of the Ni again and examines it from a different perspective. Apparently, the magnetic spin-filtering effect or the different tunneling matrix of the iron-coated tip seems to change the influence of the tip on the Ni atoms.

We measured spectroscopic dI/dV maps on the Re(0001) surface, covered with 2ML Ni [Figs. 7.11 a), b), d)] and covered with 7ML Ni [Fig. 7.11 c)]. In Fig. 7.11 representative dI/dV maps at various energies are shown, displaying a contrast independent of the topographic height contrast. Figs. 7.11 a) and b) show two measurements of the same area, measured at $V = 125\,\mathrm{mV}$ and $V = -125\,\mathrm{mV}$. By changing the sign of the tip-sample voltage from plus to minus, the examined electronic states are changed from occupied to unoccupied states [Sec. 2.6]. In the case of positive voltages, the occupied sample states are measured. Due to the change of the examined states, the contrast is also reversed at zero crossing. This phenomenon is observed in all spin-resolved measurements and might indicate a magnetic contrast. It is noticeable that most of the dark areas are limited by step edges. The number of areas with a changed contrast increases by the evaporation of more monolayers of Ni, but the total area with the light-dark contrast decreases [Fig. 7.11 c)].

Magnetic domain walls form between differently oriented magnetic domains and represent the transition of the magnetization direction between homogeneously magnetized domains. The magnetic films form domains to minimize the magnetic stray fields and thus to minimize the free energy. In thin films, Néel walls with an in-plane magnetization are energetically more favorable than Bloch walls [132, 133]. For Ni films, Néel walls can be observed approximately up to a thickness of $a = 300\,\text{Å}$ [134], where the walls contribute to lower the total free energy [135, 136]. In Ni films between 5 nm and 75 nm domain walls with widths between 20 nm and 60 nm are observed [137]. The narrowest wall for the thinnest film was 12.5 nm [137]. For the case of a Fe monolayer on W(110), a particularly narrow domain wall with a width of 6 Åhas been measured using spin-polarized STM [138]. However, this is an exceptional case caused by the huge uniaxial anisotropy. Therefore, one would expect in this case of Ni/Re(0001) films domain wall widths larger than 10 nm. In the experiment, we observe transition regions

between dark and bright areas [Fig. 7.11], which are considerably narrower. Therefore, it is unlikely that the dark/bright contrast represents a magnetic contrast. The Curie temperature $T_c(d)$ of the Ni layer strongly depends on its thickness d. For 1.6 ML it is $T_c(1.6) = 46\,\mathrm{K}$ [139]. From this point of view, the ferromagnetic behavior of Ni films in the range of thicknesses studied here is likely. On the other hand, ferromagnetic domains can be much larger than the field of view in the STM images, preventing the observation of magnetic contrast.

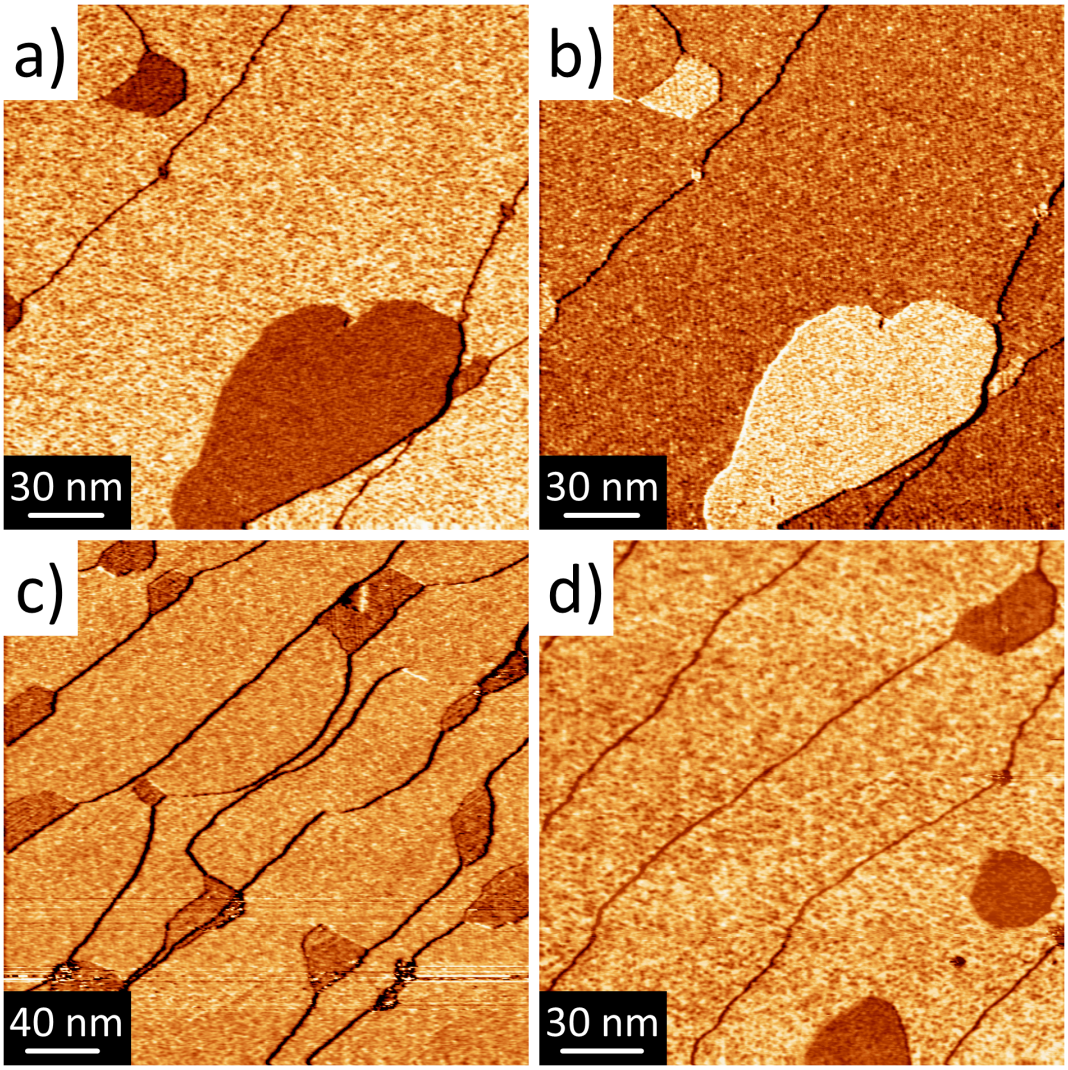

Fig. 7.11. Spin-resolved measurements of the Ni surface; a)-d) are recorded with tunneling parameters of $I = 2\,\mathrm{nA}$, $V_{\mathrm{mod}} = 6\,\mathrm{mA}$. a), b) and d) have a coverage of 2 ML Ni, c) has 7 ML. a) and b) were measured on the same sample at $V = 125\,\mathrm{mV}$ and $V = -125\,\mathrm{mV}$, which results in a strong change in contrast. c) is recorded at $V = 100\,\mathrm{mV}$ and d) at $V = 125\,\mathrm{mV}$. Notable is a contrast independent of the topographic height contrast, which may be caused by various effects.

Additional reasons exist against an interpretation of the observed contrast as magnetic contrast: the domains in all measurements are comparatively small and only two

different contrasting colors of the domains are found. If the measured structures were domains, they would only appear with two opposite spin orientations. This could only be attributed to an anisotropy of the material, in this case, crystal anisotropy. But since the crystal structure of hcp and fcc is six-fold, a contrast, indicating two different dI/dV values, cannot be explained. One would expect at least three different dI/dV values.

The domain walls in the measurements are extremely sharp, and there is an abrupt transition between the different areas of the Ni surface. Considering the results presented, it is rather unlikely that the measurements show a magnetic contrast. The layers investigated have a thickness of a few monolayers, i.e. far below 5 nm. Measurements of domain walls on monolayer coverages also show that the domain walls become significantly thinner compared to walls in thicker layers. However, in the measurements shown in Figure 7.11 the transitions are from 0.5 nm to a maximum of 1 nm corresponding roughly to the observations in [138]. The main argument against the interpretation of the magnetic contrast is the stray field minimization: many edges of the domains have a round shape. This is extremely unfavorable from an energetic point of view, because it is leading to charged domain walls in some regions. Due to the many and strong counter-arguments, it cannot be assumed that the spin-resolved measurements have a magnetic contrast. Accordingly, the question arises what the origin of the observed contrast is.

Several possible explanations could lead to the measured contrast. Close-packed sphere structures have three different planar arrangements, of which only two (A and B) occur in the hcp lattice. A third arrangement rotated by 30° appears in the fcc lattice. An obvious explanation for the observed contrast would be a stacking fault, i.e. hcp stacking for the topmost Ni layer. Also possible, but unlikely, would be a reconstitution on the surface of Ni with another material such as oxygen or CO from the residual gas. If this is the case, one would expect a 2×2 superstructure as observed in previous studies for defined surface contamination. The contrast could also indicate a denser packing of Ni atoms, for example, by a partial pseudomorphic growth in higher layers.

An alternative explanation for the contrast is a different atomic stacking of Fe in the dark areas compared to the rest of the sample. This assumption is supported by the fact that the dark areas are separated from other regions with a step edge, which has a height of approximately 2/5 of a normal step edge. Besides, the FT of the bright regions in both the spectroscopic and topographic measurements have the familiar six-fold structure of an fcc lattice. In contrast, the FT of the dark areas in Fig. 7.11 a) has shifted spots and further spots in addition to the 6 normal structure spots. While the 6 spots in a regular hexagon around the center reflect the moiré pattern, the additional structure spots indicate the growth of a bcc structure on the underlying Ni. So, it could be small Fe islands, which are created from particles that fell off the tip. Another hint for this thesis is the inversion of contrast in the pictures Figs. 7.11 a) and b). This is due to the spectroscopic effect, that different materials have maxima in the density of states at different energies. The higher the density of states, the brighter an area is shown in the measurements. Thus a strong light-dark contrast and the reversal of this contrast at different energies suggest that two different materials are present. However, further measurements are necessary to unambiguously prove this hypothesis.

8. Error Discussion

In this chapter, the errors that occurred in the measurements during the thesis are discussed. There are two major sources of error when measuring with the STM. First, the topographic imaging of the surface can be disturbed by mechanical noise, piezo-related image distortions, and changes of the tip during measurement (Sec. 8.1). Second, the spectroscopic images can be distorted by jumps or other influences described in Section 8.2.

8.1. Topographic Errors

Several influences affect or limit the imaging quality of topographic images. A significant problem are external vibrations: despite the eddy current retarder in the microscope, a lot of vibrations are not filtered, and especially at low frequencies in the hertz range, the damping is rather insufficient. Hence, at the beginning of the work on this thesis, a new damping system with an active piezo actuator was installed below the STM, reducing the background noise by a factor of ten. These efforts are only effective if the microscope is perfectly aligned so that the measuring head is suspended from the springs and swings freely without touching any other parts of the microscope.

By changing the measuring temperature, this alignment changes, and a continuous re-adjustment is necessary for which sufficient perfection is not always guaranteed. Despite all precautions, permanent isolation from external oscillations is not permanently given. Therefore, oscillations repeatedly occur in measurements, which have been partially referred to in the measurements concerned. Especially movements in the laboratory cause noticeable disturbances in the images. At the same time, electronic oscillations can also be coupled in, which leave a noticeable noise of discrete frequencies in the measurements. For example, $f = 50\,\mathrm{Hz}$ and multiples of it, as the standard of the German power grid, are reflected in the measurements.

Another source of error is the piezo element for controlling the tip. It tends to creep on the one hand and to show hysteretic behavior on the other, leading to an inaccuracy in the determination of the position. While the effects of hysteresis are small, creep can be observed, especially after a change of the tip position: the images are distorted in one direction, and the measurement must be taken several times until the piezo element has completely stabilized at cold temperatures. Only after several hours, these errors become neglectable.

A third point is the tunneling tip. Due to changes in state or macroscopic changes during measurement, images suddenly become blurred or completely unusable: if a piece falls off the tip, the sample will become locally contaminated. The tip can also form a double- or a multiple-tip, respectively, or become unstable. In these cases, the

measurement has to be aborted because the images cannot be acceptably analyzed. If the changes of the tip state occur more frequently, the images will be blurred. Thus, especially the series of measurements for the mobility of Ni, which require long acquisition times, are partially blurred and had to be processed considerably to obtain usable results. The length of the measurements of up to 22 hours dramatically increases the probability of changes of the tip or other measurement errors. Hence, several measurements are only useful for the first images of the measurement series.

8.2. Spectroscopic Errors

The tip plays a decisive role in spectroscopy. Here, changes of tip states are resulting in jumps of the spectral signal, respectively changes in resolution and quality of the measurements. The measured dI/dV maps often have a constantly changing contrast with several unusable measuring lines, which have no relation to the spectroscopic image. However, the problems of contrast can be almost eliminated in image processing with a background-subtraction. Single unusable lines of measurements can also be replaced by an average of the measuring lines above and below. Only if several consecutive lines are unusable, the image will be no longer completely restorable.

The power maps often had a considerable background noise, which could be significantly reduced by Fourier filters. Only frequencies in the range of the surface state can not be filtered because such a filter would significantly distort the measurement results. Therefore, the frequency of the lock-in amplifier had to be selected in such a way that as few interferences as possible with electrical sources of interference are generated. With the help of a frequency analyzer, $f = 786\,\mathrm{Hz}$ is chosen as a relatively interference-free frequency. The amplitude is chosen as small as possible with $V_{\mathrm{mod}} = 6\,\mathrm{mV}$ (rms) to achieve a good energy resolution without blurring the images.

In general, the electronics of the STM are very sensitive: electrical or magnetic fields, a slight noise of the current-voltage converter, but especially coupling oscillations from the power grid can cause considerable disturbances in the spectroscopy. Since the tunneling current signal of the measurement is in the nanoampere range, even the slightest contact between the measuring head and the chamber wall or between the eddy current brake components is sufficient to couple an interference signal into the measurement. This can also result in unwanted signals that can impair the measurement.

A further source of error results from the processing of the data. Especially because of the FT of the dI/dV maps and the resulting readout accuracy, a certain error occurs. This is increased if the additional ring-shaped feature, caused by the stabilization voltage for the tip height in constant-current mode [122], is in the same energy range as the surface state. This artifact caused confusion and misinterpretation at the beginning of the measurements, which could only be understood and corrected in the course of the measurements. It arises from spatial modulations in the transmission function due to variations in z at each (x, y) pixel that are dependent on the set-point conditions.

Compared to the three sources of error mentioned before, the measurement errors caused by the system devices such as time, voltage, and current resolution are negligible, so that error propagation would not yield to significant results. Instead, several measurements were averaged to obtain a more significant result, hence, a Gaussian error always results from the averaging. Thus, the systematic errors could be represented at least partially by a statistical error. More measurements for a more meaningful result would have been desirable, but due to the long measurement times and problems with the STM, it was not possible in terms of time. In addition, the standard deviation of most measurements is comparatively small, which is an indication of sufficiently good measurements.

Another possible error has already been discussed in Section 6.6, which led to a longer error search and analysis. In most dI/dV maps a continuous wave with a large wavelength appears, which varies from measurement to measurement. This measurement artifact could almost certainly be traced back to a slight disturbance in the piezo tube that is triggered when voltage thresholds are exceeded. Thus, the observed straight lines in the dI/dV maps are attributed to the digital to analog converters of the STM electronics. Due to the large wavelength, this measurement error is not found in the FTs of the dI/dV maps.

In the spin-resolved measurements using an iron-coated tip, additional artifacts appeared. It is not possible to measure the exact amount of iron deposited on the tip. Before the measurement, it is not clear whether the tip is stable or how the magnetic moment of the tip is aligned, so previous measurements were relied upon. In contrast to an uncoated tungsten tip, the coated tip cannot be pulsed infinitely or otherwise improved: it is not controllable how much iron is separated from the tip during pulsing. Accordingly, after a pulsing process, it is not possible to determine whether the measurements are still spin-resolved. Among several attempts, it was only once possible to produce a coated, stable tip. With this stable tip, all images, shown in Sections 6.5 and 7.6, were measured.

9. Conclusion and Outlook

The experimental studies described in this work are dedicated to investigate the topographic and electronic properties of the surface of pristine Re(0001) and the systems Ni/Re and Au/Re. Using a low-temperature ultrahigh vacuum STM, high resolution dI/dV maps and topographic images were measured. By analyzing the measurements, questions about the growth and scattering mechanism of surface states on these samples are clarified. The experimental results lead to insights into the fundamental mechanisms determining the mobility of Ni at low temperatures.

In the first part of this thesis, the theoretical principles of the STM and the measurement methods used in this work are discussed. In order to understand and analyze the measured phenomena, the basics of the samples and the concepts of entropy and inverse melting are explained. Also, the general approaches to predict and calculate the electronic band structure and especially the Rashba split surface states are discussed. The methods part of the work is closed with a description of the methodology for the experiments.

In Chapter 5 the growth of Ni and Au on Re(0001) is investigated as the basis for the following experiments. The LEED measurements show that the first monolayer of Au and Ni grows pseudomorphically. All subsequent layers grow epitaxially with a different lattice constant compared to Re. Topographic STM images show the formation of a short-range symmetrical moiré pattern beginning with the second monolayer of Ni. In the Au layers, the compressive strain due to the lattice mismatch is reduced by the formation of a hexagonal labyrinth structure. Both metals grow in the (111) orientation on Re(0001) with an in-plane orientation so that their nearest neighbor directions are parallel to the nearest neighbor directions of the Re(0001) substrate. Straight edges form along the three close-packed atomic row directions.

In Chapter 6, the energy dependence of the phase and wavelength of quantum interference patterns on Re(0001) is investigated by scanning tunneling spectroscopy. The hole-like energy dispersion relation of the corresponding surface state as deduced from Fourier transformation is independent of the momentum direction. The analysis of the attenuation of the quantum interference pattern with increasing distance from a declining step edge indicates interband scattering between the two branches of the Rashba split surface band. The interband scattering is also confirmed by a comparison of the dispersion relation with results from angular-resolved photoemission [26].

At a rising step edge, the attenuation with distance is considerably larger, which is tentatively explained by hybridization of surface and bulk states combined with an increased absorption probability. For testing, if spin-orbit or magnetic exchange scattering might change the interband to intraband scattering, which is forbidden without spin-flip, step edges were decorated with submonolayer Au and Ni stripes grown by step-flow growth, starting at the Re(0001) step edges. For the pseudomorphic

Au monolayer on Re(0001), a surface state could be determined in a short energy range around the Fermi energy. In comparison to the surface state on Re, this is less pronounced and shows an electron-like dispersion. In contrast to the pseudomorphic Au monolayer, the pseudomorphic Ni monolayer shows no quantum interference pattern, indicating that no surface state exists. The energy dispersion relation of the Tamm surface state on Re(0001) and the attenuation behavior of the corresponding quantum interference patterns do not change for these step decorations. This result indicates that spin-flip processes do not significantly contribute to the formation of quantum interference patterns.

The phase of the step-induced QPI pattern shows a π shift for a sign-change of the tunneling current. This shift points to a change of the scattering energy barrier from a potential dike for electrons to a potential trench for holes. A striking change to the opposite behavior is observed at the higher surface terrace when the top layer changes from Re to Au. In this case, representing the one-dimensional analog to a metal-metal layer interface, the Re surface state continues on the 1 ML Au/Re(0001) surface, showing a similar QPI pattern. The continuation of the surface state across the one-dimensional interface reverses the scattering barrier behavior.

The spin-resolved analysis of the surface states on Re(0001) shows a partial suppression of the surface waves near the step edges. A closer inspection of this phenomenon shows that it occurs predominantly on the lower terraces. The partial suppression hints to a spin-dependent scattering mechanism. A quantitative analysis would require further spin-dependent spectroscopic measurements.

In Chapter 7, the movement behavior of Ni atoms on a Re(0001) single crystal is investigated with the STM. By changing external parameters such as temperature, measurement parameters, and coverage, a model to explain this phenomenon could be established. We observe an increase of mobility with decreasing temperature, being in conflict with the model of thermally activated mobility involving the comparison of thermal energy and an energy barrier for hopping. The Ni adatoms can move at 4.6 K on the Ni(111)/Re(0001) surface in contrast to the conventional behavior of other metal surfaces such as Au(111).

The mass transport varies between 350 and 42400 atoms per minute within an area of 200 nm×200 nm over at least one step edge with a large variation over time. The average direction of the step movement is parallel to the fast scanning direction, indicating a tip-induced triggering of the movement. Due to the strong electric field of the tip, the bonding of Ni adatoms is weakened, and the movement of Ni atoms is initiated. Triggered by the tip, the system can change to an energetically more favorable state by the movement of Ni atoms. However, we did not find a systematic dependence of the trigger process on tunneling parameters. As a tentative explanation for the increasing mobility with decreasing temperature, we propose a contribution of lattice strain energy to the local potential energy of Ni adatoms, thus effectively lowering the energy barrier. Assuming bulk lattice expansion coefficients, the strain increases with decreasing temperature, being consistent with the observed inverse mobility behavior.

Several questions remain open, one of them being whether this is a classic inverse melting process. In two dimensions, the term melting is in general difficult to define, and it is better to speak of a mobility transition. The mobilization of the Ni atoms can be clearly seen, where an increase of mobility can be observed by cooling down the Ni atoms. Entropy and pressure seem to behave similarly to other examples of IM, but it is indeed not a matter of classical IM. One difference to IM is that the process has to be triggered. Therefore, the process can be better described as a decrease of the energy barrier for mobilization upon cooling.

Further questions remaining open comprise whether single atoms or clusters move and how the atomic hopping process is initiated. Also, the movement of Ni atoms on other substrates would be interesting. A complementary investigation using AFM would be useful to see the influence of the tip on the system and if the movement of Ni adatoms occurs without the electrical field of the tip. Further questions, still to be clarified by additional measurements, would be the quantitative movement speed and the limit of coverage, where the tensile strain has decreased so much that the Ni can no longer move. Additionally, the movement of Ni on other substrates would be interesting.

A slightly different mode of the mobility of the Ni atoms occurs at higher temperatures. A significantly increased formation of Ni clusters drives the reduced mobility of Ni. The mobility of Ni atoms differs at the minimum and maximum layer thickness, where the Ni atoms are mobile. A minimum layer thickness of about 0.8 ML could be determined, the upper limit is above 20 ML. While the Ni atoms within layers at the lower boundary move based on a different mechanism with very small clusters or even monoatomically, the formation of holes within the Ni areas can be observed especially in thicker layers. The observed mobility of Ni atoms with decreasing temperature has an interesting effect on the growth process and the resulting film morphology: the fast movement in combination with interlayer transport results in smoother morphologies. Under favorable conditions, homogeneity of Ni films, kinetically limited layer growth, and hence smooth surface morphologies can be achieved.

As a direct test for the model of the mobility of Ni, experiments with comparable Au layers are made. In this case, no movement on the surface could be detected at any temperature. Spin-resolved images of the Ni surface were also recorded during the course of this thesis. These images often showed no movement in contrast to images recorded with a tungsten tip. The differential conductivity contrast observed with the Fe-coated tip most likely does not indicate magnetic contrast, yet the contrast is originating from Fe atoms that have jumped from the tip to the surface.

At the end of this thesis, the several problems of the measurement are discussed in the error analysis. The most important sources of errors are related to external electrical and kinetic disturbances of the system and become statistically more probable due to the long measuring times. Therefore, mainly statistical errors are considered in the presented measurements.

In conclusion, the electronic states and atomic kinetics of the surface of a pristine Re(0001) single crystal in combination with step decorations of Ni and Au are investigated in this thesis. The findings in this work contribute towards investigating surface related effects for building and designing new electronic devices used for future nanodevices.

Bibliography

[1] J. M. Kosterlitz and D. J. Thouless. Ordering, metastability and phase transitions in two-dimensional systems. *J. Phys. C: Solid State Physics*, 6(7):1181, apr 1973.

[2] D. R. Nelson and B. I. Halperin. Dislocation-mediated melting in two dimensions. *Phys. Rev. B*, 19:2457, Mar 1979.

[3] A. P. Young. Melting and the vector coulomb gas in two dimensions. *Phys. Rev. B*, 19:1855, Feb 1979.

[4] A. L. Greer. Too hot to melt. *Natur*, 404:134, 2000.

[5] G. Tammann. *Kristallisieren und Schmelzen - Ein Beitrag zur Lehre der Änderungen des Aggregatzustandes*. Johann Ambrosius Barth, 1903.

[6] E. Bauer. Epitaxy of metals on metals. *Applications of Surface Science*, 11-12:479, 1982.

[7] C. H. Marrows and B. J. Hickey. New directions in spintronics. *Philosophical Transactions of the Royal Society A: Mathematical, Physical and Engineering Sciences*, 369(1948):3027, 2011.

[8] R. L. Schwoebel and E. J. Shipsey. Step motion on crystal surfaces. *Journal of Applied Physics*, 37(10):3682, 1966.

[9] R. L. Schwoebel. Step motion on crystal surfaces II. *Journal of Applied Physics*, 40(2):614–618, 1969.

[10] S. Kawai, A. S. Foster, T. Björkman, S. Nowakowska, Jonas Björk, F. F. Canova, L. H. Gade, T. A. Jung, and E. Meyer. Van der waals interactions and the limits of isolated atom models at interfaces. *Nat. Commun.*, 7:11559, 2015.

[11] M. K. Rose, A. Borg, J. C. Dunphy, T. Mitsui, D. F. Ogletree, and M. Salmeron. Chemisorption of atomic oxygen on Pd(111) studied by STM. *Surface Science*, 561(1):69, 2004.

[12] H. Lüth. *Solid Surfaces, Interfaces and Thin Films*. Springer, 2010.

[13] E. I. Rashba. Properties of semiconductors with an extremum loop. i. cyclotron and combinational resonance in a magnetic field perpendicular to the plane of the loop. *Sov. Phys*, 2:1109, 1960.

[14] P. Roushan, J. Seo, C. V. Parker, Y. S. Hor, D. Hsieh, D. Qian, A. Richardella, M. Z. Hasan, R. J. Cava, and A. Yazdani. Topological surface states protected from backscattering by chiral spin texture. *Nature (London)*, 460:1106, 2009.

[15] Z. Alpichshev, J. G. Analytis, J.-H. Chu, I. R. Fisher, Y. L. Chen, X. Shen, A. Fang, and A. Kapitulnik. STM imaging of electronic waves on the surface of Bi_2Te_3: Topologically protected surface states and hexagonal warping effects. *Phys. Rev. Lett.*, 104:016401, Jan 2010.

[16] L. El-Kareh, P. Sessi, T. Bathon, and M. Bode. Quantum interference mapping of rashba-split bloch states in Bi/Ag(111). *Phys. Rev. Lett.*, 110:176803, Apr 2013.

[17] L. El-Kareh, G. Bihlmayer, A. Buchter, H. Bentmann, S. Blügel, F. Reinert, and M. Bode. A combined experimental and theoretical study of rashba-split surface states on the $(\sqrt{3} \times \sqrt{3})$Pb/Ag(111) R30° surface. *New J. Phys.*, 16(4):045017, apr 2014.

[18] M. Steinbrecher, H. Harutyunyan, C. R. Ast, and D. Wegner. Rashba-type spin splitting from interband scattering in quasiparticle interference maps. *Phys. Rev. B*, 87:245436, Jun 2013.

[19] L. Petersen and P. Hedegård. A simple tight-binding model of spin–orbit splitting of sp-derived surface states. *Surf. Sci.*, 459(1):49, 2000.

[20] J. I. Pascual, G. Bihlmayer, Yu.M. Koroteev, H.-P. Rust, G. Ceballos, M. Hansmann, K. Horn, E.V. Chulkov, S. Blügel, P.M. Echenique, and Ph. Hofmann. Role of spin in quasiparticle interference. *Phys. Rev. Lett.*, 93:196802, Nov 2004.

[21] H. Zhang, F. Freimuth, G. Bihlmayer, M. Ležaić, S. Blügel, and Y. Mokrousov. Engineering quantum anomalous hall phases with orbital and spin degrees of freedom. *Phys. Rev. B*, 87:205132, May 2013.

[22] A. Stróżecka, A. Eiguren, and J. I. Pascual. Quasiparticle interference around a magnetic impurity on a surface with strong spin-orbit coupling. *Phys. Rev. Lett.*, 107:186805, Oct 2011.

[23] D. Hsieh, Y. Xia; L. Wray, D. Qian, A. Pal, J. H. Dil, J. Osterwalder, F. Meier, G. Bihlmayer, C. L. Kane, Y. S. Hor, R. J. Cava, and M. Z. Hasan. Observation of unconventional quantum spin textures in topological insulators. *Science*, 323(5916):919, 2009.

[24] X. Zhou, C. Fang, W.-F. Tsai, and J. Hu. Theory of quasiparticle scattering in a two-dimensional system of helical dirac fermions: Surface band structure of a three-dimensional topological insulator. *Phys. Rev. B*, 80:245317, Dec 2009.

[25] A. Urru and A. D. Corso. Spin-polarized electronic surface states of Re(0001): An ab-initio investigation. *Surf. Sci.*, 686:22, 2019.

[26] H. J. Elmers, J. Regel, T. Mashoff, J. Braun, S. Babenkov, S. Chernov, O. Fedchenko, K. Medjanik, D. Vasilyev, J. Minar, H. Ebert, and G. Schönhense. Rashba splitting of the tamm surface state on Re(0001) observed by spin-resolved photoemission and scanning tunneling spectroscopy. *Phys. Rev. Res.*, 2:013296, Mar 2020.

[27] M. F. Crommie, C. P. Lutz, and D. M. Eigler. Confinement of electrons to quantum corrals on a metal surface. *Nature*, 363:524, 1993.

[28] Y. Hasegawa and Ph. Avouris. Direct observation of standing wave formation at surface steps using scanning tunneling spectroscopy. *Phys. Rev. Lett.*, 71:1071, Aug 1993.

[29] J. Li, W. D. Schneider, and R. Berndt. Local density of states from spectroscopic scanning-tunneling-microscope images: Ag(111). *Phys. Rev. B*, 56:7656, Sep 1997.

[30] S. LaShell, B. A. McDougall, and E. Jensen. Spin splitting of an Au(111) surface state band observed with angle resolved photoelectron spectroscopy. *Phys. Rev. Lett.*, 77:3419, Oct 1996.

[31] J. Ohe, M. Yamamoto, T. Ohtsuki, and J. Nitta. Mesoscopic stern-gerlach spin filter by nonuniform spin-orbit interaction. *Phys. Rev. B*, 72:041308, Jul 2005.

[32] J. Friedel. The distribution of electrons round impurities in monovalent metals. *Philos. Mag.*, 43(337):1115, 1952.

[33] G. Binnig, H. Rohrer, Ch. Gerber, and E. Weibel. Tunneling through a controllable vacuum gap. *Applied Physics Letters*, 40(2):178, 1982.

[34] G. Binnig and H. Rohrer. Scanning tunneling microscopy. *Surface Science*, 126(1):236, 1983.

[35] H. Uchida, D.H. Huang, J. Yoshinobu, and M. Aono. Single-atom manipulation on the Si(111)7×7 surface by the scanning tunneling microscope (STM). *Surface Science*, 287-2880:1056, 1993. Proceedings of the 8th International Conference on Solid Surfaces.

[36] G. Meyer, L. Bartels, and K.-H. Rieder. Atom manipulation with the STM: nanostructuring, tip functionalization, and femtochemistry. *Computational Materials Science*, 20(3):443, 2001.

[37] S.-W. Hla, K.-F. Braun, and K.-H. Rieder. Single-atom manipulation mechanisms during a quantum corral construction. *Phys. Rev. B*, 67:201402, May 2003.

[38] J. J. Schulz, R. Koch, and K. H.Rieder. New mechanism for single atom manipulation. *Phys. Rev. Lett.*, 84:4597, May 2000.

[39] G. Binnig and H. Rohrer. Scanning tunneling microscopy. *IBM Journal of Research and Development*, 44(1):279, Mar 2000.

[40] G. Münster. *Quantentheorie*. De Gruyter, 2009.

[41] J. Bardeen. Tunnelling from a many-particle point of view. *Phys. Rev. Lett.*, 6:57, Jan 1961.

[42] J. Tersoff and D. R. Hamann. Theory and application for the scanning tunneling microscope. *Phys. Rev. Lett.*, 50:1998, Jun 1983.

[43] J. Tersoff and D. R. Hamann. Theory of the scanning tunneling microscope. *Phys. Rev. B*, 31:805, Jan 1985.

[44] J. C. Chen. Theory of scanning tunneling spectroscopy. *Journal of Vacuum Science & Technology A*, 6(2):319, 1988.

[45] C. Chen. Tunneling matrix elements in three-dimensional space: The derivative rule and the sum rule. *Phys. Rev. B*, 42:8841, Nov 1990.

[46] J. M. Blanco, F. Flores, and R. Pérez. STM-theory: Image potential, chemistry and surface relaxation. *Progress in Surface Science*, 81(10):403, 2006.

[47] D. Drakova. Theoretical modelling of scanning tunnelling microscopy, scanning tunnelling spectroscopy and atomic force microscopy. *Reports on Progress in Physics*, 64(2):205, jan 2001.

[48] S. Heinze, G. Bihlmayer, and S. Blügel. First-principles interpretation of scanning tunneling microscopy applied to transition-metal surfaces: Buried CuIr/Cu(001) surface alloys. *physica status solidi (a)*, 187(1):215, 2001.

[49] D. Wortmann, S. Heinze, Ph. Kurz, G. Bihlmayer, and S. Blügel. Resolving complex atomic-scale spin structures by spin-polarized scanning tunneling microscopy. *Phys. Rev. Letter*, 86:4132, Apr 2001.

[50] P. Ferriani, C. Lazo, and S. Heinze. Origin of the spin polarization of magnetic scanning tunneling microscopy tips. *Phys. Rev. B*, 82:054411, Aug 2010.

[51] M. Bode, S. Heinze, A. Kubetzka, O. Pietzsch, M. Hennefarth, M. Getzlaff, R. Wiesendanger, X. Nie, G. Bihlmayer, and S. Blügel. Structural, electronic, and magnetic properties of a Mn monolayer on W(110). *Phys. Rev. B*, 66:014425, Jul 2002.

[52] A. R. Smith, R. Yang, H. Yang, W. R.L. Lambrecht, A. Dick, and J. Neugebauer. Aspects of spin-polarized scanning tunneling microscopy at the atomic scale: experiment, theory, and simulation. *Surface Science*, 561(2):154, 2004.

[53] K. K. Saha, J. Henk, A. Ernst, and P. Bruno. Multiple-scattering theoretical approach to scanning tunneling microscopy. *Phys. Rev. B*, 77:085427, Feb 2008.

[54] G. Binnig, H. Rohrer, Ch. Gerber, and E. Weibel. Surface studies by scanning tunneling microscopy. *Phys. Rev. Lett.*, 49:57, Jul 1982.

[55] Øystein Fischer, Martin Kugler, Ivan Maggio-Aprile, Christophe Berthod, and Christoph Renner. Scanning tunneling spectroscopy of high-temperature superconductors. *Rev. Mod. Phys.*, 79:353, Mar 2007.

[56] R. Wiesendanger. *Scanning Probe Microscopy.* Springer, 1998.

[57] Y. Kuk and P. J.Silverman. Scanning tunneling spectroscopy of metal surfaces. *Journal of Vacuum Science & Technology A*, 8(1):289, 1990.

[58] R. Wiesendanger. *Scanning Probe Microscopy: Analytical Methods.* Springer, 1998.

[59] N. D. Lang. Spectroscopy of single atoms in the scanning tunneling microscope. *Phys. Rev. B*, 34:5947, Oct 1986.

[60] M. Bode. Spin-polarized scanning tunnelling microscopy. *Reports on Progress in Physics*, 66(4):523, mar 2003.

[61] C. Davisson and L. H. Germer. Diffraction of electrons by a crystal of nickel. *Phys. Rev.*, 30:705, Dec 1927.

[62] C. Davisson and L. H. Germer. The scattering of electrons by a single crystal of nickel. *Nature*, 119:558, 1927.

[63] M.A. Van Hove, W.H. Weinberg, and C.-M. Chan. *Low-Energy Electron Diffraction*. Springer, 1986.

[64] S. Ouazi, T. Pohlmann, A. Kubetzka, K. von Bergmann, and R.Wiesendanger. Scanning tunneling microscopy study of Fe, Co and Cr growth on Re(0001). *Surf. Sci.*, 630:280, 2014.

[65] M. Parschau, D. Schlatterbeck, and K. Christmann. Nucleation and growth of silver films on a rhenium (0001) surface: a combined STM and LEED study. *Surf. Sci.*, 376(1):133, 1997.

[66] M. Stindtmann, M. Farle, T. S. Rahman, L. Benabid, and K. Baberschke. Growth and morphology of Ni(111)Re(0001) ultrathin films: an in-situ study using scanning tunneling microscopy. *Surface Science*, 381(1):12, 1997.

[67] D. R. Lide. *CRC Handbook of Chemistry and Physics*, volume 84. CRC Press, 2004.

[68] G. Rouschias. Recent advances in the chemistry of rhenium. *Chem. Rev.*, 74(5):531, 1974.

[69] F. C. Frank, J. H. van der Merwe, and N. F. Mott. One-dimensional dislocations. I. static theory. *Proceedings of the Royal Society of London. Series A. Mathematical and Physical Sciences*, 198(1053):205–216, 1949.

[70] F. C. Frank, J. H. van der Merwe, and N. F. Mott. One-dimensional dislocations. II. misfitting monolayers and oriented overgrowth. *Proceedings of the Royal Society of London. Series A. Mathematical and Physical Sciences*, 198(1053):216–225, 1949.

[71] M. Volmer and A. Weber. Keimbildung in übersättigten Gebilden. *Zeitschrift für Physikalische Chemie*, 119U(1):277, 1926.

[72] I. N. Stranski and L. Krastanow. Zur theorie der orientierten Ausscheidung von Ionenkristailen aufeinander. *Monatshefte für Chemie*, 71:351, 1937.

[73] P. J. Berlowitz, J. E. Houston, J. M. White, and D. W. Goodman. Properties of monolayer and multilayer Ni films on the Ru(0001) surface. *Surface Science*, 205(1):1, 1988.

[74] J. Kolaczkiewicz and E. Bauer. Growth and thermal stability of ultrathin films of Fe, Ni, Rh and Pd on the Ru(0001) surface. *Surface Science*, 423(2):292, 1999.

[75] J. A. Meyer, J. Vrijmoeth, H. A. van der Vegt, E. Vlieg R. J., and Behm. Importance of the additional step-edge barrier in determining film morphology during epitaxial growth. *Phys. Rev. B*, 51:14790, May 1995.

[76] J. Rychlewski. On hooke's law. *Journal of Applied Mathematics and Mechanics*, 48(3):303, 1984.

[77] D. Gross, W. Ehlers, P. Wriggers, J. Schröder, and R. Müller. *Mechanics of Materials – Formulas and Problems: Engineering Mechanics 2*, volume 1. Springer Verlag, 2017.

[78] H. Kuchling. *Taschenbuch der Physik*, volume 21. Carl Hanser Verlag, 2014.

[79] R. Bergholz and U. Gradmann. Structure and magnetism of oligatomic Ni(111)-films on Re(0001). *Journal of Magnetism and Magnetic Materials*, 45(2):389, 1984.

[80] W. H. Cropper. Rudolf clausius and the road to entropy. *American Journal of Physics*, 54(12):1068, 1986.

[81] A. Wehrl. The many facets of entropy. *Reports on Mathematical Physics*, 30(1):119, 1991.

[82] S. Rastogi, G. W. Höhne, and A. Keller. Unusual pressure-induced phase behavior in crystalline poly(4-methylpentene-1): Calorimetric and spectroscopic results and further implications. *Macromolecules*, 32(26):8897, 1999.

[83] N. Schupper and N. M. Shnerb. Inverse melting and inverse freezing: A spin model. *Phys. Rev. E*, 72:046107, Oct 2005.

[84] W. Sinkler, C. Michaelsen, and R. Bormann. A transmission electron microscopy investigation of inverse melting in Nb45Cr55. *Journal of Materials Research*, 12(7):1872, 1997.

[85] Z. H. Yan, T. Klassen, C. Michaelsen, M. Oehring, and R. Bormann. Inverse melting in the Ti-Cr system. *Phys. Rev. B*, 47:8520, Apr 1993.

[86] A. Schöll, L. Kilian, Y. Zou, J. Ziroff, S. Hame, F. Reinert, E. Umbach, and R. H. Fink. Disordering of an organic overlayer on a metal surface upon cooling. *Science*, 329(5989):303, 2010.

[87] O. Portmann, A. Vaterlaus, and D. Pescia. An inverse transition of magnetic domain patterns in ultrathin films. *Nature*, 422:701, 2003.

[88] N. Jakse and A. Pasturel. Molecular-dynamics study of liquid nickel above and below the melting point. *J. Chem. Phys.*, 123(24):244512, 2005.

[89] G.L. Kellogg. Surface diffusion and clustering of nickel atoms on the (110) plane of tungsten. *Surf. Sci.*, 187(1):153, 1987.

[90] D.W. Bassett. Field ion microscope studies of submonolayer films of nickel, palladium and platinum on (110) tungsten surfaces. *Thin Solid Films*, 48(2):237, 1978.

[91] J. P. Jones and A. D. Martin. High field microscopy of nickel on tungsten. *Surf. Sci*, 41(2):559, 1974.

[92] S. K. Nayak, S. N. Khanna, B. K. Rao, and P. Jena. Thermodynamics of small nickel clusters. *J. Phys.: Condensed Matter*, 10(48):10853, dec 1998.

[93] J. A. Meyer, P. Schmid, and R. J. Behm. Effect of layer-dependent adatom mobilities in heteroepitaxial metal film growth: Ni/Ru(0001). *Phys. Rev. Lett.*, 74:3864, May 1995.

[94] P. Yu and M. Cardona. *Fundamentals of Semiconductors Physiks and Material Properties*. Springer, 2010.

[95] F. Bloch. Über die Quantenmechanik der Elektronen in Kristallgittern. *Z. Physik*, 52:555, 1929.

[96] H. Ibach and H. Lüth. *Festkörperphysik*. Springer, 2009.

[97] C. Kittel. *Introduction to Solid State Physics*. John Wiley & Sons, Inc, 2005.

[98] P. Hohenberg and W. Kohn. Inhomogeneous electron gas. *Phys. Rev.*, 136:B864, Nov 1964.

[99] R. M. Martin. *Electronic Structure, Basic Theory and Practical Methods*. Springer, 2004.

[100] A. Georges, G. Kotliar, W. Krauth, and M. J. Rozenberg. Dynamical mean-field theory of strongly correlated fermion systems and the limit of infinite dimensions. *Rev. Mod. Phys.*, 68:13, Jan 1996.

[101] S. D. Kevan. Effective-mass theory of simple surface states. *Phys. Rev. B*, 34:6713, Nov 1986.

[102] T. Hirahara, I. Matsuda, M. Ueno, and S. Hasegawa. The effective mass of a free-electron-like surface state of the Si(111)$3 \times 3 - $Ag surface investigated by photoemission and scanning tunneling spectroscopies. *Surface Science*, 563(1):191, 2004.

[103] W. Shockley. On the surface states associated with a periodic potential. *Phys. Rev.*, 56:317, Aug 1939.

[104] I. Tamm. Über eine mögliche Art der Elektronenbindung an Kristalloberflächen. *Z. Physik*, 76:849, Aug 1932.

[105] S. G. Davison and M. Steslicka. Relativistic theory of tamm surface states. *J. Phys. C: Solid State Physics*, 2(10):1802, oct 1969.

[106] R. De L. Kronig and W. G. Penney. Quantum mechanics of electrons in crystal lattices. *Proc. R. Soc. Lond.*, 130:499, 1931.

[107] S. D. Kevan, N. G. Stoffel, and N. V. Smith. Spin-orbit effects on the bulk penetration and energy shift of tamm states on Cu(001) and Ag(001). *Phys. Rev. B*, 32:4956, Oct 1985.

[108] Y. A. Bychkov and E. I. Rashba. Oscillatory effects and the magnetic susceptibility of carriers in inversion layers. *J. Phys. C*, 17(33):6039, 1984.

[109] M. Nagano, A. Kodama, T. Shishidou, and T. Oguchi. A first-principles study on the rashba effect in surface systems. *J. Phys.: Condensed Matter*, 21(6):064239, jan 2009.

[110] G. Bihlmayer, Yu.M. Koroteev, P.M. Echenique, E.V. Chulkov, and S. Bülgel. The rashba-effect at metallic surfaces. *Surface Science*, 600(18):3888, 2006.

[111] G. Bihlmayer, O. Rader, and R. Winkler. Focus on the rashba effect. *New J. Phys.*, 17(5):050202, May 2015.

[112] A. Manchon, H.C. Koo, J. Nitta, S.M. Frolov, and R.A. Duine. New perspectives for rashba spin–orbit coupling. *Nature Mater*, 14:871, Sept 2015.

[113] G. Nicolay, F. Reinert, S. Hüfner, and P. Blaha. Spin-orbit splitting of the l-gap surface state on Au(111) and Ag(111). *Phys. Rev. B*, 65:033407, Dec 2001.

[114] M. Hoesch, M. Muntwiler, V. N. Petrov, M. Hengsberger, L. Patthey, M. Shi, M. Falub, T. Greber, and J. Osterwalder. Spin structure of the shockley surface state on Au(111). *Phys. Rev. B*, 69:241401, Jun 2004.

[115] A. Bendounan, K. Aït-Mansour, J Braun, J. Minár, S. Bornemann, R. Fasel, O. Gröning, F. Sirotti, and H. Ebert. Evolution of the rashba spin-orbit-split shockley state on Ag/Pt(111). *Phys. Rev. B*, 83:195427, May 2011.

[116] A. I. Oliva, A. Romero, J. L. Pe na, E. Anguiano, and M. Aguilar. Electrochemical preparation of tungsten tips for a scanning tunneling microscope. *Review of Scientific Instruments*, 67(5):1917, 1996.

[117] M. Bode, S. Krause, L. Berbil-Bautista, S. Heinze, and R. Wiesendanger. On the preparation and electronic properties of clean W(110) surfaces. *Surface Science*, 601(16):3308, 2007.

[118] I. Horcas and R. Fernández. WSXM: A software for scanning probe microscopy and a tool for nanotechnology. *Rev. Sci. Instrum.*, 78:013705, 2007.

[119] F. Yang, Y. Yao, Z. Yan, H. Min, and D. W. Goodman. Preparation and characterization of planar Ni-Au bimetallic model catalysts. *Applied Surface Science*, 283:263, 2013.

[120] J.Regel, T. Mashoff, and H. J. Elmers. Quasiparticle interference of spin momentum locked surface states at step edges on Re(0001). *Phys. Rev. B*, 102:115404, Sep 2020.

[121] L. Petersen, P. T. Sprunger, Ph. Hofmann, E. Lægsgaard, B. G. Briner, M. Doering, H.-P Rust, A. M. Bradshaw, F. Besenbacher, and E. W. Plumme. Direct imaging of the two-dimensional fermi contour: Fourier-transform STM. *Phys. Rev. B*, 57:R6858, Mar 1998.

[122] A. J. Macdonald, Y.-S. Tremblay-Johnston, S. Grothe, S. Chi, P. Dosanjh, S. Johnston, and S. A. Burke. Dispersing artifacts in FT-STS: a comparison of set point effects across acquisition modes. *Nanotechnology*, 27(41):414004, sep 2016.

[123] J. Wang, W. Li, P. Cheng, C. Song, T. Zhang, P. Deng, X. Chen, X. Ma, K. He, J.-F. Jia, Q.-K. Xue, and B.-F. Zhu. Power-law decay of standing waves on the surface of topological insulators. *Phys. Rev. B*, 84:235447, Dec 2011.

[124] Ph. Avouris, I.-W. Lyo, and P. Molinàs Mata. STM studies of the interaction of surface state electrons on metals with steps and adsorbates. *Chem. Phys.*, 240(5):423, 1995.

[125] R. Smoluchowski. Anisotropy of the electronic work function of metals. *Phys. Rev.*, 60:661, Nov 1941.

[126] P. Avouris and I.-W. Lyo. Observation of quantum-size effects at room temperature on metal surfaces with STM. *Science*, 264(5161):942, 1994.

[127] B. N. J. Persson and Ph. Avouris. The effects of the electric field in the STM on excitation localization. implications for local bond breaking. *Chem. Phys. Let.*, 242(4):483, 1995.

[128] U. Gradmann, R. Bergholz, and E. Bergter. Magnetic properties of very thin films. *Thin Solid Films*, 126(1):107, 1985.

[129] J. Prokop, D. A. Valdaitsev, A. Kukunin, M. Pratzer, G. Schönhense, and H. J. Elmers. Strain-induced magnetic anisotropies in Co films on Mo(110). *Phys. Rev. B*, 70:184423, Nov 2004.

[130] H. Fritzsche, J. Kohlhepp, and U. Gradmann. Epitaxial strain and magnetic anisotropy in ultrathin Co films on W(110). *Phys. Rev. B*, 51:15933, Jun 1995.

[131] U. Gradmann and H. J. Elmers. Magnetic surface anisotropies in NiFe-alloy films: separation of intrinsic néel-type from strain relaxation contributions. *Journal of Magnetism and Magnetic Materials*, 206(3):107, 1999.

[132] L. Néel. Énergie des parois de bloch dans les couches minces. *Compt. Rend.*, 241(6):533, 1963.

[133] S. Middelhoek. Domain walls in thin Ni-Fe films. *Journal of Applied Physics*, 34(4):1054, 1963.

[134] C. L. Richard and H. J. Juretschke. Magnetoresistance and domain structure in thin nickel films. *Phys. Rev.*, 126:1378, May 1962.

[135] A. DeSimone, H. Knüpfer, and F. Otto. 2-d stability of the néel wall. *Calc. Var*, 27:233, 2006.

[136] H. A. M. van den Berg. Self-consistent domain theory in soft-ferromagnetic media. II. basic domain structures in thin-film objects. *Journal of Applied Physics*, 60(3):1104, 1986.

[137] C.T. Hsieh, J.Q. Liu, and J.T. Lue. Magnetic force microscopy studies of domain walls in nickel and cobalt films. *Applied Surface Science*, 252(5):1899, 2005.

[138] M. Pratzer, H. J. Elmers, M. Bode, O. Pietzsch, A. Kubetzka, and R. Wiesendanger. Atomic-scale magnetic domain walls in quasi-one-dimensional Fe nanostripes. *Phys. Rev. Lett.*, 87:127201, Aug 2001.

[139] K. Baberschke. The magnetism of nickel monolayers. *Appl. Phys. A*, 62:417, 1996.

List of Figures

2.1. Quantum Tunneling . . . 6
2.2. Bardeen's Model . . . 9
2.3. Model of the Tip . . . 11
2.4. STM Setup . . . 15
2.5. Constant-Height Mode . . . 17
2.6. Constant-Current Mode . . . 17
2.7. STS . . . 19

3.1. Different Growth Mechanisms . . . 25
3.2. Phase Diagram . . . 30
3.3. EBS Re . . . 35
3.4. Solution for Shockley States . . . 39
3.5. Rashba Effect . . . 41

4.1. STM . . . 44
4.2. The Probe . . . 45
4.3. Tip and Tip Holder . . . 50
4.4. The Sample . . . 52

5.1. LEED Measurements . . . 54
5.2. Sketch Ni/Au on Re . . . 55
5.3. Growth and Defects of Re(0001) . . . 57
5.4. Growth of the Step Decorations . . . 58
5.5. Growth of the Step Decorations . . . 59

6.1. dI/dV Maps of Re and Au/Re . . . 62
6.2. QPI Dispersion Relation of Energy and Wavelength . . . 63
6.3. QPI Attenuation of Lower and Upper Terrace . . . 64
6.4. Method for Obtaining the Phase Angle . . . 66
6.5. Phase Angle Analysis . . . 67
6.6. Schematic of Surface States . . . 68
6.7. Surface State on Au/Re . . . 69
6.8. Surface State on Au/Re 2 . . . 70
6.9. Spin-Resolved Surface State . . . 71
6.10. Line Defects . . . 73

7.1. Different Temperatures, Same Parameters . . . 76
7.2. Further Special Measurements . . . 77
7.3. Analysis of Mobility . . . 78
7.4. Mobility of Step Edges . . . 79
7.5. Analysis and Au Measurements . . . 81

7.6. Schematic of the Potentials 83
7.7. Another Movement 84
7.8. Below one ML 85
7.9. Movement at 20 ML 86
7.10. Spin-Resolved Ni 1 87
7.11. Spin-Resolved Ni 2 89

A.1. Additional Measurements 1 111
A.2. Additional Measurements 2 112
A.3. Movement at 20 Ml 2 113
A.4. Extension 1 114
A.5. Extension 2 114
A.6. Extension 3 115
A.7. Extension 4 115

A. Appendix

The appendix provides additional measurements supporting the statements presented in the main text. The three sections show measurements with different scanning parameters and coverages at 4.6 K (Sec. A.1), another measurement of the mobility of the Ni atoms at a larger film thickness (Sec. A.2), and extensions to the measurement series shown in the main text (Sec. A.3).

A.1. Mobility with Different Parameters

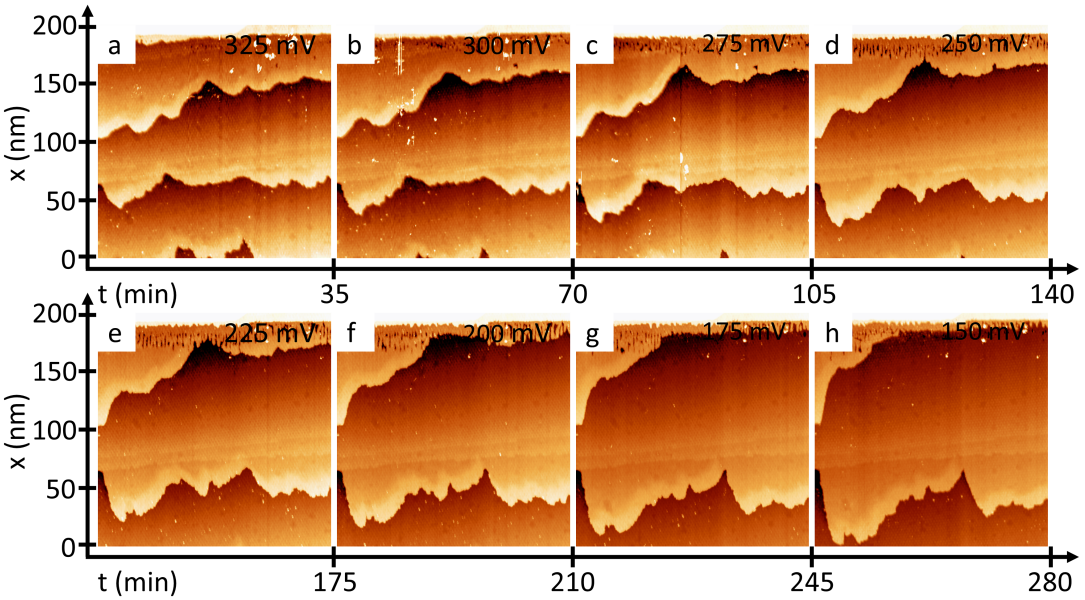

Fig. A.1. A series of measurements with a coverage of 7 ML Ni, recorded at $T = 4.6\,\mathrm{K}$ with a tunneling current of $I = 2\,\mathrm{nA}$ and variable voltages, indicated in the images.

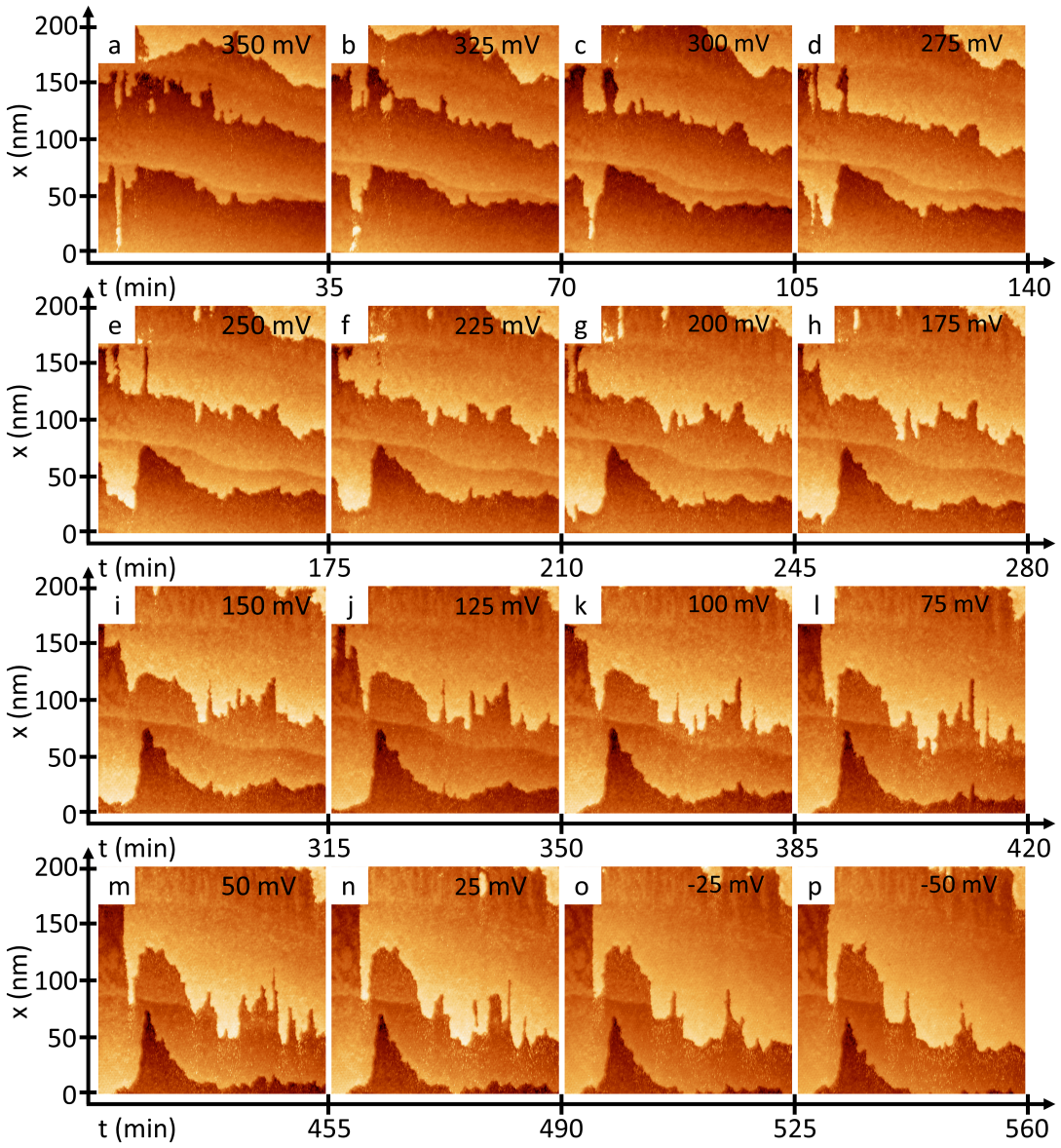

Fig. A.2. A series of measurements with a coverage of 2 ML Ni, recorded at $T = 4.6\,\mathrm{K}$ with a tunneling current of $I = 2\,\mathrm{nA}$ and variable voltages, indicated in the images.

A.2. Mobility at Higher Film Thickness

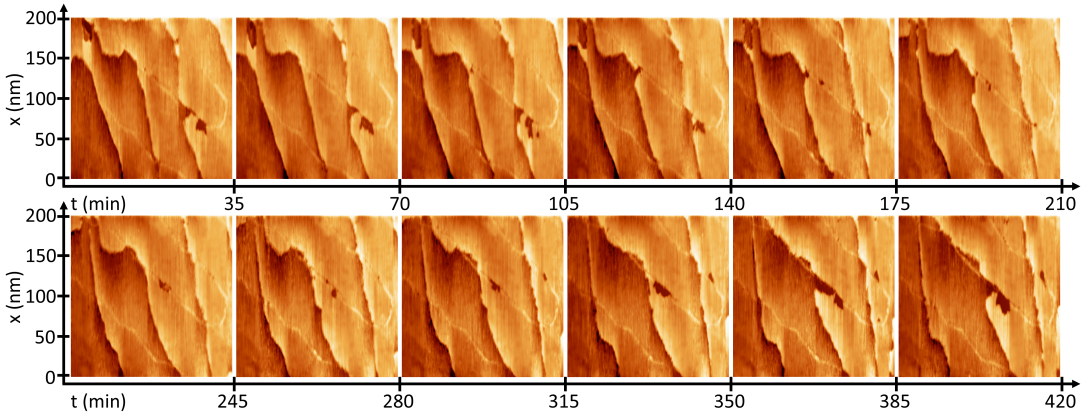

Fig. A.3. A series of measurements, illustrating the mobility of Ni at a coverage of 20 ML. The images are recorded with tunneling parameters of $I = 2\,\mathrm{nA}$ and $V = 0.1\,\mathrm{V}$. The series shows a moderate mobility at $T = 4.6\,\mathrm{K}$. Even with thicker layers dislocation lines are visible.

A.3. Extensions to the Measurement Series in the Thesis

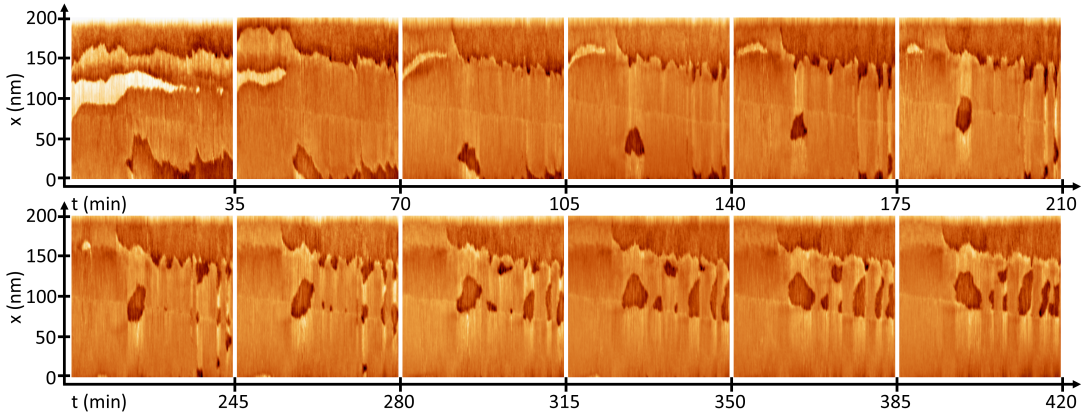

Fig. A.4. Series extension to the measurement shown in Figs. 7.1 a)-f) in the main text ($I = 2\,\mathrm{nA}$, $V = 0.1\,\mathrm{V}$, $T = 4.6\,\mathrm{K}$, 5 Ml Ni).

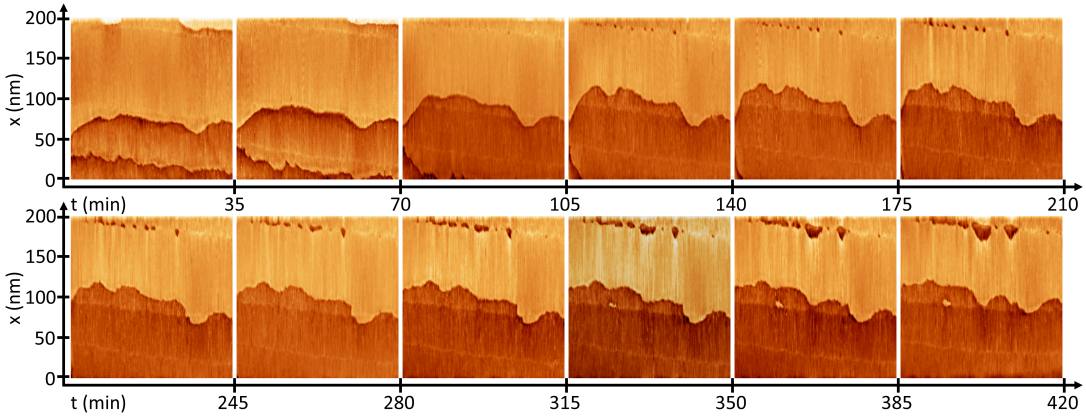

Fig. A.5. Series extension to the measurement shown in Figs. 7.1 g)-l) in the main text ($I = 2\,\mathrm{nA}$, $V = 0.1\,\mathrm{V}$, $T = 12.9\,\mathrm{K}$, 5 Ml Ni).

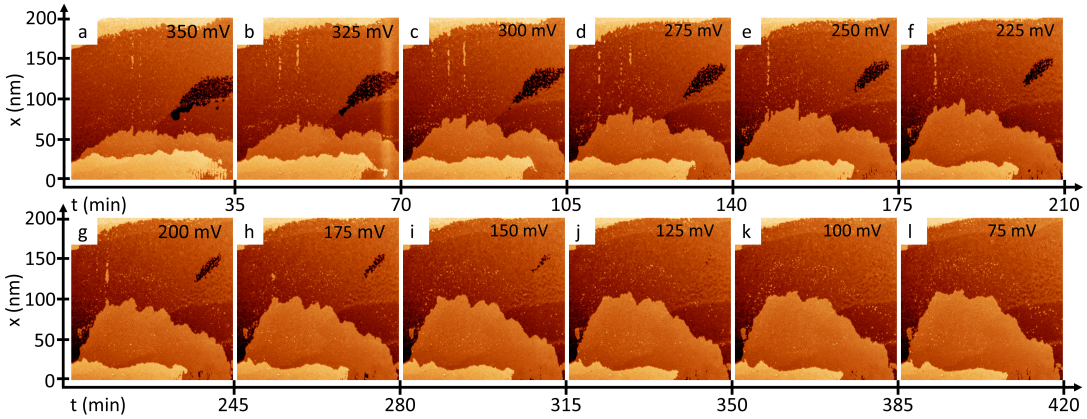

Fig. A.6. Series extension to the measurement shown in Figs. 7.2 g)-l) in the main text ($I = 1\,\mathrm{nA}$, variable voltage, $T = 4.6\,\mathrm{K}$, 4 Ml Ni).

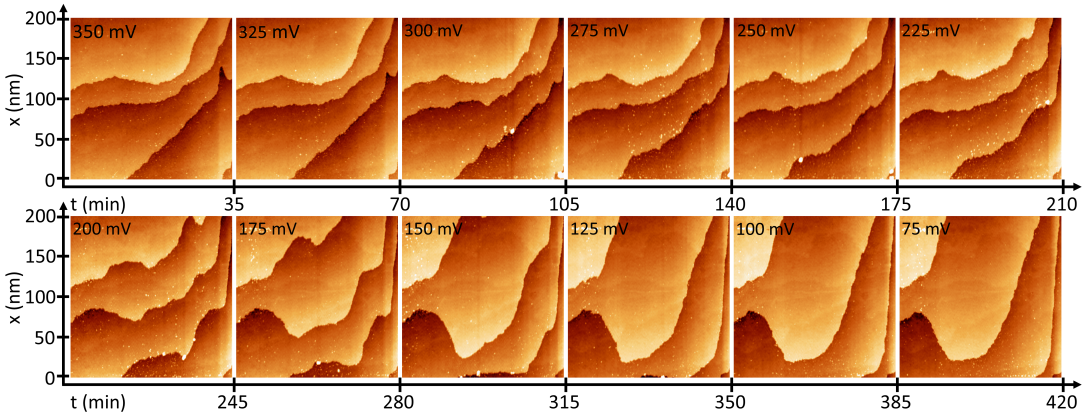

Fig. A.7. Series extension to the measurement shown in Figs. 7.3 a)-f) in the main text ($I = 0.1\,\mathrm{nA}$, variable voltage, $T = 4.6\,\mathrm{K}$, 4 Ml Ni).